



Università degli Studi di Napoli *Federico II*

DOTTORATO DI RICERCA IN FISICA

Ciclo: XXIX

Coordinatore: Prof. Salvatore Capozziello

Ultrafast laser surface structuring with Gaussian and Optical Vortex beam

Settore Scientifico Disciplinare : FIS/01

Dottorando
Jijil JJ Nivas

Tutore
Prof. Salvatore Amoruso

Anni 2014/2017

Acknowledgements

It is my great pleasure to acknowledge certain individuals who were contributory for the completion of my PhD research.

First and foremost, I would like to express my sincere thanks to my mentor and supervisor, **Prof. Salvatore Amoruso**, for his exceptional guidance, motivation, and unconditional support. I consider myself blessed for getting a chance to pursue my research studies with **Prof. S. Amoruso**. He is such a unique personality and a successful physicist that I could not have imagined having a better advisor and mentor for my Ph.D. I truly enjoyed working with him in the last three years and his skillful guidance and patience are greatly appreciated. Besides my advisor I would like to thank **Prof. Riccardo Bruzzese**, who contributed to many discussions that helped to shape my PhD. I express my whole hearted appreciation for his care, encouragement, insightful comments throughout my research. I also take this opportunity to thank **Dr. Xuan Wang**, who was always keen to help me to learn many programming skills, and for all valuable suggestions during my experimental work.

In the course of my research work, I was privileged to work with many collaborators in side as well as outside Italy. I would like to thank **Prof. Lorenzo Marucci** for a wonderful collaboration and for all your support. I thank **Dr. Domenico Paparo, Dr. Andrea Rubano and Dr. Filippo Cardano** for all their support, for our experiments on femtosecond optical-vortex laser ablation. Timely collaboration with **Dr. Antonio Vecchione, Dr. Rosalba Fittipaldi** (Università degli Studi di Salerno) has been an integral part of my research outcome. I would like to thank **Prof. Giovanni Ausanio** and **Dr. Felice Gesuele** for their kind support. Internal collaboration with other labs within the department of physics has fastened my research timeframe more than expected. I also thank **Prof. Raffaele Velotta**, former PhD coordinator, for his timely support.

I must thank the **Italian Education Ministry** for providing me with full funded PhD program which helped me to pursue research in University of Naples Federico II. I must thank my PhD Coordinator **Prof. Salvatore Capozzallo**, for all support and guidance to improve my research. I am very thankful to my internal referees **Prof. Alberto Porzio** and **Prof. Umberto Scotti di Uccio**. I also extend my thanks to **Prof. Carlo Ferdeghini**, the director of CNR-SPIN, for their kind support during my foreign visit related to conferences and internship program. I thank **Prof. Jörn**

Bonse of Federal Institute for Materials Research and Testing (BAM) Germany and **Prof. Nikolay Nedialkov** of Bulgarian Academy of Sciences, Bulgaria, for their insightful comments, suggestions and guidance while writing my thesis report.

I would like to express my special appreciation and thanks to **Prof. Reji Philip** of Raman Research Institute (RRI), Bangalore, India with whom I started my research carrier in ultrafast optics, initially as a visiting students and then as Junior Research Fellow. Apart from this I would particularly thank him for giving me an opportunity to carry out my PhD internship at RRI.

I am extremely obliged to Dr. Anoop KK, my senior lab mate and friend, who helped me while I start my work in University of Naples. I would like to extend my thanks to Dr. Shutong He and Dr. Zhenming Song, for being my very good friends and colleagues. I also thank Dr. Sam Sudhakaran and Dr. Nivya Roy for their care and immense support. All of you made me feel at home. I thank my fellow lab mates in RRI for their help and support. In particular, I am grateful to Dr. Smijesh N for teaching me how to work in a research lab and for his immense support in my personal and professional life. I thank my former lab mates in RRI, Mrs. Pranitha Sankar, Ms. Anitta Rose Thomas, Dr. Priya Rose, Mr. Muhammed Shafi Ollakan, Dr. Binoy K Anand, Ms. Tintu Kuriakose and Ms. Elizabeth Noble. I extent my thanks to Mr. Nithin Prasannan, Mr. Jayasankar, Mrs. Vrinda Bindu and all other friends in Bangalore.

In this moment I would like to express my sincere appreciations to my teachers and friends in College of Engineering Guindy-Chennai, Royal College of Engineering and Technology-Thrissur, Rehmaniya Arabic College-Katameri, Santhinikethen Secondary School-Thiruvallur and finally Ayanchery No.1 LP School.

These acknowledgements would not be complete without mentioning Mr. Guido Celentano, our PhD secretary, for acting as a local guardian. Last but not least, I thank my family: parents, partner and to my sister for supporting me spiritually throughout writing this thesis and my life in general.

Abstract

The progress in the physics of interaction of electromagnetic radiation with matter and related fundamental processes largely benefits from the contribution of the laser sources and many areas of investigation just commenced after the breakthrough given by the realization of the first pulsed laser in 1960 by T. H. Maiman. Contactless processing and high localization of energy possibly achieved with laser processing increased its acceptance in diverse fields. In general, reduced pulse duration offered by ultrashort laser pulses is utilized for direct monitoring of temporal dynamics of several fast atomic processes. On the other hand, the high intensity provided by such pulses gives a new twist in the field of laser ablation of materials. Study related to fundamental aspects of laser interaction and ablative processes opened numerous investigations and many possible applications. Because of the ultrashort duration, fs laser holds the capacity to achieve ablation with considerably less heat effected zone which in turns provides maximum spatial resolution in term of material processing. Controlled ablation processes with fs laser offer the possibility to generate periodic surface structures with a periodicity much less than the laser wavelength. This further proves the fs laser as a precise and versatile tool for micro- and nano-fabrication processes with great accuracy. Since many surface properties of solids (optical, wetting, mechanical etc.) are closely associated to their morphology, such phenomenon can have great impact on a variety of applications. Further applications include generation of microfluidic channels for biological uses and optical integrated circuits for quantum applications.

This thesis describes surface processing of crystalline silicon (100 orientation) with fs laser pulses with Gaussian as well as with some modified beam generated by a special optical device called q-plate. The experimental details and results are discussed in five chapters, which include a brief introduction about laser ablation and ultrafast laser processing. The first chapter gives a brief introduction about laser-matter interaction, underlying mechanisms of material ablation with ultrashort laser pulses along with a short overview of characterization methods used in laser induced plasma and material removal analyses. The material removal by the laser irradiation results in the generation of specific surface structures, generally called laser induced periodic surface structures (LIPSS). This chapter discusses also some basic aspects in the formation of LIPSS generated with Gaussian and Optical Vortex (OV) beams reported earlier. Finally, a short section illustrates the experiments on laser surface structuring using Gaussian and OV beams

presented in the next chapters of this thesis. The second chapter deals with experimental methods used in fs surfaces structuring experiments during this thesis. In particular, the laser sources and the method used to generate OV beams using q-plate are discussed. Moreover, it includes a brief description of sample material, optical setup and instrumentations used for surface structuring with different kind of fs laser beams and surface characterization. Chapter 3 illustrates experimental results on the various surface structures generated on crystalline silicon (100) by irradiation with fs laser pulses having a Gaussian spatial intensity profile. In particular, characteristic effects related to the number of pulses and energy are described. Moreover, bending and bifurcation phenomena characterizing quasi-periodic structures are presented. These aspects are, then, rationalized in the frame of a model of surface structure formation based on surface scattered wave theory. Finally, results of some experiments on the effect of the ambient gas pressure on the surface structures are also illustrated. The fourth chapter is dedicated to surface structuring with fs OV beam with orbital angular momentum (OAM) $m=1$ generated by a q-plate ($q=+1/2$). OV beams with azimuthal, radial, spiral and linear state of polarization (SoP) in the transverse plane are employed in the process, which enables not only to generate complex surface patterns but also to characterize the OV beam itself in the focal point. Interaction with more complex OV as the one generated with additional $\lambda/4$ wave plates gives interesting patterns of ripples and grooves. Results showing the laser structuring with higher OAM beams, such as $m=2$ and 5 , are also included in order to demonstrate the ability of laser induced structures in following the much more complex beam polarization pattern. The fifth chapter addresses an experimental investigation on direct femtosecond laser surface structuring with a higher class of vector beams generated by electrically tuning the optical retardation of a q-plate with $q=+1/2$. This allows generating a family of ultrashort laser beams with a continuous spatial evolution of polarization and fluence distribution in the focal plane by controlled coherent superposition of a uniformly polarized Gaussian beam with an OV beam. The use of these generalized vector beams in laser structuring can considerably improve the possibility of achieving a number of asymmetric surface patterns.

Finally, a brief summary of the experimental findings is reported in the last chapter also shortly addressing the scope of surface structuring and the possible applications of process and resulting periodic surface structures formed.

Published articles

- 1) **Jijil JJ Nivas**, Shutong He, Zhenming Song, Rosalba Fittipaldi, Antonio Vecchione, Riccardo Bruzzese, and Salvatore Amoruso. "Direct ultrashort laser surface structuring of silicon in air and vacuum at 1055 nm" *Appl. Surf. Sci.*, 2017, <http://dx.doi.org/10.1016/j.apsusc.2017.03.158>
- 2) **Jijil JJ Nivas**, Filippo Cardano, Zhenming Song, Andrea Rubano, Rosalba Fittipaldi, Antonio Vecchione, Domenico Paparo, Lorenzo Marrucci, Riccardo Bruzzese, and Salvatore Amoruso. "Surface Structuring with Polarization-Singular Femtosecond Laser Beams Generated by a q-plate" *Sci. Rep.*, vol. **7**, p. 42142, Feb. 2017.
- 3) **Nivas, Jijil JJ**, Shutong He, Zhenming Song, Andrea Rubano, Antonio Vecchione, Domenico Paparo, Lorenzo Marrucci, Riccardo Bruzzese, and Salvatore Amoruso. "Femtosecond laser surface structuring of silicon with Gaussian and optical vortex beams." *Appl. Surf. Sci.*, Oct. 2016, <http://dx.doi.org/10.1016/j.apsusc.2016.10.162>.
- 4) He, Shutong, **Jijil JJ Nivas**, Antonio Vecchione, Minglie Hu, and Salvatore Amoruso. "On the generation of grooves on crystalline silicon irradiated by femtosecond laser pulses." *Opt. Express*, vol. **24**, no. 4, pp. 3238–3247, Feb. 2016.
- 5) **Nivas, Jijil JJ**, Shutong He, Andrea Rubano, Antonio Vecchione, Domenico Paparo, Lorenzo Marrucci, Riccardo Bruzzese, and Salvatore Amoruso. "Direct Femtosecond Laser Surface Structuring with Optical Vortex Beams Generated by a q-plate." *Sci. Rep.*, vol. **5**, p. 17929, Dec. 2015.
- 6) **Nivas, Jijil JJ**, He Shutong, K. K. Anoop, A. Rubano, R. Fittipaldi, A. Vecchione, D. Paparo, L. Marrucci, R. Bruzzese, and S. Amoruso. "Laser ablation of silicon induced by a femtosecond optical vortex beam." *Opt. Lett.*, vol. **40**, no. 20, p. 4611, 2015.
- 7) He, Shutong, **Jijil JJ Nivas**, K. K. Anoop, Antonio Vecchione, Minglie Hu, Riccardo Bruzzese, and Salvatore Amoruso. "Surface structures induced by ultrashort laser pulses: Formation mechanisms of ripples and grooves." *Appl. Surf. Sci.*, vol. **353**, pp. 1214–1222, 2015.

Contents

<i>Acknowledgements</i>	ii
<i>Abstract</i>	iv
<i>Published articles</i>	vi
<i>Contents</i>	vii
<i>List of figures</i>	x
1 Ultrashort laser ablation and micromachining	1
1.1 General introduction	1
1.2 Laser ablation and characterization techniques	1
1.3 Mechanism of ultrafast laser ablation	3
1.3.1 Ablation and material removal with ultrashort laser pulses	4
1.4 Ultrashort laser induced surface structures	5
1.5 Overview of our experiments in surface structuring of silicon	9
2 Experimental methods	14
2.1 Introduction	14
2.2 OAM and generation of OV beams	15
2.2.1 The q-plate	16
2.2.2 Generation and optimization of OV beam with q plate	18
2.3 Characterization of fs Gaussian and OV beams for surface structuring	20
2.4 Silicon-ideal material used in surface structuring	22
2.5 General experimental setup for fs laser surface structuring	22
2.6 Generation of asymmetric beams with the q-plate	24
2.7 Surface characterization techniques	25
3 Surface structuring with a femtosecond Gaussian beam	28
3.1 Introduction	28
3.2 Laser induced periodic surface structures with a femtosecond Gaussian beam	29
3.3 Characteristic formation of LIPSS in Silicon [100] crystal	32
3.3.1 Evolution dynamics of different periodic structures	32

3.3.2	General characterization of ripples and grooves	34
3.3.3	Threshold of surface structure formation	37
3.4	Mechanism of LIPSS formation	39
3.4.1	Surface scattered wave model	40
3.4.2	Formation and characteristic bending/bifurcation of ripples	42
3.4.3	Formation of Grooves	46
3.5	Effect of nanoparticles in surface structure formation	48
3.5.1	Direct comparison of surface structure generated in air and high vacuum conditions	50
3.5.2	Structure evolution with varying ambient pressure	53
3.6	Conclusive Remarks	55
4	Surface structuring with femtosecond optical vortex beam	58
4.1	Introduction	58
4.2	Generation of fs OV beam from Gaussian beam by a q-plate	61
4.2.1	OV beams with $m=+1$ generated by a q-plate	61
4.2.2	Direct material ablation with OV beams with $m=+1$	63
4.2.3	Influence of N and F_p on surface patters	64
4.2.4	Surface structuring with other possible SoP for an OV beam with $m=+1$	65
4.3	Threshold calculation for OV beam	67
4.4	Effect of polarization using a shorter focal lens	70
4.5	Surface pattern generated by OV beam with more complex polarization	72
4.6	Ablation with higher OAM optical vortex beam	75
4.7	Conclusive remark	77
5	Surface structuring with generalized vector beams	81
5.1	Introduction	81
5.2	Generation of asymmetrical beam by q-plate	82
5.3	Surface structuring with beams generated by tuning the q-plate optical retardation	84
5.3.1	Patterning with generalized vector beams produced using the q-plate	87
5.4	Conclusive remark	94

6	Summary and perspectives	97
	Appendix I	i
	Appendix II	iv

List of figures

Fig. 1.1	Schematic picture addressing long laser pulse and femtosecond laser pulse interactions with a solid target.	3
Fig. 1.2	SEM images of LIPSS formed on gold and platinum following femtosecond laser irradiation at different angle of incidence.	6
Fig. 1.3	Colored silicon and aluminum produced by femtosecond laser pulse processing	7
Fig. 1.4	Examples of the silicon needle and chiral nano-needle fabricated at center of ablated zone by irradiation with a vortex beam.	9
Fig. 2.1	Examples of q plates.	16
Fig. 2.2	Schematics of the optical effect of a q-plate.	18
Fig. 2.3	Schematics of experimental setup showing optimization scheme followed with q-plate, $\lambda/4$ wave plates and polarizer.	19
Fig. 2.4	2D map of the beam profile generated from the simulation and the normalized values of intensity profile along the diameter for Gaussian and OV beam	20
Fig. 2.5	Schematic of the experimental setup used for direct laser surface structuring with fs laser beams generated by a q-plate.	23
Fig. 2.6	Three examples of the q-plate configurations for various optical retardations.	24
Fig. 3.1	Typical silicon surface after the irradiation with several fs laser pulse with Gaussian spatial intensity profile.	31
Fig. 3.2	SEM micrographs of the different surface structures formed after irradiation with $N = 2, 20$ and 50 laser pulses, illustrating the diverse morphologies of the rippled surface pattern.	33
Fig. 3.3	IL SEM micrographs illustrating the typical morphological features encountered by gradually moving from the rippled to the grooved areas through the intermediate region.	34
Fig. 3.4	Variation of the width of the different structured surface regions recognized in the craters produced as a function of the laser pulse energy and laser pulse number.	35
Fig. 3.5	The plot showing variation of radius of rippled and grooved area with pulse energy along with threshold fluence variation with the number of pulses.	38

Fig. 3.6	Sketches showing the geometry of the rough surface irradiated with s-polarized light at wavelength λ and the surface wave vector κ .	40
Fig. 3.7	Result from simulation showing the variation of the real and imaginary part of the dielectric permittivity ϵ^* , as a function of the peak fluence F_p , for various values of the pulse duration.	41
Fig. 3.8	SEM images of the evolving ripples structures at different excitation conditions and 2D gray-scale intensity maps of the efficacy factor with corresponding 2D-IFT along with the sketch of bending and bifurcations of ripples.	44
Fig. 3.9	SEM image showing central portion of the ablation crater where grooves are completely formed with 2D map of the efficacy factor and corresponding 2D-IFT.	47
Fig. 3.10	Examples of SEM micrographs illustrating the morphology of the surface spots generated in air and high vacuum.	49
Fig. 3.11	SEM micrograph of the surface spot generated in high vacuum with rotation in polarization.	52
Fig. 3.12	SEM micrographs of ripples generated at various ambient pressure along with the plot indicating the variation of spatial period of ripples measured at each individual pressure values.	54
Fig. 4.1	Symbolic image of the beam profile and 3D representation of incoming Gaussian and OV beam before and after the q-plate module	61
Fig. 4.2	The schematics of the q-plate configuration in generating OV beam with azimuthal, radial, spiral and linear SoP.	62
Fig. 4.3	CCD image of the OV beam, its spatial intensity profile and SEM images of the ablation crater in silicon.	64
Fig. 4.4	SEM images of the surface structures on the silicon target with azimuthally polarized OV beam after an irradiation sequence of N pulses for two different values of the pulse energy and number of pulses.	65
Fig. 4.5	SEM images of the surface structures on the silicon target after irradiation with radial, spiral and linear polarized OV beams.	66
Fig. 4.6	Variation of the internal (R_{in}) and external (R_{ex}) radii as a function of the OV beam energy for two different numbers of pulses along with the plot showing	69

	variation of F_{th} with N . Also R_{in} and R_{ex} , as a function of the number of pulses N for the OV beam with azimuthal, radial, and circular SoP.	
Fig. 4.7	Variation in the internal and external radii of the spot for radial and azimuthal polarizations in medium focusing condition with SEM images of the ablation spots generated by OV beams for one irradiation condition.	70
Fig. 4.8	Complex SoP generated for OV beam of $m=1$ with optical set up consisting of q-plate and $\lambda/4$ wave plate converting radial and azimuthal with SoP in the near-field and far-field.	73
Fig. 4.9	SEM images of structuring with OV beam of $m=1$ with complex polarization distribution.	74
Fig. 4.10	Representation of intensity and phase pattern of OV beam for different m values.	76
Fig. 4.11	Surface structuring of silicon by OV beam with higher OAM (for $m=1, 2$ and 5)	77
Fig. 5.1	Schematics of q-plate setup in the case of voltage tuning for various optical retardations along with variation of optical retardation and of the OV beam energy with different tuning voltage of the q-plate.	83
Fig. 5.2	Examples of SEM images acquired with the SE detector showing the surface morphologies developed on the silicon target for the Gaussian beam (un-tuned q-plate) and the OV beams (tuned q-plate, radial SoP) with spatial profile of laser fluence.	86
Fig. 5.3	The central panels show the spatial profiles, in the focal plane, of both the fluence and the SoP of various vector beams generated by changing the value of the q-plate optical retardation corresponding to radial SoP at tuned condition and the upper panels report the corresponding one-dimensional fluence profiles along the horizontal diameter. Lower panel displays the SEM images of the corresponding craters produced on the silicon target.	88
Fig. 5.4	SEM image, acquired with the IL detector, illustrating the surface morphology developed on the silicon target for the radial vector beam generated at $\delta = 1.5\pi$.	89
Fig. 5.5	The central panels show the spatial profiles, in the focal plane, of both the fluence and the SoP of various vector beams generated by changing the value of the q-plate optical retardation corresponding to azimuthal SoP at tuned condition and the upper panels report the corresponding one-dimensional fluence profiles along	90

the horizontal diameter. Lower panel gives the SEM images of the corresponding craters produced on the silicon target.

- Fig. 5.6 SEM images, acquired with the IL detector, illustrating the surface morphology developed on the silicon target for the radial vector beam generated at $\delta = 1.5\pi$. 91
- Fig. 5.7 Variation of the central position and area of the region of minimum fluence as a function of the optical retardation. 94

Ultrashort laser ablation and micromachining

“As an introduction, this chapter briefly discusses underlying mechanisms of ablation with ultrashort laser pulses reporting a short overview of material removal and surface structuring phenomena. Finally, a short section illustrates the experiments on laser surface structuring using Gaussian and Optical Vortex beams presented in the next chapters of this thesis.”

1.1 General introduction

Laser interaction with matter is uniquely interesting due to its peculiar properties like coherence and monochromaticity as well as high intensity field possibly achieved by focusing laser radiation. In general, ultrashort pulses are characterized by a pulse width which is equal to or less than a picosecond (ps). Their short duration typically results in less heat affected zone (HAZ) [1], a characteristics that stimulates a significant attention for fundamental studies and technological applications in material processing. The process of laser ablation and material removal occurs when the energy delivered by the laser pulse in the system is more than the binding energy of the material [2]. As a result of ultrashort laser irradiation or ablation, the target surface can remain decorated with different surface features. As many surface properties of the solids (optical, wetting, mechanical, etc.) are closely associated to their morphology, such phenomenon can have great impact on real world applications [3].

1.2 Laser ablation and characterization techniques

The focusing of energetic laser pulses on a solid creates a hotspot over the skin layer of the material that is brought in extreme conditions, whose relaxation leads to ablation and plasma formation. The laser ablation process can be dated back to the invention of pulsed lasers. For example, in 1962, Breech and Cross carried out a pioneering work on laser ablation of a metal by a ruby-laser observing the material removal and the formation of a laser produced plasma [4]. They collected and spectrally dispersed the light emitted from the plasma giving rise to laser induced breakdown

spectroscopy (LIBS), which is now a well-established laser-based elemental analysis technique. In the past decades, femtosecond (fs) laser pulses have made revolutionary changes in the field of laser ablation and generation of laser produced plasmas thanks to a temporal duration which is shorter than the characteristic relaxation times for electron-to-lattice energy transfer (picoseconds), heat conduction and hydrodynamic expansion of the material (tens of picoseconds to hundreds of microseconds). In this regime, ablation of a metallic target results in a material blow-off that is constituted by $\approx 10\text{-}20\%$ of atomic species followed by a strong expulsion of nanoparticles constituting the major part of the ablated mass. The resulting plume presents two spatially and temporally separated components: an atomic plume preceding a nanoparticles plume. There are several techniques utilized in the study of laser ablation by means of characterization of the generated plasma. These include time resolved evolution studies with photomultiplier tube (PMT), direct plasma imaging with charge coupled device (CCD) and intensified charge coupled device (ICCD), ion probe studies (Langmuir probe and Faraday cup), Thomson scattering, mass spectroscopy and many more [5]–[9]. Even though first investigation of the laser ablation process commenced about half century ago, the evolution of both laser technology and diagnostic techniques makes it an evergreen phenomenon and the underlying mechanisms and the various interesting effects related to new regimes of interaction endeavor further investigation of this process still today [10], [11]. Furthermore, from the very beginning laser ablation has always been drawing great attention and extensive investigations as it is at the base of many foremost laser-based applications, like LIBS, generation of nanoparticles and deposition of thin-films, creation of new materials with unique physical properties, micro/nano machining, high-precision drilling, laser welding and cutting, etc. Even many medical applications, like laser-assisted in situ keratomileusis (LASIK), are based on laser ablation [12].

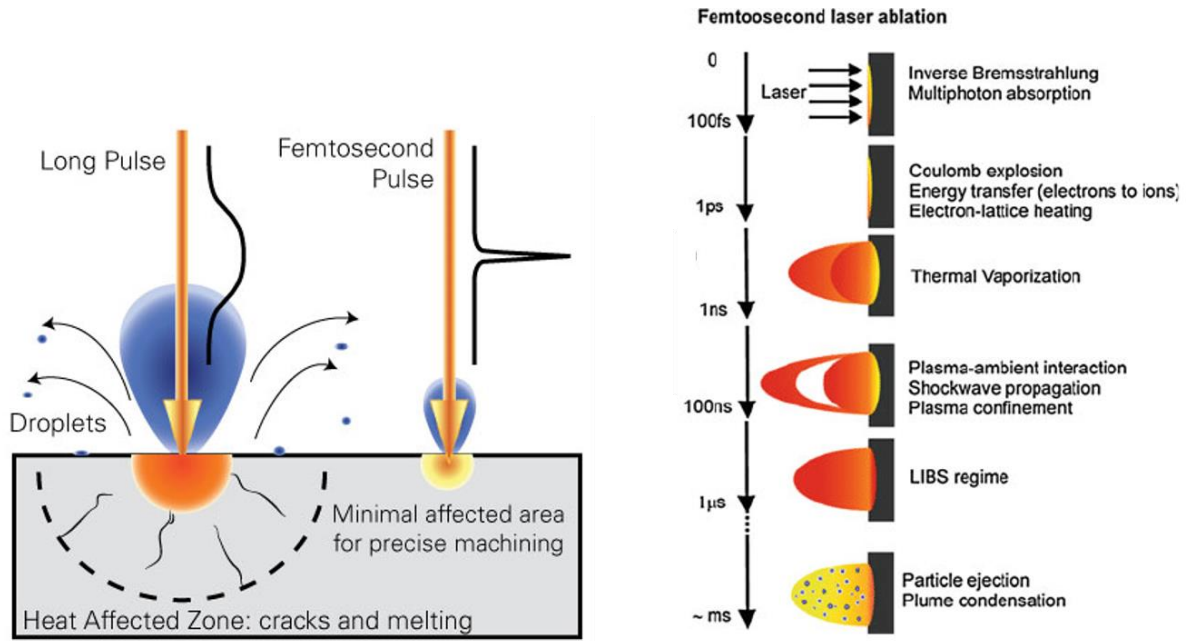


Figure 1.1| Left panel: schematic picture addressing long pulse and femtosecond laser pulse interactions with a solid target. Right panel: sketch of the approximate timescales involved in femtosecond laser energy absorption and ablation along with various processes occurring during and after the laser pulse [13], [14].

1.3 Mechanisms of ultrafast laser ablation

In the case of laser ablation, the exposure time is a parameter that greatly influences the efficiency of mass removal because it accounts for the power delivered (inverse relation with exposure time) into the system and is proportional to the laser pulse width. The typical values of laser pulse duration for a commercial Nd:YAG laser source is ≈ 6 ns, while common Ti:Sapphire laser systems deliver pulses of ≈ 35 -60 fs. This literally says that the spatial and temporal extension of fs pulses is $\approx 10^5$ times shorter than a typical nanosecond pulse. This temporal pulsewidth is shorter than all major relaxation times involved in laser-solid interaction, hence such pulses excite only the electrons of the system during their short duration, leaving the lattice cold. Subsequently, the absorbed energy is transferred from heated electrons to lattice by means of several relaxation mechanisms occurring on longer timescales [2]. Therefore, the interaction process is quite different for long (typically ns) and fs pulses due to the temporal separation (in the case of fs) and temporal overlap (for ns case) between the onset of laser and the effective electron-lattice energy transfer time triggering the plasma formation, which usually comes on the order of picoseconds (ps). Moreover, by compressing light pulses down to the fs timescale, solids can be irradiated at

intensities of the order of 10^{11} - 10^{13} W/cm² while only depositing micro-joules of energy into the material. The high peak power of fs pulses promotes nonlinear absorption within the bulk of transparent materials. Left panel of Fig. 1.1 schematically displays the basic difference in the interaction of long pulse and fs pulse with a solid [13]. During long pulse interaction, energy is deposited over a comparatively long period of time, leading to heat conduction and other unwanted effects resulting in melt re-solidification, cracks, and voids due to thermal stress, etc. In contrast, for ultrashort laser pulse the duration of the pulse is shorter than the time required for energy to be transferred from electrons to surrounding atoms. This results in a minimum HAZ [1]. Moreover, fs pulses have lower energy deposition depth even though the sample and emission wavelengths are same. This difference is ascribed to the linear (ns) and nonlinear multiphoton absorption (fs) processes occurring in the initial stage of laser ablation process. The absorbed energy becomes dissipated into different processes, such as electronic excitation, ionization, heating, shock waves propagation, and vaporization. The upcoming section illustrates the mechanisms underlying laser ablation and material removal in ultrashort pulse irradiation.

1.3.1 Ablation and material removal with ultrashort laser pulses

The interaction with the ultrashort laser pulses delivers significantly high intensity and power which ultimately leads to the excitation of solids into a non-equilibrium state. The process of interaction between ultrashort laser pulses and solids allows the study of materials under extreme conditions which can hardly be obtained with other feasible methods. Right panel of Fig. 1.1 schematically represents main processes and corresponding timescales under fs laser interaction from onset of pulse to particle ejection from the target material and plasma formation [14]. After excitation, melting occurs approximately on a picosecond timescale [15]. During the onset of fs laser pulse over a metal surface, the absorbed pulse energy will excite only valence electrons through inverse bremsstrahlung mechanism over a skin layer of the order of 10-nm thickness. This excited electrons approach a Fermi-Dirac distribution after about 200 fs [16]. Generally, in solids up to 10% of available valence electrons are contributed towards the excited non-equilibrium carrier density [17], which substantially changes the interatomic binding potential [18]. The thermalization of the excited electrons can be expected to occur immediately, due to the short electron-electron interaction time, and their temperature usually exceeds over 11,000 K (≈ 1 eV). However, this drastic and instantaneous thermal change is unfollowed by the ions and thus the

lattice remains at room temperature [3], [19]. This differential temperature dynamics [16] develops a temperature gradient between electron and lattice, which remains for several picoseconds after the termination of fs pulse. Unlike the case of ns pulse irradiation, during this time interval the fs laser pulse is no longer interacting with the solid and electronic and lattice sub-systems are out of equilibrium. This transient two-temperature system will tend to reach thermal equilibrium within a few ps through electron-phonon interactions as well as electron diffusion out of the excited region. This dynamic process can be well-described by the two-temperature model formulated by Anisimov *et.al.* in 1974 [16], [20]. In the case of semiconductors, after attaining the thermal equilibrium, generally these excited free carriers undergo recombination through a combined mechanism of radiative and Auger recombination. The dynamical pathway a material takes back to equilibrium from this unusual state may permit phenomena such as atomic mixing, rapid liquid-vapor separation [21], [22], etc., which are generally inaccessible by other means. The process of ultrafast melting of the semiconductors is then followed by a rapid amorphous re-solidification of the material [23], [24]. After the melt formation and before thermal expansion occur, extreme pressure gradients form at the air-liquid and liquid-bulk interfaces accumulating a tensile stress which further leads to the spallation of the melt liquid layer resulting in material removal from the surface. Different arguments can be found regarding the exact physical mechanisms, from photons to kinetic energy of vapor, photoemission (atomic, ionic, and molecular) to aerosol formation that are not yet completely established and still investigated both theoretically and experimentally. Effects such as alteration in crystal structure resulting in amorphous layer formations are also encountered as a result of such interactions [24].

1.4 Ultrashort laser induced surface structures

The material removal resulting from laser ablation leaves a comparatively rough surface depending on the rate of ablation. Moreover, several kind of surface features are generated on the irradiated sample as a result of material removal. As a matter of fact, these surface features show a close correlation with various beam parameters as well as intrinsic physical properties of the target. The generated surface features are generally referred as laser induced surface structures. Moreover, these structures usually are found to be decorated with nanoparticles coming from the backward flux of ablated plume when irradiation is carried out at ambient pressure. While mentioning about the laser surface structuring, it is rather important to note that for laser fluence near the material

ablation threshold the morphological arrangement of the structures tends to follow a particular order. Many surface structures tend to be quasi-periodic and are generally identified as “laser induced periodic surface structures” or LIPSS. LIPSS formation is one of the most investigated surface phenomenon from the time of their first observation by Birnbaum *et.al* [25]. It is worth to mention that it is possible to control the geometry of the structures by precisely controlling laser parameters as polarization, number of pulses, pulse energy, angle of incidence and so on [3], [26], [27], that makes the process very flexible. Fig. 1.2 report examples of SEM images of Au and Pt samples displaying the great difference in the generated surface features with beam incidence angle ‘ θ ’ [28]. The ambient of the process provides a further way to influence the spatial distribution of these structures [29]. Surface morphology is a key factor in numerous physical properties of a solid surface (e.g. optical, mechanical, wetting, chemical and biological [3]), therefore direct laser surface structuring is a striking tool since it can possibly offer feasible and effective ways to tailor or control material functionalities.

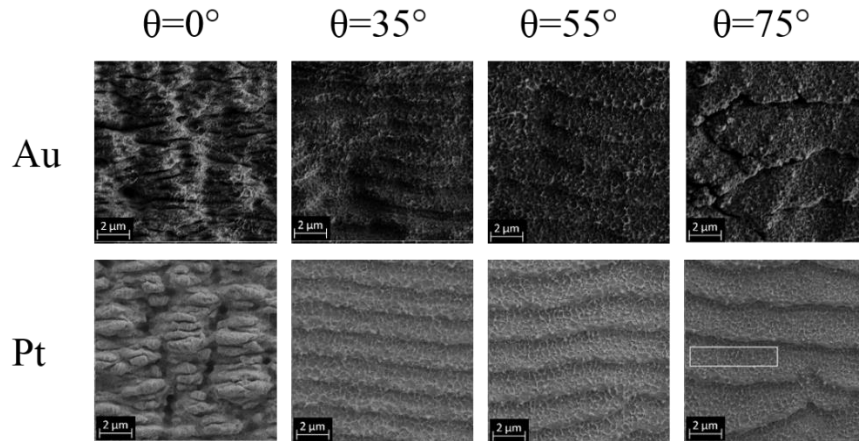


Figure 1.2| SEM images of NC-LIPSSs formed on Au and Pt following femtosecond laser irradiation at different angle of incidence $\theta=0^\circ$, 35° , 55° and 75° [28]. NC stands for nanoparticles-covered LIPSS.

The terminology LIPSS usually refers to ripples with a regular quasi-periodic structure, a period in the order of the laser wavelength and a preferential orientation along the normal to the incident laser polarization. Apart from ripples structure a very fine pattern with spatial period much lower than that of the ripples is also observed in some cases around lower intensity part of the beam. In contrast, recently a new relatively larger quasi-periodic structure, whose preferential alignment is in the direction of the laser polarization, has gained considerable attention. These structures are identified with a spatial period much larger than ripples and are formed in the high intensity part

of the beam. The formation of ripples on metals is often explained by the interference of the incident laser light with a surface scattered wave, which in some cases can be depicted as propagating excited surface plasmon polaritons (SPP), that results in an inhomogeneous energy distribution on the surface [30]. For a linearly polarized laser light, the period Λ of the LIPSSs on a metal placed in a dielectric medium is given by [3], [31],

$$\Lambda = \frac{\lambda_{las}}{Re[\eta] \pm \sin(\theta)} \quad (1)$$

where λ_{las} is the incident laser light wavelength, θ is the angle of the incident light, $\eta = \sqrt{\frac{\epsilon_d \epsilon_{metal}}{\epsilon_d + \epsilon_{metal}}}$, is the effective refractive index of the dielectric-metal interface (ϵ_d is the dielectric constant of the ambient dielectric medium, ϵ_{metal} is the dielectric constant of the metal, $Re[\eta]$ is the real part of η). Further details regarding theoretical modeling of surface structure formation and experimental results are reported in chapter 2.

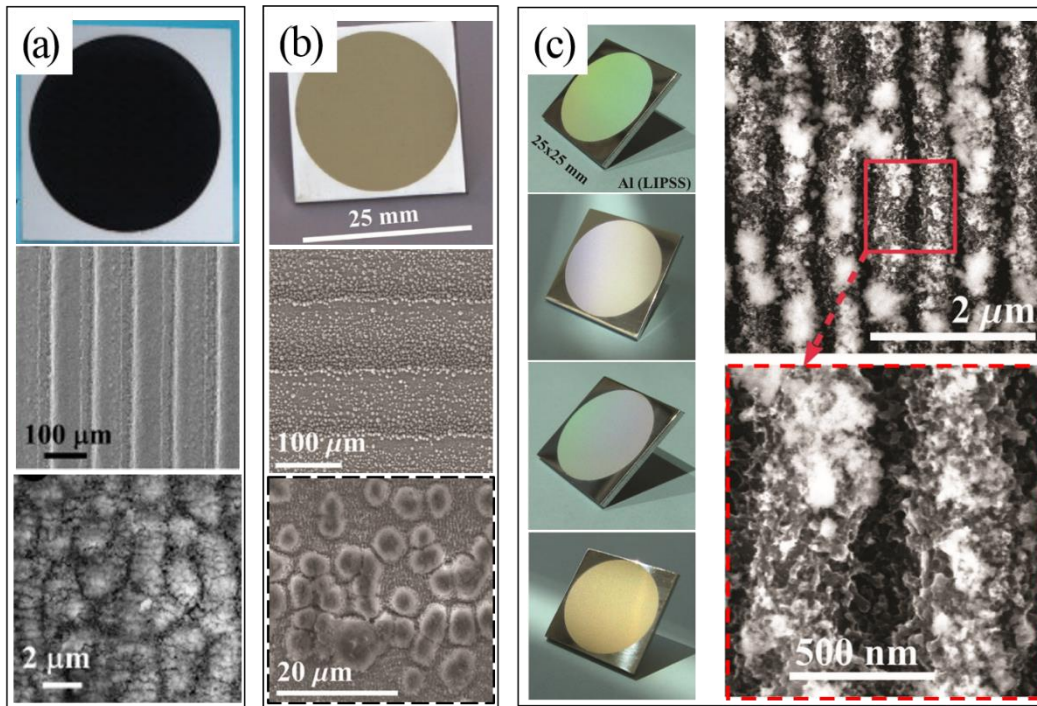


Figure 1.3| Colored Si and Al produced by femtosecond laser pulse processing. (a) black silicon – the lower panels are SEM images of the black silicon surface at different resolution. (b) golden aluminum with a laser fluence of 0.16 J/cm^2 -. The golden appearance is independent of viewing angle. The lower panels report SEM images showing surface features of the golden aluminum. (c) left panels show photographs of the same Al sample processed at comparatively lower fluence (0.05 J/cm^2), which exhibits various colors depending on the viewing angle, and the corresponding SEM images of the Al surface is given in right panel with zoomed view of the marked region in red [32], [33].

Ultrafast laser processing allows generating various kind of surface structures with limited processing environment compared to traditional methods, like lithographic techniques, opening a novel method with tremendous possible applications ranging from permanent colorization of the metal surface [3], [32], [33] to various other cutting edge technologies. Moreover, the minimum HAZ for fs laser interaction realizes the fabrication of least possible feature size with maximizing the precision of material processing. The fabrication of black silicon using laser assisted method can be envisioned as a breakthrough step considering the increased absorption (~90%) achieved by the processed silicon surface [21], [34]. Fig. 1.3 shows examples of permanent colorization of materials by fs laser processing. Part (a) of Fig. 1.3 concerns black silicon generated by scanning fs beam. The processed region looks like black irrespective of viewing angles and the surface shows a minimum reflection in visible region (below 5%) with a comparatively weak effect at long wavelengths [32]. Panel (b) of Fig. 1.3 shows a golden colored aluminum produced by scanning the surface with a laser fluence of 0.16 J/cm^2 and a pulse repetition rate of 100 Hz. Once processed, the aluminum surface appears golden at all viewing angles. Irradiation with a comparatively lower fluence of 0.05 J/cm^2 with a repetition rate of 83 Hz results in the formation of Al surface that shows appearance of different colors while viewing at different angles, as given in section (c) of the Fig. 1.3 [33]. Direct laser surface processing has also demonstrated capability in fabricating surfaces with advanced wetting properties, such as super-hydrophilic and super-hydrophobic surfaces as well as the super-wicking surfaces that can make liquid runs vertically uphill [3].

Fig. 1.4 reports two examples of surface processing with fs optical vortex (OV) beams. OVs are light beams carrying a definite orbital angular momentum (OAM) being characterized by a helical wave-front and spatially varying polarization patterns [35]. More details regarding the OV beam and its generation schemes will be given in chapter 2. The left panel of part (a) displays the SEM image of a silicon needle fabricated by irradiation with 12 overlaid pulses. The magnified image of the needle tip is shown in the inset. The measured height, length and thickness of the needles at different number overlaid vortex pulses are provided in the right panel, which shows a maximum achieved height of $\sim 40 \mu\text{m}$ [36]. In another work, Toyoda *et.al.* reported the fabrication of chiral needle by direct transfer of orbital helicity to the metal, as displayed in the lower panel of Fig. 1.4. SEM images of the surface irradiated using circularly polarized (b) and linearly polarized (c) OV beams are shown in Fig. 1.4, while panel (d) reports the magnified image of a chiral nanoneedle with a spiral cone fabricated at center of ablated zone [37].

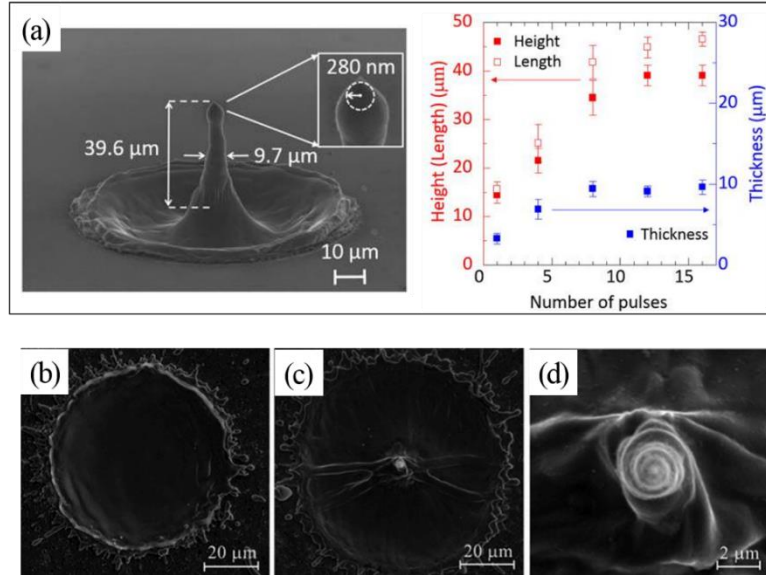


Figure 1.4| (a) Left panel shows the silicon needle fabricated by irradiation with a vortex beam. The inset shows a magnified silicon needle tip. Right panel gives the experimental height (red square), length (open square) and thickness (blue square) of the needles as a function of the number of overlaid pulses [38]. Lower panel displays the SEM images of surfaces irradiated by (b) circularly polarized and (c) linearly polarized optical vortex beams. (d) Magnified image of a chiral nano-needle with a spiral cone fabricated at center of ablated zone [37].

1.5 Overview of our experiments in surface structuring of silicon

As a matter of fact, a number of mechanisms have been considered as responsible for ripples formation by ultrashort laser pulse irradiation. In spite of surface scattered wave theory, many other mechanisms have also been proposed including excitation of surface plasmon polaritons (SPPs), self-organization of surface instabilities, second-harmonic generation, etc. [3], [39]. However, no widespread consensus has been reached yet on ripples formation mechanisms. Recently, the development of other, supervening quasi-periodic surface structures, named as grooves, was reported in semiconductors (Si and InP, e.g.) irradiated by a large number of laser pulses, and at higher fluence than ripples [40]. In fact, there is still no specific explanation for the grooves generation. Finally, most of the studies on fs laser surface structuring of silicon are carried out in air. In the case of high vacuum, seldomly analyzed earlier and reported in some experiments done in this thesis, the formation of a peculiar structured region and elliptically shaped ablation spot with the major axis directed along the laser polarization is also observed. These results are particularly interesting to further clarify some of the mechanisms involved in the process of direct ultrashort laser surface structuring. In particular, our findings points towards the important role

played by the re-deposited nanoparticulate debris occurring in air at atmospheric pressure on the generation of above-wavelength quasi-periodic grooves. As a second issue, let me mention that the other goal of my work is to address the merits of using novel laser beams to control and tune still further the generated surface structure by exploiting fs vector beams.

In our experiments, we treated a well-polished silicon (100) surface with ultrashort laser pulses in various conditions, which also include different state of beam polarization, for the sake of observing the nature of the surface modification and its dependence on the various parameters. The totality of the results indicates formation of diverse kind of surface structures including ordered and randomly distributed surface features. We focus our attention on two main quasi-periodic surface patterns that are characterized by different spatial alignment and sizes. From the morphological characteristics, these features are identified as classical ripples and micron-sized grooves. Each specified structure is richly decorated with nanoparticles in the case of processing in ambient air, which for instance allows elaborating micron-scale structured surfaces possessing also nano-scale roughness that are ideal to implement multi-functional properties.

Among other, the main novel aspect of this thesis is on the use of an unconventional beam, e.g. an OV with definite orbital angular momentum (OAM) [41]. An OV (also known as a screw dislocation or phase singularity) is one type of optical singularity that has a spiral phase wavefront around a singularity point where the phase is undefined. We made use of a special optical element called *q-plate* in order to generate the mentioned OV beam. The spiral phase of vortex beams rotates about the optical axis that causes the wavefront of the light to twist like a corkscrew as it propagates. The q is defined as the topological charge of the vortex, which in turn defines how many twists the light experiences in one wavelength of propagation. The number of topological charge can be positive or negative, depending on the handedness of the twist in left (anticlockwise) or right (clockwise) direction. Furthermore, a different state of polarization inside the annular beam is obtained using a set of wave plates before and after the q -plate, along the optical path. In order to study the effect of ambient pressure, experiments are also carried out in reduced pressure values down to 10^{-4} mbar. Throughout the work weak focusing conditions are used, avoiding all effects involved with tight focus [42]. In particular, in most of our surface structuring experiments an OV beam with OAM $m=1$ is used. However, some examples of surface patterns generated with beam with higher values of the OAM are also included. In the last case, higher the number of twist

per λ the faster the light spinning around the optical axis, which usually makes the singularity larger resulting in an ablation crater with larger non-ablated central region. Moreover, asymmetric beams are also generated by tuning the optical retardation of the q-plate. This results in more complex surface patterns on the silicon surface with lopsided features.

Recently, potential beam shaping applications of vortex beams superimposed with a Gaussian beam to compensate the central dark hollow intensity distribution generating a flat-top spatial profile has been addressed as an undeniable tool for uniform surface processing, laser weapons, optical data processing, etc. [43]. Finally, remarkable advantages inherent to laser based techniques are speed and scalability in achieving surface processing and operating in ambient air. Since the structuring remarkably increases the effective surface area, this could be a potential method for numerous real world applications.

References

- [1] R. Russo, X. Mao, J. Gonzalez, and J. Yoo, "Femtosecond vs. nanosecond laser pulse duration for laser ablation chemical analysis," *Spectroscopy*, vol. 28, no. 1, pp. 24–39, 2013.
- [2] E. G. Gamaly, "The physics of ultra-short laser interaction with solids at non-relativistic intensities," *Phys. Rep.*, vol. 508, no. 4, pp. 91–243, 2011.
- [3] A. Y. Vorobyev and C. Guo, "Direct femtosecond laser surface nano/microstructuring and its applications," *Laser Photon. Rev.*, vol. 7, no. 3, pp. 385–407, May 2013.
- [4] F. Brech and L. Cross, "Optical microemission stimulated by a ruby maser," *Appl. Spectrosc.*, vol. 16, no. 59, p. 59, 1962.
- [5] S. Amoruso, R. Bruzzese, N. Spinelli, and R. Velotta, "Characterization of laser-ablation plasmas," *J. Phys. B At. Mol. Opt. Phys.*, vol. 32, no. 14, pp. R131–R172, Jul. 1999.
- [6] S. Amoruso, G. Ausanio, R. Bruzzese, M. Vitiello, and X. Wang, "Femtosecond laser pulse irradiation of solid targets as a general route to nanoparticle formation in a vacuum," *Phys. Rev. B*, vol. 71, no. 3, p. 33406, Jan. 2005.
- [7] S. S. Harilal, C. V. Bindhu, M. S. Tillack, F. Najmabadi, and A. C. Gaeris, "Internal structure and expansion dynamics of laser ablation plumes into ambient gases," *J. Appl. Phys.*, vol. 93, no. 5, pp. 2380–2388, Mar. 2003.
- [8] D. W. Koopman, "Langmuir Probe and Microwave Measurements of the Properties of Streaming Plasmas Generated by Focused Laser Pulses," *Phys. Fluids*, vol. 14, no. 8, p. 1707, 1971.
- [9] D. Umstadter, S. Chen, and A. Maksimchuk, "Experimental observation of relativistic nonlinear Thomson scattering," *Nature*, vol. 396, no. 6712, pp. 653–655, Dec. 1998.
- [10] K. Goda, K. K. Tsia, and B. Jalali, "Serial time-encoded amplified imaging for real-time observation of fast dynamic phenomena," *Nature*, vol. 458, no. 7242, pp. 1145–1149, Apr. 2009.

- [11] K. Nakagawa, A. Iwasaki, Y. Oishi, R. Horisaki, A. Tsukamoto, A. Nakamura, K. Hirose, H. Liao, T. Ushida, K. Goda, F. Kannari, and I. Sakuma, “Sequentially timed all-optical mapping photography (STAMP),” *Nat. Photonics*, vol. 8, no. 9, pp. 695–700, Aug. 2014.
- [12] D. W. Bäuerle, *Laser processing and chemistry*. Springer Science & Business Media, 2013.
- [13] IMRA - The Femtosecond Fiber Laser Company, “Materials Processing.” [Online]. Available: <http://www.imra.com/applications/application-areas/materials-processing/>.
- [14] S. S. Harilal, J. R. Freeman, P. K. Diwakar, and A. Hassanein, “Femtosecond Laser Ablation: Fundamentals and Applications,” Springer Berlin Heidelberg, 2014, pp. 143–166.
- [15] B. Rethfeld, K. Sokolowski-Tinten, D. von der Linde, and S. I. Anisimov, “Timescales in the response of materials to femtosecond laser excitation,” *Appl. Phys. A*, vol. 79, no. 4–6, pp. 767–769, Sep. 2004.
- [16] J. K. Chen, D. Y. Tzou, and J. E. Beraun, “A semiclassical two-temperature model for ultrafast laser heating,” *Int. J. Heat Mass Transf.*, vol. 49, no. 1, pp. 307–316, 2006.
- [17] J. S. Graves and R. E. Allen, “Response of GaAs to fast intense laser pulses,” *Phys. Rev. B*, vol. 58, no. 20, pp. 13627–13633, Nov. 1998.
- [18] A. M. Lindenberg, J. Larsson, K. Sokolowski-Tinten, K. J. Gaffney, C. Blome, O. Synnergren, J. Sheppard, C. Coleman, A. G. Macphie, D. Weinstein, D. P. Lowney, T. K. Allison, T. Matthews, R. W. Falcone, A. L. Cavalieri, D. M. Fritz, S. H. Lee, P. H. Bucksbaum, D. A. Reis, J. Rudati, P. H. Fuoss, C. C. Kao, D. P. Siddons, R. Pahl, J. Als-Nielsen, S. Duesterer, R. Ischebeck, H. Schlarb, H. Schulte-Schrepping, T. Tschentscher, J. Schneider, D. von der Linde, O. Hignette, F. Sette, H. N. Chapman, R. W. Lee, T. N. Hansen, S. Techert, J. S. Wark, M. Bergh, G. Huldt, D. van der Spoel, N. Timneanu, J. Hajdu, R. A. Akre, E. Bong, P. Krejcik, J. Arthur, S. Brennan, K. Luening, and J. B. Hastings, “Atomic-scale visualization of inertial dynamics,” *Science (80-.)*, vol. 308, no. 5720, pp. 392–395, 2005.
- [19] X. Y. Wang, D. M. Riffe, Y.-S. Lee, and M. C. Downer, “Time-resolved electron-temperature measurement in a highly excited gold target using femtosecond thermionic emission,” *Phys. Rev. B*, vol. 50, no. 11, pp. 8016–8019, Sep. 1994.
- [20] S. Anisimov, B. Kapeliovich, and T. Perelman, “Electron emission from metal surfaces exposed to ultrashort laser pulses,” *Zh. Eksp. Teor. Fiz.*, vol. 66, pp. 776–781, 1974.
- [21] A. Serpenguzel, A. Kurt, I. Inanc, J. Carey, and E. Mazur, “Luminescence of black silicon,” *J. Nanophotonics*, vol. 2, no. 1, p. 21770, Feb. 2008.
- [22] D. A. Reis, K. J. Gaffney, G. H. Gilmer, and B. Torralva, “Ultrafast Dynamics of Laser-Excited Solids,” *MRS Bull.*, vol. 31, no. 8, pp. 601–606, Aug. 2006.
- [23] P. Saeta, J.-K. Wang, Y. Siegal, N. Bloembergen, and E. Mazur, “Ultrafast electronic disordering during femtosecond laser melting of GaAs,” *Phys. Rev. Lett.*, vol. 67, no. 8, pp. 1023–1026, Aug. 1991.
- [24] J. Bonse, K. W. Brzezinka, and A. J. Meixner, “Modifying single-crystalline silicon by femtosecond laser pulses: An analysis by micro Raman spectroscopy, scanning laser microscopy and atomic force microscopy,” *Appl. Surf. Sci.*, vol. 221, no. 1–4, pp. 215–230, 2004.
- [25] M. Birnbaum, “Semiconductor Surface Damage Produced by Ruby Lasers,” *J. Appl. Phys.*, vol. 35, no. 11, pp. 3688–3689, 1965.
- [26] J. Bonse and J. Krüger, “Pulse number dependence of laser-induced periodic surface structures for femtosecond laser irradiation of silicon,” *J. Appl. Phys.*, vol. 108, no. 3, p. 34903, 2010.

- [27] G. D. Tsibidis, E. Stratakis, P. A. Loukakos, and C. Fotakis, “Controlled ultrashort-pulse laser-induced ripple formation on semiconductors,” *Appl. Phys. A Mater. Sci. Process.*, vol. 114, no. 1, pp. 57–68, 2014.
- [28] T. Y. Hwang and C. Guo, “Angular effects of nanostructure-covered femtosecond laser induced periodic surface structures on metals,” *J. Appl. Phys.*, vol. 108, no. 7, p. 73523, Oct. 2010.
- [29] D. N. Kuladeep, Rajamudili and Dar, Mudasir H and Deepak, KLN and Rao, “Ultrafast laser induced periodic sub-wavelength aluminum surface structures and nanoparticles in air and liquids,” *J. Appl. Phys.*, vol. 116, no. 11, p. 113107, 2014.
- [30] J. E. Sipe, J. F. Young, J. S. Preston, and H. M. van Driel, “Laser-induced periodic surface structure. I. Theory,” *Phys. Rev. B*, vol. 27, no. 2, pp. 1141–1154, Jan. 1983.
- [31] A. M. Bonch-Bruевич, M. N. Libenson, V. S. Makin, and V. V. Trubaev, “Surface electromagnetic waves in optics,” *Opt. Eng.*, vol. 31, no. 4, p. 718, 1992.
- [32] A. Y. Vorobyev and C. Guo, “Direct creation of black silicon using femtosecond laser pulses,” *Appl. Surf. Sci.*, vol. 257, no. 16, pp. 7291–7294, 2011.
- [33] A. Y. Vorobyev and C. Guo, “Colorizing metals with femtosecond laser pulses,” *Appl. Phys. Lett.*, vol. 92, no. 4, p. 41914, Jan. 2008.
- [34] C. Wu, C. H. Crouch, L. Zhao, J. E. Carey, R. Younkin, J. A. Levinson, E. Mazur, R. M. Farrell, P. Gothoskar, and A. Karger, “Near-unity below-band-gap absorption by microstructured silicon,” *Appl. Phys. Lett.*, vol. 78, no. 13, pp. 1850–1852, Mar. 2001.
- [35] L. Marrucci, C. Manzo, and D. Paparo, “Optical spin-to-orbital angular momentum conversion in inhomogeneous anisotropic media,” *Phys. Rev. Lett.*, vol. 96, no. 16, p. 163905, 2006.
- [36] F. Takahashi, K. Miyamoto, H. Hidai, K. Yamane, R. Morita, and T. Omatsu, “Picosecond optical vortex pulse illumination forms a monocrystalline silicon needle,” *Sci. Rep.*, vol. 6, p. 21738, Feb. 2016.
- [37] K. Toyoda, F. Takahashi, S. Takizawa, Y. Tokizane, K. Miyamoto, R. Morita, and T. Omatsu, “Transfer of Light Helicity to Nanostructures,” *Phys. Rev. Lett.*, vol. 110, no. 14, p. 143603, Apr. 2013.
- [38] F. Takahashi, K. Miyamoto, H. Hidai, K. Yamane, R. Morita, and T. Omatsu, “Picosecond optical vortex pulse illumination forms a monocrystalline silicon needle,” *Sci. Rep.*, vol. 6, p. 21738, Feb. 2016.
- [39] K. Sugioka and Y. Cheng, “Ultrafast lasers—reliable tools for advanced materials processing,” *Light Sci. Appl.*, vol. 3, no. 4, p. e149, Apr. 2014.
- [40] G. D. Tsibidis, C. Fotakis, and E. Stratakis, “From ripples to spikes: A hydrodynamical mechanism to interpret femtosecond laser-induced self-assembled structures,” *Phys. Rev. B - Condens. Matter Mater. Phys.*, vol. 92, no. 4, p. 41405, 2015.
- [41] J. JJ Nivas, S. He, A. Rubano, A. Vecchione, D. Paparo, L. Marrucci, R. Bruzzese, and S. Amoroso, “Direct Femtosecond Laser Surface Structuring with Optical Vortex Beams Generated by a q-plate,” *Sci. Rep.*, vol. 5, p. 17929, Dec. 2015.
- [42] C. Hnatovsky, V. G. Shvedov, N. Shostka, A. V. Rode, and W. Krolikowski, “Polarization-dependent ablation of silicon using tightly focused femtosecond laser vortex pulses,” *Opt. Lett.*, vol. 37, no. 2, p. 226, Jan. 2012.
- [43] F. Dickey, T. Lizotte, S. Holswade, and D. Shealy, *Laser beam shaping applications*. CRC Press, 2005.

Experimental methods

“This chapter illustrates experimental methods used in fs-laser surfaces structuring experiments. In particular, the laser sources and the method used to generate optical vortex (OV) beams using q-plate will be discussed. Moreover, it includes a brief description of sample material, optical setup and instrumentations for surface structuring with different kind of fs laser beams and surface characterization.”

2.1 Introduction

Femtosecond lasers provide a versatile tool for micro- and nano-fabrication, which over the past decade has received a great amount of research attention due to numerous advantages. One of the main aspect is that all kind of materials (metals, semiconductors, glasses, and polymers) can be processed, even with non-planar surfaces. Another important point is the capability of generating a wide variety of surface structures, whose size ranges from nano- to micro-scale. Moreover, unlike other techniques, e.g. lithography, this method does not require any clean room facility and is a single step process [1]. Also, laser structuring does not make use of chemical reagents or produce significant waste, unlike other conventional methods. In addition, the short temporal duration of the fs pulse offers high control and precision over the produced geometry [2].

The present thesis deals with direct fs laser surface structuring by exploiting either standard laser beams with a Gaussian spatial profile or unconventional beams such as OV beam. OVs are beams carrying an OAM and can have various states of polarization (e.g. azimuthal, radial, spiral, etc.). In the present work, they are generated by using a converter based on a q-plate, an optical device which will be described in the next section [3]. Besides Gaussian and OV beams, which present a symmetric distribution of the spatial intensity, also asymmetric beams are generated by the q-plate device and used for surface structuring [4]. The processing is mainly carried out in ambient air

conditions, but some experiments in high vacuum are also discussed addressing some very peculiar features of the structuring process [5].

2.2 OAM and generation of fs OV beams

The electromagnetic wave carries not only energy but also momentum, and this can be either linear or angular. In agreement with classical electrodynamics and quantum mechanics, light possesses linear momentum. For instance, it is recognized as responsible for radiation pressure, a fascinating property of light. In experiments revealing radiation pressure, a light beam transfers its momentum to an absorbing or scattering object, generating a mechanical pressure on it [6]. In accordance with the quantum theory of light, each photon in addition to its linear momentum $p=h/\lambda$ has also an intrinsic angular momentum equal to \hbar . Angular momentum of light indicates the amount of dynamic rotation present in the light field. The two discrete forms of degrees of freedom are spin angular momentum (SAM) and OAM. The former is associated with the spin of the transverse electric field and may take the values $s=\pm\hbar$ per photon [7], [8]. SAM depends only on polarization of the beam and not on its phase [9]. In fact, SAM is associated with the circular or elliptical polarization. So a beam carrying SAM can be easily generated by using a quarter wave plate to convert linear to circularly polarized light. OAM is associated with the optical phase structure of the complex electric field. It is related to helical shape of the wave front. It was found in early 1992 that a light beam with an azimuthal phase dependence $\exp(-im\phi)$ carries an angular momentum independent of its polarization state, where m can take any integer value (positive or negative) and the angle ' ϕ ' is the azimuthal co-ordinate in the beam's cross section [6]–[8]. Unlike SAM, OAM is independent of the beam polarization and depends on spatial distribution of the field. OAM has a value $m\hbar$ per photon and its sign gives the handedness of the beam helical phase. In general, the total angular momentum of any light field is obtained by the sum of these spin and orbital angular momenta. With the help of some optical devices, it is possible to convert SAM to OAM and generate special kind of beams with a helical phase. An OV is one kind of such unconventional beams. These beams are characterized by a spiral wave front, a singularity on the axis, where the phase is undefined, and carries a definite OAM. There are many methods to generate beams carrying OAM. These include spiral phase plate [10], astigmatic lens converter, computer generate fork hologram [11] and spatial light modulator (SLM) [12], [13]. In our case,

we adopt a special optical component called *q-plate*, where ‘*q*’ stands for charge of the vortex. In the next sections, the *q-plate* and the method to generate vortex beams will be illustrated.

2.2.1 The *q-plate*

The light converter we used is an electrically tunable *q-plate*. In specific, *q-plate* is an optical device based on liquid crystal (LC) technology. It is basically a birefringent wave plate with inhomogeneous patterned distribution of optical axis in the transverse plane, which is able to generate and manipulate light OAM [3], [7], [14]. In a *q-plate*, a LC film is enclosed between two glass walls perpendicular to the light propagation axis. The orientation of the local optic axis of the *q-plate* is given by the LC molecular director distribution [8], whose pattern is defined by means of a parameter called the topological charge ‘*q*’. Initially *q-plates* with only $q=1$ were developed by using a planar cell of LC with a thickness of about $1\ \mu\text{m}$ of material (*E63 from Merck, Darmstadt, Germany*) sandwiched between two plane glasses so as to obtain a birefringence retardation of approximately a half-wave. Before assembly, the inner surfaces of the two glasses were coated with a polyimide for planar alignment and for parallel strong anchoring, and one of them was briefly pressed against a piece of fabric kept in continuous rotation. The liquid crystals arrange in direction normal (or parallel, depending on the LC type) to the rubbing direction. The orientation of the LC molecules can be controlled in any preferred direction. The $q = 1$ *q-plates*, with circular symmetric direction of optical axis, can be manufactured in this way. For other patterns, with $q \neq 1$, photo alignment technique is carried out [8].

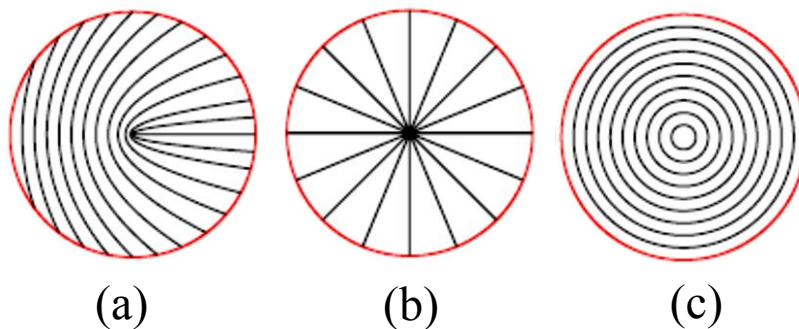


Figure 2.1/ Examples of *q* plates. The tangent to the lines shown indicates the local direction of the optic axis. (a) $q=1/2$ and $\alpha_0=0$ (a nonzero α_0 is here just equivalent to an overall rigid rotation), which generates helical modes with $m=\pm 1$; (b) $q = 1$ with $\alpha_0=0$ and (c) with $\alpha_0= \pi/2$, which can both be used to generate modes with $m=\pm 2$. The last two cases correspond to rotationally symmetric plates, giving rise to perfect spin-to-orbital angular momentum conversion, with no angular momentum transfer to the plate.

When a left-circular polarized plane wave passes through a q-plate with optical charge ‘ q ’, the wave emerging from the plate is uniformly right-circular polarized, as would occur for a normal $\lambda/2$ wave plates, but it also acquires a phase factor $\exp(im\phi)$, with $m=2q$; i.e., it has been transformed into a helical wave with orbital helicity $2q$ and OAM= $2q\hbar$ per photon. In case of a right-circular input wave, orbital helicity and OAM of the outgoing wave are sign-inverted. In other words, the input polarization of the light controls the sign of the orbital helicity of the output wave front as schematically shown in Fig. 2.2. The magnitude $|m|$ is fixed by the birefringence axis geometry. During the passage each photon being converted from left-circular to right-circular changes its spin z-component angular momentum from $+\hbar$ to $-\hbar$. In the case of a q-plate with $q = 1$, the orbital z-component angular momentum of each photon changes instead from zero to $2q$. Therefore, the total variation of the angular momentum of light is nil, and there is no net transfer of angular momentum to the plate. The plate in this case acts only as a “coupler” of the two forms of optical angular momentum, allowing their conversion into each other. This exact compensation of the spin and orbital angular momentum exchanges with matter is clearly related to the circular symmetry (rotation invariance) of the $q= 1$ plate. So for a beam of light passing through a q-plate with topological charge q and phase retardation δ , a particular part of photons defined by the fraction $\sin^2 \frac{\delta}{2}$ reverses their SAM (in effect flipping their spin from -1 to $+1$) simultaneously hanging their OAM by an amount of $\pm 2q$. The remaining photon fraction $\cos^2 \frac{\delta}{2}$ remains unaffected. When the phase retardation of the q-plate is tuned to half-wave ($\delta = \pi$) all the input photons will be converted. In the particular case of charge $q = 1$, the total SAM+OAM light angular momentum remains unchanged in passing through the q-plate, so that the change of the photon SAM is transferred into a corresponding opposite change of the photon OAM, yielding a spin-to-orbital conversion (STOC) of the angular momentum. If $q \neq 1$, the plate is not symmetric and will exchange an angular momentum of $\pm 2\hbar(q-1)$ with each photon, with a sign depending on the input polarization. Therefore, in this general case, the angular momentum will not be just converted from spin to orbital, but the spin degree of freedom will still control the “direction” of the angular momentum exchange with the plate, besides the sign of the output wave-front helicity.

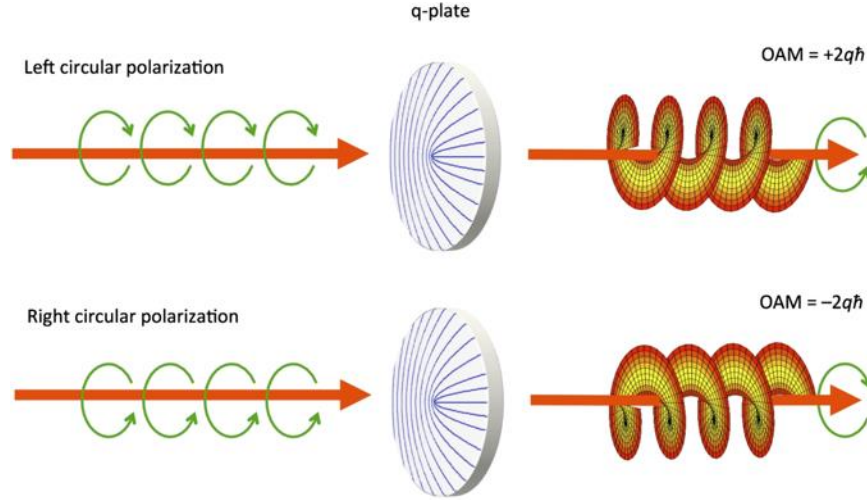


Figure 2.2/ Schematics of the optical effect of a q-plate. Left (right) circularly polarized light having zero OAM at the input is converted into light carrying an OAM per photon given by $+2q\hbar$ ($-2q\hbar$). The circular polarization handedness gets also inverted in the process [14].

2.2.2 Generation and optimization of OV beam with q plate

In order to generate a good quality OV beam we need to provide a perfect working condition to the q-plate. The two parameters to which q-plate is very sensitive are voltage applied between the two plates filled with liquid crystal and the temperature. In fact, while changing the applied voltage, which is a square wave optimized at 11 kHz, we actually tune the optical birefringent retardation ' δ ' of the q-plate. A tuned q-plate ($\delta = \pi$) shined with linearly polarized Gaussian beams allows generating cylindrically symmetric OV beams, e.g. radial and azimuthal.

The left panel of Fig. 2.3 shows a simple schematics of the optical arrangement exploited for optimizing the q-plate conversion. It consists of a two sets of $\lambda/4$ wave plates and polarizer ($GLP_{(I)}, \lambda/4_{(I)}$, ($\lambda/4_{(II)}, GLP_{(II)}$) located before and after the q-plate. In order to attain the exact δ , the amplitude of the applied voltage (V_{pp}) is continuously varied while simultaneously monitoring the laser energy along the beam path.

The first part of the optimization procedure is carried out without the q-plate. $GLP_{(I)}$ and $GLP_{(II)}$ are set to transmit only horizontal (H) and vertical (V) polarization, respectively. The optic axis of $\lambda/4_{(I)}$ is rotated 45° with respect to the direction of incoming linear polarization so that the beam polarization to the q-plate is always circular. As we know, for circularly polarized beam the q-plate conversion efficiency is maximum because of its relation to SAM and thus to polarization of the beam. Then, the beam after the $\lambda/4_{(I)}$ is circularly polarized. The axis of the $\lambda/4_{(II)}$ is rotated to 90° so that it converts back the circularly polarized beam to linear again (i.e. $\lambda/4_{(I)}$ at -45° and

$\lambda/4_{(II)}$ at $+45^\circ$). Now the insertion of a q-plate tuned at an optical retardation of $\lambda/2$ (i.e. $\delta = \pi$) will generate an annular beam with a linear polarization preferentially aligned in the vertical direction. This condition is achieved by continuously monitoring the beam energy after $GLP_{(II)}$ while varying the q-plate voltage. In fact, the fraction of input beam converted to an annular beam presents a V-polarization and is transmitted through $GLP_{(II)}$, while the unconverted part will keep a H-polarization. Hence, an optical retardation of $\lambda/2$ (i.e. $\delta = \pi$) will be associated with a maximum in the registered signal that occurs at a voltage for which the q-plate provides its maximum conversion from the input Gaussian beam to an OV. The measured variation of the transmitted energy as a function of the q-plate voltage is displayed in the right panel of Fig. 2.3.

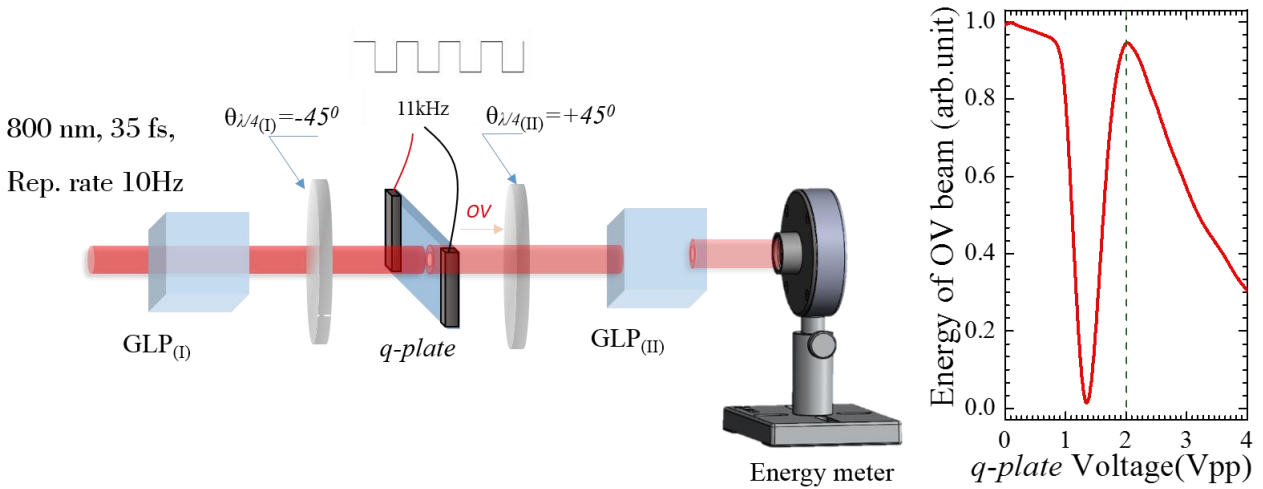


Figure 2.3/ Schematics of experimental setup showing optimization scheme followed with q-plate, $\lambda/4$ wave plates and polarizers. Graph provided in the right side corresponds to the normalized energy of OV beam passing $GLP_{(II)}$ as a function of the q-plate voltage.

In the measured OV beam energy vs voltage shown in Fig. 2.3, there are two regions at which the conversion to OV beam is maximum. The second peak at relatively higher voltage ($\sim 2.08 V_{pp}$) is found to be more stable over long working time and less sensitive to temperature effects. So in our experiments, the q-plate is operated at a driving signal voltage $2.08 V_{pp}$, which provides a value of $\delta = \pi$. This voltage values can slightly vary from time to time due to some local variations of liquid crystals and ambient parameters like temperature, humidity, etc.

2.3 Characterization of fs Gaussian and OV beams for surface structuring

An OV beam is a beam with annular intensity distribution in the transverse plane carrying a specific OAM whose values are quantized. In most of our experiments, optical beams with $m=+1$, are produced by a q -plate with a topological charge of $q = +1/2$. We have also performed experiments with q -plates having higher q values such as $q=+1$, $+5/2$ providing an OAM $m=+2$, $+5$ respectively. The generation and optimization of the OV beam by electrically tuning the q -plate are done before each set of experiments following the procedure illustrated above. More information regarding the q -plates and OV with OAM are provided in following sections.

The Gaussian beam from the laser amplifier is linearly polarized and its polarization direction can be controlled by means of a half wave-plate. The OV beam is characterized by an annular spatial profile and its state of polarization (SoP) is manipulated by appropriate rotation of the linear polarization of the Gaussian beam entering the q -plate with respect to its optic axis. Fig. 2.4 (a) and (b) report 2D maps of the spatial intensity profile corresponding to Gaussian and OV beams, respectively, generated by simulation. The OV is characterized by an annular spatial profile, with a central region of null intensity due to an undefined phase on the OV beam axis. Fig. 2.4 (c) and (d) show the normalized values of intensity distribution along the diameter for Gaussian and OV beams, respectively.

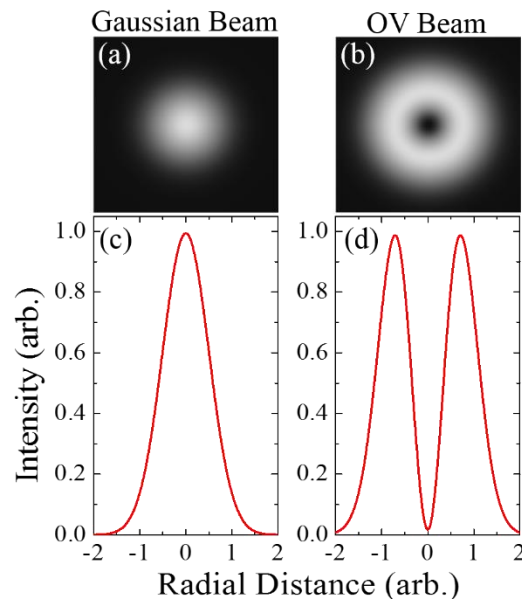


Figure 2.4| (a) and (b) show the 2D map of the beam profiles generated from the simulation and (c) and (d) show the normalized intensity profiles along the diameter for Gaussian and OV beams, respectively.

The q-plate converter allows the generation of azimuthal, radial and spiral SoP. Fig. 2.4 (d) reports the spatial profiles of the pulse fluence $F(r)$ for the OV beams, r being the spatial coordinate along the diameter, which are described as:

$$F_{OV}(r) = \frac{2^2 E_0}{\pi w_0^4} r^2 \exp\left[-\frac{2r^2}{w_0^2}\right] \quad (1)$$

where E_0 is the beam energy, w_0 the waist of the fundamental Gaussian beam [18], and the subscripts OV refer to OV beam. The fluence profile $F_{OV}(r)$ of the OV beam is null at center and shows a peak value $F_{OV,p} = 2e^{-1}E_0/\pi w_0^2 \approx 0.74E_0/\pi w_0^2$ at a radial distance $r_p = w_0/\sqrt{2}$ from the center. Moreover, the fluence reduces to $1/e^2$ of the peak value at two different locations on the two sides of the peak, namely at $r_{in} \approx 0.16 w_0$ and $r_{out} \approx 0.15 w_0$, due to the dissimilar fluence spatial gradient in the central ($r < r_p$) and external ($r > r_p$) regions of the OV beam profile. Since the formation of ripples and grooves strongly depends on the incoming beam polarization, one of the great advantages in using OV beam in surface structuring is the possibility to generate diverse state of polarization (SoP). In general radial and azimuthal are the two familiar SoPs which can be obtained by simply rotating the incoming linear polarization to the q-plate from horizontal to vertical. Moreover, many spiral state of polarizations can be obtained while varying the input polarization between these two states. Moreover, also other numerous kind of complex SoP can be achieved by adding additional optical elements in the beam path, like wave plates ($\lambda/2$ and $\lambda/4$), before and/or after the q-plate.

Several surface structuring experiments are carried out in the present work by exploiting laser pulses provided by two different fs laser systems:

- i) a re-generatively amplified Ti:Sapphire laser (*Legend, Coherent Inc.*) delivering linearly polarized ≈ 35 fs pulses at a central wavelength around 800 nm with a repetition rate of 1 kHz;
- ii) a Nd:Glass laser (*Twinkle, Light Conversion*) providing a fundamental ≈ 900 fs pulses at a wavelength of 1055 nm and repetition rate of 33 Hz.

In the experiments, the target is irradiated either with the fundamental Gaussian beam or the converted beams. In the case of structuring with Gaussian beam, both the laser systems mentioned above are utilized to carry out investigations on the diverse aspects of surface structure formation. In particular, the Nd:glass laser system is used for structuring of a target held in a vacuum chamber

at different base pressures. Meanwhile, in all the performed experiments with q-plate and OV beams, illustrated in this thesis, the Ti:Sapphire laser is used as the primary source.

2.4 Silicon-ideal material used in surface structuring

We have carried out surface structuring of different solid samples by focusing ultrafast laser beams with different irradiation conditions and beam profiles. In most of the experiments Silicon is used as a target because it is a material of great technological interest as well as its dominance in the electronics industry. The Silicon samples used in the experiments were commercial intrinsic crystalline (resistivity $> 200 \Omega \text{ cm}$) silicon (100) plate with a thickness of $400 \mu\text{m}$ (*Sil'tronix silicon Technologies*). The response of Si to laser irradiation has been studied comprehensively in the past decades [15], making it perhaps one of the world's best-characterized materials. Apart from all specifications, on interaction with fs laser Si generate almost all kind of periodic and random structures reported [16]–[20]. One of silicon most appealing characteristics for applications is the existence of two structurally different solid phases, crystalline and amorphous. Laser melting followed by fast quenching results in the amorphous state formation in silicon, while recrystallization is achieved by either thermal or laser annealing. The use of ultrashort pulses triggers non-thermal phase transition which can direct to different solidification pathways [15]. In many fundamental studies of laser surface structuring in Si with fs laser interaction, mechanisms related to the formation of periodic structures and influence of laser parameters on the spatial period and orientation of different structures are investigated experimentally as well as theoretically. There are also application-oriented studies aiming at the modification of surface properties by large area fabrication of such structures [18], [20]–[27].

As the effect of the ambient pressure has been seldom considered in earlier studies, we also investigated the effect of ambient pressure on surface structuring by performing experiments at atmospheric pressure and in vacuum conditions (down to about 10^{-5} mbar).

2.5 General experimental setup for fs laser surface structuring

Fig. 2.5 reports a schematics of the typical experimental setup. The q-plate shown in the figure will be present only when ablation is done with an OV beam and not for Gaussian beam irradiation. Both Gaussian and OV beams are focused on the target surface with a lens of $f=75 \text{ mm}$ focal length, in air. For experiments at variable pressure the target is located inside a vacuum chamber,

and a longer focal length lens ($f=200$ mm) placed outside the chamber is utilized to focus the laser beam on the sample. Pulse energy is adjusted by means of $\lambda/2$ wave plate and polarizer (GLP) as shown in the schematics of the experimental setup. An additional $\lambda/2$ wave plate is used to control the linear SoP to the q-plate and is critical since the complex OV beam polarization is defined on the basis of the angle the linear polarization of the incoming beam makes with the q-plate axis. The generation scheme of different polarization of the OV beam with the aid of wave plates ($\lambda/2$ and $\lambda/4$) along the beam path will be illustrated in chapter 4.

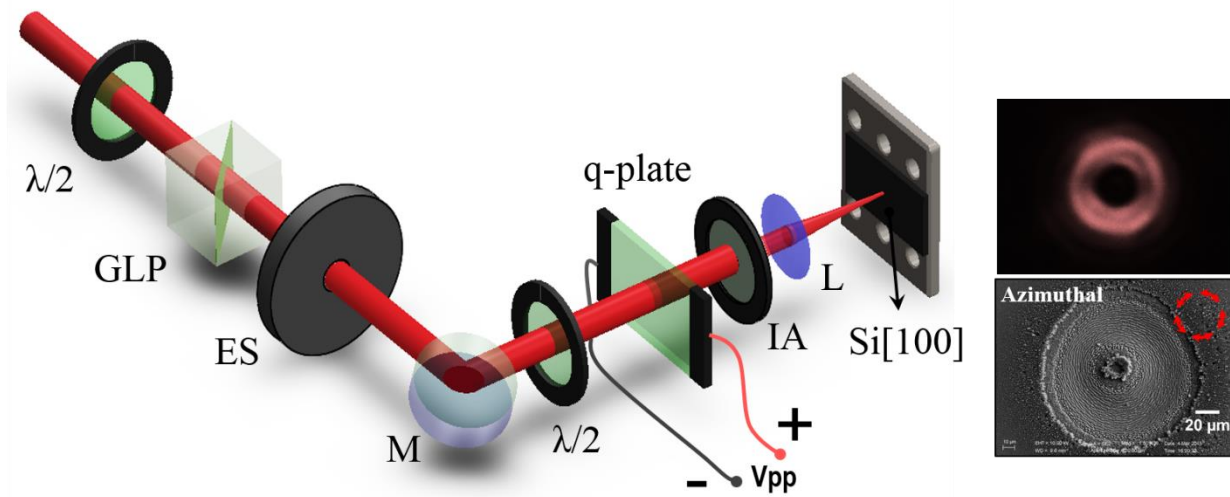


Figure 2.5| Schematic of the experimental setup used for direct laser surface structuring with fs laser beams generated by a q-plate; $\lambda/2$ =half-wave plate, GLP=Glan Laser Polarizer, ES=electro-mechanical shutter; M=mirror; IA=iris aperture; L=lens. On the right side the upper panel indicates the beam profile taken by a CCD of generated OV beam and lower panel displays a SEM image of the ablation crater after the irradiation with azimuthally polarized OV beam.

In all experiments the laser beam hits the sample surface at normal incidence. During the irradiation, the sample is mounted on a three-axis (XYZ stage) motorized nanometer precision piezo stage (PPS-20) controlled by modular motion controller (MMC-103) (Micronix-USA ltd). The entire stage is capable to move in all three direction with travel range of 20 mm at a maximum scan velocity of 2 mm/s. The stage movement is synchronized with an electromechanical shutter (Unibitz shutter, Vincent Associates) and the combined system is controlled by a custom made software. Such control provides a great hand on the selection of the desired number of laser pulses,

N, applied to the same spot on any location of the target. The synchronization and software control further provide the possibility of scanning the beam with variable velocity and programmable pattern facilitating the surface modification over large area of the sample within the limit of stage. Since the mentioned morphological patterns are well formed at near ablation threshold of the material before performing the structuring experiments on any new material the ablation threshold is characterized. The size of ablation spots are measured for different pulse energies of Gaussian beam. By fitting the plot of area of the ablated spot vs laser fluence approximate measurements of the beam waist and ablation threshold are obtained [28].

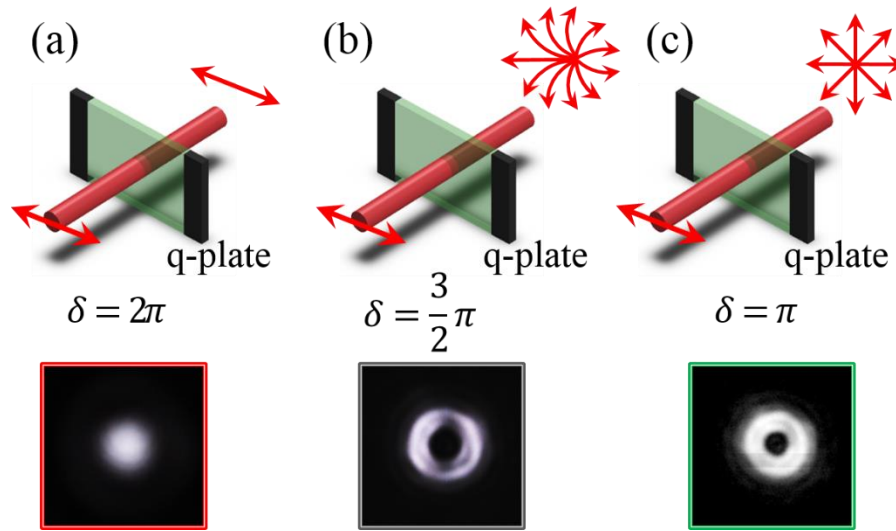


Figure 2.6: Three examples of the q-plate configurations for various optical retardations δ . (a) leads to a linearly polarized Gaussian beam at the output of the q-plate when $\delta = 2\pi$; (b) $\delta = 3\pi/2$ shows an example of q-plate tuning condition leading to the generation of a generalized vector beam with an asymmetric spatial distribution of the SoP. (c) $\delta = \pi$ corresponds to the q-plate tuning condition leading to the generation of optical vortex beams. The arrows schematically indicate the SoP input and output beams at the q-plate. The lower images show examples of the spatial intensity profiles of the converted beams.

2.6 Generation of asymmetric beams with the q-plate

The q-plate tuning is achieved by varying the optical retardation δ by means of the driving voltage V_{pp} (peak to peak) applied to the q-plate by using a square-wave at 11 kHz delivered by a signal generator [8], [29]. At the optimal tuning, corresponding to a half-wave retardation ($\delta = \pi$), the q-plate allows generating OV beams carrying an OAM $m = \pm 1$ through STOC of the angular momentum of light. An example of OV beam with a radial SoP is shown in the panel (c) of Fig. 2.6. A full wave retardation ($\delta = 2\pi$) results in a Gaussian beam at the q-plate output, as

illustrated in the panel (a) of Fig. 2.6). The fluence profile of the un-tuned case ($\delta = 2\pi$) corresponding to a Gaussian beam is illustrated in Fig. 2.4(c). The OV beams generated in the tuned case ($\delta = \pi$) are characterized by an annular spatial profile with a central region of null fluence due to an undefined phase on the OV beam axis, as described by Eq. (1) and illustrated in Figs. 2.4(d) and 2.6(c).

Partial tuning of the q-plate allows generating light beams, here indicated as fs generalized vector beams, for which only a partial conversion to an OV state is achieved [30]. Therefore, these beams can be described as a superposition of an OV and a Gaussian beam with a variable fraction of these two components. When focused with a low numeric aperture (NA) lens, as in our experimental conditions, these two components become spatially shifted in the focal plane. This, in turn, allows generating lopsided, fs laser beams with a rather complex spatial variation of the SoP and fluence distribution. An example of such a configuration is schematically reported in the Fig. 2.6 (b). Detailed explanations regarding the lopsided annular beams produced in the focal plane of the focusing lens and the corresponding asymmetric surface patterns generated will be reported in chapter 5.

2.7 Surface characterization techniques

Usually the characterization of surface is based on images obtained by scanning electron microscope (SEM). This provides good contrast images of the surface structure with high resolution. In our case an initial characterization to measure the quality and area of the ablation spot is done with optical microscope in order to get an approximate value of ablation threshold of the material. To get more information about the morphology of the formed structures, the irradiated surface is analyzed by using a Field Emission Scanning Electron Microscope (FESEM, *Zeiss SIGMA*). SEM images are acquired by registering secondary electrons (SE) with an Everhart-Thornley (ET-SE) type detector. From this SEM images measurements such as spatial period of ripples and grooves, ablation threshold, etc. are obtained. In some cases, an In-Lens (IL) detector, located inside the electron column of the microscope and arranged rotationally symmetric around the optic axis, is used to register SEM images with higher contrast.

References

- [1] A. Y. Vorobyev and C. Guo, “Direct femtosecond laser surface nano/microstructuring and its applications,” *Laser Photon. Rev.*, vol. 7, no. 3, pp. 385–407, May 2013.
- [2] C. Momma, S. Nolte, B. N. Chichkov, F. v. Alvensleben, and A. Tünnermann, “Precise laser ablation with ultrashort pulses,” *Appl. Surf. Sci.*, vol. 109, pp. 15–19, 1997.
- [3] L. Marrucci, C. Manzo, and D. Paparo, “Pancharatnam-Berry phase optical elements for wave front shaping in the visible domain: Switchable helical mode generation,” *Appl. Phys. Lett.*, vol. 88, no. 22, p. 221102, May 2006.
- [4] J. JJ Nivas, F. Cardano, Z. Song, A. Rubano, R. Fittipaldi, A. Vecchione, D. Paparo, L. Marrucci, R. Bruzzese, and S. Amoruso, “Surface Structuring with Polarization-Singular Femtosecond Laser Beams Generated by a q-plate,” *Sci. Rep.*, vol. 7, p. 42142, Feb. 2017.
- [5] J. J. J. Nivas, Z. Song, R. Fittipaldi, A. Vecchione, R. Bruzzese, and S. Amoruso, “Direct ultrashort laser surface structuring of silicon in air and vacuum at 1055nm,” *Appl. Surf. Sci.*, 2017.
- [6] L. Allen, M. W. Beijersbergen, R. J. C. Spreeuw, and J. P. Woerdman, “Orbital angular momentum of light and the transformation of Laguerre-Gaussian laser modes,” *Phys. Rev. A*, vol. 45, no. 11, pp. 8185–8189, Jun. 1992.
- [7] L. Marrucci, C. Manzo, and D. Paparo, “Optical spin-to-orbital angular momentum conversion in inhomogeneous anisotropic media,” *Phys. Rev. Lett.*, vol. 96, no. 16, p. 163905, 2006.
- [8] S. Slussarenko, A. Murauski, T. Du, V. Chigrinov, L. Marrucci, and E. Santamato, “Tunable liquid crystal q-plates with arbitrary topological charge,” *Opt. Express*, vol. 19, no. 5, p. 4085, Feb. 2011.
- [9] M. Padgett, J. Courtial, and L. Allen, “Light’s Orbital Angular Momentum,” *Phys. Today*, vol. 57, no. 5, pp. 35–40, May 2004.
- [10] M. W. Beijersbergen, R. P. C. Coerwinkel, M. Kristensen, and J. P. Woerdman, “Helical-wavefront laser beams produced with a spiral phaseplate,” *Opt. Commun.*, vol. 112, no. 5, pp. 321–327, 1994.
- [11] V. Y. Bazhenov, M. S. Soskin, and M. V. Vasnetsov, “Screw Dislocations in Light Wavefronts,” *J. Mod. Opt.*, vol. 39, no. 5, pp. 985–990, May 1992.
- [12] A. Mair, A. Vaziri, G. Weihs, and A. Zeilinger, “Entanglement of the orbital angular momentum states of photons,” *Nature*, vol. 412, no. 6844, pp. 313–316, Jul. 2001.
- [13] Y. Igasaki, F. Li, N. Yoshida, H. Toyoda, T. Inoue, N. Mukohzaka, Y. Kobayashi, and T. Hara, “High Efficiency Electrically-Addressable Phase-Only Spatial Light Modulator,” *Opt. Rev.*, vol. 6, no. 4, pp. 339–344, Jul. 1999.
- [14] L. Marrucci, “The q-plate and its future,” *J. Nanophotonics*, vol. 7, no. 1, p. 78598, Sep. 2013.
- [15] D. Puerto, M. Garcia-Lechuga, J. Hernandez-Rueda, A. Garcia-Leis, S. Sanchez-Cortes, J. Solis, and J. Siegel, “Femtosecond laser-controlled self-assembly of amorphous-crystalline nanogratings in silicon,” *Nanotechnology*, vol. 27, no. 26, p. 265602, Jul. 2016.
- [16] J. Bonse, S. Baudach, J. Krüger, W. Kautek, and M. Lenzner, “Femtosecond laser ablation of silicon - modification thresholds and morphology,” *Appl. Phys. A*, vol. 74, no. 1, pp. 19–25, 2002.

- [17] G. D. Tsibidis, C. Fotakis, and E. Stratakis, “From ripples to spikes: A hydrodynamical mechanism to interpret femtosecond laser-induced self-assembled structures,” *Phys. Rev. B - Condens. Matter Mater. Phys.*, vol. 92, no. 4, p. 41405, 2015.
- [18] S. He, J. JJ Nivas, A. Vecchione, M. Hu, and S. Amoruso, “On the generation of grooves on crystalline silicon irradiated by femtosecond laser pulses,” *Opt. Express*, vol. 24, no. 4, pp. 3238–3247, Feb. 2016.
- [19] O. Varlamova, M. Bounhalli, and J. Reif, “Influence of irradiation dose on laser-induced surface nanostructures on silicon,” *Appl. Surf. Sci.*, vol. 278, pp. 62–66, 2013.
- [20] G. Daminelli, J. Krüger, and W. Kautek, “Femtosecond laser interaction with silicon under water confinement,” *Thin Solid Films*, vol. 467, no. 1, pp. 334–341, 2004.
- [21] C. Hnatovsky, V. G. Shvedov, N. Shostka, A. V. Rode, and W. Krolikowski, “Polarization-dependent ablation of silicon using tightly focused femtosecond laser vortex pulses,” *Opt. Lett.*, vol. 37, no. 2, p. 226, Jan. 2012.
- [22] G. D. Tsibidis, M. Barberoglou, P. A. Loukakos, E. Stratakis, and C. Fotakis, “Dynamics of ripple formation on silicon surfaces by ultrashort laser pulses in subablation conditions,” *Phys. Rev. B*, vol. 86, no. 11, p. 115316, 2012.
- [23] Y. Han and S. Qu, “The ripples and nanoparticles on silicon irradiated by femtosecond laser,” *Chem. Phys. Lett.*, vol. 495, no. 4, pp. 241–244, 2010.
- [24] T. J.-Y. Derrien, T. E. Itina, R. Torres, T. Sarnet, and M. Sentis, “Possible surface plasmon polariton excitation under femtosecond laser irradiation of silicon,” *J. Appl. Phys.*, vol. 114, no. 8, p. 83104, 2013.
- [25] J. JJ Nivas, S. He, A. Rubano, A. Vecchione, D. Paparo, L. Marrucci, R. Bruzzese, and S. Amoruso, “Direct Femtosecond Laser Surface Structuring with Optical Vortex Beams Generated by a q-plate,” *Sci. Rep.*, vol. 5, p. 17929, Dec. 2015.
- [26] A. Y. Vorobyev and C. Guo, “Direct creation of black silicon using femtosecond laser pulses,” *Appl. Surf. Sci.*, vol. 257, no. 16, pp. 7291–7294, 2011.
- [27] J. Bonse, A. Rosenfeld, and J. Krüger, “Implications of transient changes of optical and surface properties of solids during femtosecond laser pulse irradiation to the formation of laser-induced periodic surface structures,” *Appl. Surf. Sci.*, vol. 257, no. 12, pp. 5420–5423, 2011.
- [28] M. J. Liu, “Simple technique for measurements of pulsed Gaussian-beam spot sizes,” *Opt. Lett.*, vol. 7, no. 5, pp. 196–198, 1982.
- [29] V. D’Ambrosio, F. Baccari, S. Slussarenko, L. Marrucci, and F. Sciarrino, “Arbitrary, direct and deterministic manipulation of vector beams via electrically-tuned q-plates,” *Sci. Rep.*, vol. 5, p. 7840, Jan. 2015.
- [30] A. D’Errico, M. Maffei, B. Piccirillo, C. de Lisio, F. Cardano, and L. Marrucci, “Topological features of vector vortex beams perturbed with uniformly polarized light,” *Sci. Rep.*, vol. 7, p. 40195, Jan. 2017.

Surface structuring with a femtosecond Gaussian beam

“This chapter illustrates experimental results on the various surface structures generated on crystalline silicon (100) by irradiation with fs laser pulses having a Gaussian intensity profile. In particular, characteristic effects of number of pulses and energy as well as bending and bifurcation phenomena of quasi-periodic structures will be presented. These aspects are, then, rationalized in the frame of a model of surface structure formation based on surface scattered wave theory. Finally, results of some experiments on the effect of the ambient gas pressure on the surface structures are illustrated.”

3.1 Introduction

The applicative interests of laser surface structuring are immense and these include the ability to permanently modify the surface absorption spectrum or change appearing colors of metals and semiconductors without any addition of pigments, the possibility to fabricate super-hydrophobic and self-cleaning surfaces, etc.[1]. Moreover, fs laser provides a versatile tool for micro- and nano-fabrication, such as periodic surface structures with a periodicity much less than the wavelength, microfluidic channels for biological uses and optical integrated circuits for quantum applications.

Laser parameters, like energy, pulse width, number of pulses, etc., have different effects in the generation of different surface morphologies. The spatial distribution of the beam intensity decides the shape of the ablated spot area inside which several kinds of surface structures can be formed, depending on the irradiation conditions. The nature of the morphological features formed on the irradiated surface showcases various features of both ultrafast laser pulses and target material. The nano/microscale surface structures produced by direct fs laser processing can be classified into the following categories [2]:

- nanoscale periodic/quasi-periodic structures;
- quasi-periodic, micron sized structures mostly decorated with nanostructures;

- irregular surface structures (nanocavities, nanospheres, nanoprotusions, nanowires)

Typically, structures presenting a regular pattern are denoted as LIPSS. In the case of semiconductor materials that show strong absorption at the laser wavelength, such as silicon, typically LIPSS are observed with a preferential orientation perpendicular to the laser beam polarization and with a spatial period Λ approximately in the range of the wavelength λ of the incident laser pulse ($\lambda/2 < \Lambda < \lambda$). These are known as low-spatial-frequency LIPSS (LSFL) or generally as “ripples”. Besides ripples, in some rare cases a very fine structure with spatial period of less than half of the laser wavelength ($\Lambda < \lambda/2$) are observed and these are categorized as high-spatial-frequency LIPSS (HSFL). In order to avoid any confusion, we would like to specify that in this thesis the term “ripples” always denotes the subwavelength structure LSFL, and HSFL is referred as “high frequency ripples”.

This chapter illustrates experimental results on the surface structures generated on crystalline silicon (100) targets by irradiation with fs laser pulses having Gaussian spatial intensity distribution. In particular, some signatures of the morphological features of ripples, like bending and bifurcation of quasi-periodic structures [3], along with some characteristic effects of surface structures on pulse energy and pulse number N , are discussed. General characteristics of the surface structures and their dependence on laser pulse number and energy are discussed in sections 3.2 and 3.3. Then, surface scattered wave theory is presented in section 3.4 and correlated with the experimental results to explain the various features generated at different irradiation conditions. Finally, section 3.5 addresses, how the ambient pressure influences the formation of different surface features. It is interesting to note that experiments done at reduced ambient pressure evidence a striking influence on the shape and area of the modified region as well as the formation of surface features with characteristics different from that produced in ambient air, which was seldomly addressed earlier.

3.2 Laser induced periodic surface structures with femtosecond Gaussian beam

When a solid target is irradiated with multiple fs laser pulses in sub-ablation conditions (i.e. below the single pulse ablation threshold), several self-assembled surface structures are found to be generated by multiple pulses on the irradiation spot, whose morphology ranges from nanoripples to periodic microgrooves and quasi-periodic microspikes [4]. In particular, these structures are formed depending on the level of excitation of irradiated surface induced by the fs laser pulses. So

by appropriate tuning of the laser parameters, specific surface structures can be optimized. Fig. 3.1 displays a typical SEM image of an ablation crater generated on silicon by 100 laser pulses with single pulse peak fluence $F_p=1.1 \text{ J/cm}^2$, in air. The laser used is a Ti:Sapphire laser having a pulse width of 35 fs and a central wavelength of 800 nm. As shown in Fig. 3.1, the Gaussian distribution of beam spatial intensity profile generates several periodic structures at an increasing radial distance from the center, depending on the local laser fluence. In the ablation spot shown in Fig. 3.1(a), two principal quasi-period features are recognized: micro-wrinkles formed in the higher fluence part, covering the major portion of the ablation crater, and an annular disc near the crater edge, characterized by reduced local fluence, composed of relatively finer structures. A zoomed view of both morphologies is given in Figs. 3.1(b) and (c). The finer structures preferentially aligned normal to laser polarization with spatial period $(683\pm62) \text{ nm}$ and occupying a $\sim 10 \text{ }\mu\text{m}$ annulus are identified as subwavelength ‘ripples’. From the center up to a radial distance of $\sim 23 \text{ }\mu\text{m}$, the crater is covered by micron-sized quasi-periodic structures with a preferential alignment along the laser polarization and whose spatial period comes in the range of $(2.1\pm 0.3) \text{ }\mu\text{m}$. This larger quasi-periodic structures with a period $\Lambda > 2\lambda$, usually designated as “grooves”, also generally accompanies LIPSS formation [2], [3], [5], [6]. The annular interface region between ripples and grooves with a characteristic width of $\sim 4 \text{ }\mu\text{m}$ is occupied by rudiments of grooves. The results suggest a deterministic relationship between orientation and characteristic size of the surface structure and local polarization and fluence of the laser beam. Most of the studies regarding LIPSS mainly focused on subwavelength ripples [1], [7]–[9], while more detailed analyses of micro-wrinkles produced by fs Gaussian beams started only very recently [3], [4], [6]. In general, fs laser surface nano- and micro-structuring has become a versatile method to tailor material surface morphologies, which enhance diverse interesting physical properties. Since with fs laser pulses one can generate periodic surface structures in all kind of materials like metals, semiconductors and dielectrics, the possibilities are enormous.

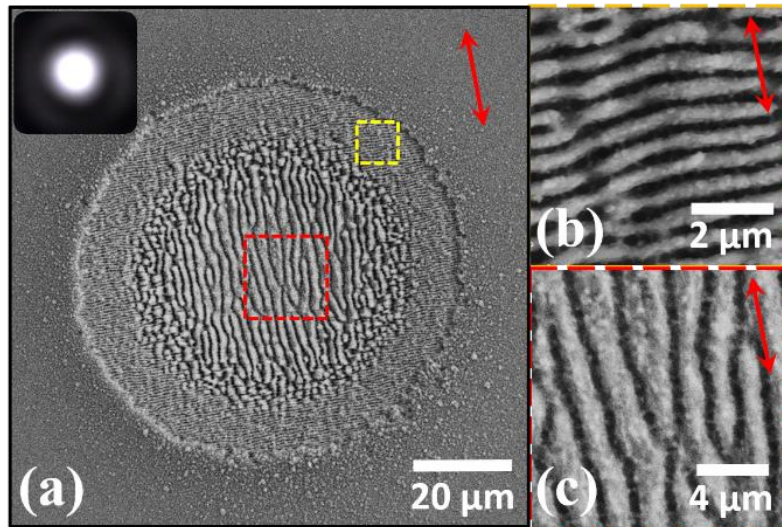


Figure 3.1/ Panel (a): Typical silicon surface after the irradiation with several fs laser pulse with Gaussian spatial intensity profile. The inset in panel (a) shows the CCD images of the Gaussian beam. Panel (b) & (c) show the zoomed views of the ripples aligned normal to the direction of laser polarization and micro-grooves formed along the polarization direction, respectively. The red arrow indicates the polarization direction.

There are numerous works investigating the origin mechanism and characteristic behavior of such formations with the various parameters like fluence, number of pulses per spot, irradiation wavelength, ambient condition, etc., by means of static experiments. The temporal evolution dynamics of ripples are investigated in many correlative approaches [10]. The formation of fs-LIPSS on silicon surfaces has already been studied in double-fs-pulse experiments with varying delay between double pulses, in the picosecond range, using Ti:sapphire laser at 800 nm wavelength [11][12][13]. The result of temporal dynamics study of ripples shows a characteristic decay of the rippled area as delay is increased, while the ripple period Λ remains almost constant.

Recently also the grooves, which usually form at higher fluence and larger number of incident laser pulses than ripples, gained more attention [4][14]. However, there is still a limited number of works dealing with detailed investigation of their properties. Contrary to ripples, grooves show a characteristic preferential alignment parallel to laser polarization and hence, orthogonal to ripples.

3.3 Characteristic formation of LIPSS in Silicon [100] crystal

Interaction of fs laser pulses with a silicon target surface clearly showcases the formation of quasi-periodic surface patterns with distinguishable characteristic features. Before each irradiation, the targets are well cleaned with ethanol to avoid any dust particle over the surface. Irradiation of crystalline silicon with fs laser pulses produces several quasi-periodic surface structures with individual period ranging from tens of nanometer to several microns. In our experiments, silicon is irradiated with fs pulses with Gaussian spatial intensity profile. In order to understand the complete formation sequence of different surface features, controlled ablation is done at various irradiation conditions. From the results it is found that, peak fluence (F_p) and total number of pulses (N) have great influence on the formation of different surface structures on silicon. In the upcoming section, first we will see the morphological features of the irradiated surface observed at different number of laser pulses, N , at a fixed fluence, F_p . We will first discuss the ripples characteristics by presenting experimental observations for N in the range 2–50, which is associated to the different excitation levels of the silicon under fs laser irradiation. This will address the initial formation of annular ripples (at low N) followed by a progressive surface development leading to the formation of quasi-periodic ripples (at larger N) characterized by some specific bending and bifurcation phenomena which are discussed later. The formation of grooves, for $N > 100$ are also discussed in association with model predictions. An effective fluence scaling is used by calculating the incubation factor to model the energy modulation over surface that corresponds to interaction with large number of consecutive laser pulses.

3.3.1 Evolution dynamics of different periodic structures

As a result of the interaction with a fs laser beam, numerous changes occur on the silicon surface after the incidence of each energetic pulse. In this section, we deal with the initial change in the surface morphology at early stage of structure formation. Fig. 3.2 shows SEM micrographs of the different surface structures on silicon after irradiation with different number of laser shots. In particular, $N = 2, 20,$ and 50 were considered to illustrate the morphological evolution of the surface structures leading to a rippled pattern at increasing exposure level.

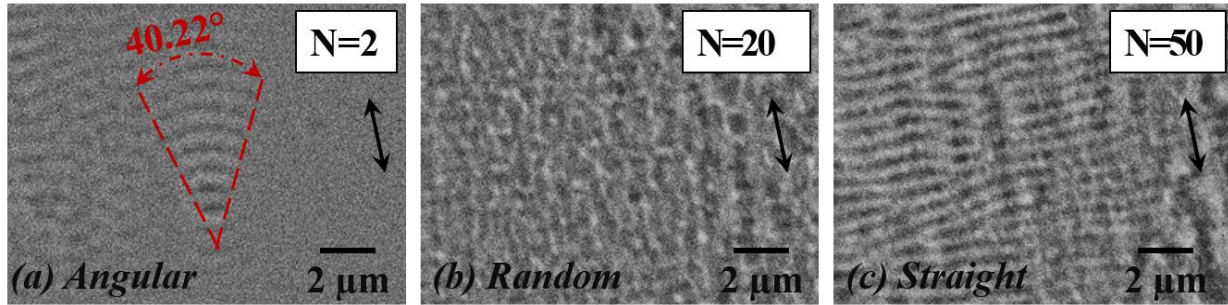


Figure 3.2/ SEM micrographs of the different surface structures formed after irradiation of Gaussian beam having a peak fluence $F_p=0.6 \text{ J/cm}^2$ after (a) $N = 2$, (b) $N = 20$ and (c) $N = 50$ laser pulses, illustrating the different morphologies of the rippled surface pattern. The black double-headed arrow indicates the direction of the incident laser pulse polarization.

In Fig. 3.2, the double-headed arrow indicates the direction of the laser pulse polarization. Fig. 3.2(a) ($N = 2$) refers to the very early stage of laser induced surface modification. It shows an “angular structure” in form of a periodic ensemble of curved ripples characterized by a sector angle of $\approx 40^\circ$. Similar wave-like curved localized patterns were reported earlier [15], and associated to a spatial modulation of absorbed energy induced by defects present on the silicon surface. At $N = 20$, the surface morphology transforms into a rather random pattern (see Fig. 3.2(b), e.g.) where only shallow and obscure rudiments of straight ripples are recognized. Then, Fig. 3.2(c) reports the target surface texture at $N = 50$, which is characterized by a quasi-periodic distribution of straight ripples orthogonal to the laser polarization with several interconnections, typical of LIPSS.

In semiconductors (Si and InP, e.g.), the ripples generation is followed by the progressive growth of grooves [3], [4], [14]–[18]. Grooves are formed at larger number of pulses (typically $N \geq 200$) and their spatial separation is always larger than 2λ . Fig. 3.3 reports SEM micrographs of the silicon surface after irradiation with $N = 200$ laser pulses, showing different regions of the spot along radial direction, at a peak fluence $F_p=0.6 \text{ J/cm}^2$. The central region of the irradiated spot presents an array of micro-grooves preferentially aligned along the laser polarization. The measured intervals between two consecutive groove stripes in Fig. 3.3(d) vary from $1.7 \mu\text{m}$ to $2.5 \mu\text{m}$. The outer area of the spot, instead, presents quasi-periodic ripples orthogonal to the laser polarization already discussed above (see Fig. 3.1). An intermediate region, showing rudiments of the grooves super-imposed over ripples, separates the inner and outer areas. This, in turn, again demonstrates that generation of the diverse morphologies depend on the local fluence value over

the irradiated surface, which is lower on the wings and more intense in the central area of the Gaussian beam.

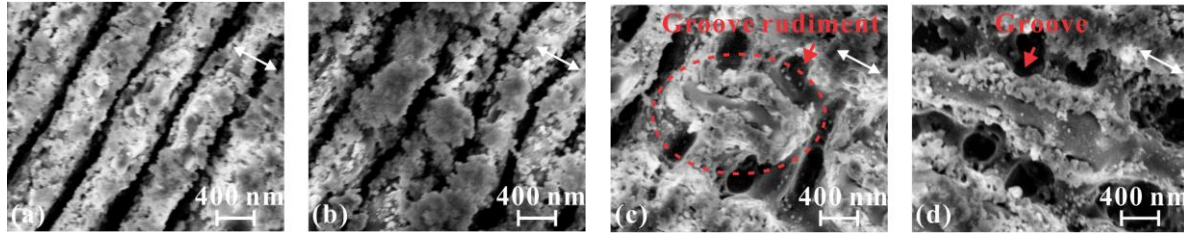


Figure. 3.3/ IL SEM micrographs formed after irradiation of Gaussian beam having a peak fluence $F_p=0.6 \text{ J/cm}^2$ after $N = 200$ illustrating the typical morphological features encountered by gradually moving from the rippled (a) to the grooved (d) areas through the intermediate region (panel (b) and (c)). The dashed ellipse in panel (c) evidences a rudiment of a groove directed along the laser polarization and covering the underlying ripples. The white double-headed arrow indicates the direction of the incident laser polarization.

We discuss now how the surface texture encountered in the passage from the rippled outer area to the grooved central area provides useful indications about the formation of grooves. Fig. 3.3 reports examples of SEM micrographs illustrating the morphological changes occurring when progressively moving from ripples (Fig. 3.3(a)) to grooves (Fig. 3.3 (d)), through the intermediate region represented in Fig. 3.3 (b) and (c). The SEM micrographs of Fig. 3.3 were registered by using the IL detector, which provides more defined surface information than the standard ET-SE detector. Fig. 3.3(a) shows an extended nano-roughness of the ripples surface, which is densely covered by nanoparticles or aggregates of nanoparticles, as typically observed in fs laser generated LIPSS [1]. Fig. 3.3(d) illustrates the detailed morphology of the grooves formed by stripes that are aligned along the laser polarization that cover the underlying ripples. These stripes present a smoother internal surface surrounded by aggregates of nanoparticles along the two sides. Moving from ripples to grooves, in the intermediate region one can observe the presence of large clusters of nanoparticles.

3.3.2 General characterization of ripples and grooves

Fig. 3.4 summarizes the dependence of both the width of regions presenting ripples and grooves (W_R and W_G) and of their spatial period (Λ_R and Λ_G) on laser pulse peak fluence F_p and number of pulses N . The error bars indicate the uncertainty estimated by considering the variability in the recognition of width and period in the various parts of the spot obtained in repeated measurements. Let us consider first the variation of widths reported in panels (a) and (b) of Fig. 3.4. The width W_R of the annular rippled region exhibits a small reduction on the pulse peak fluence F_p , compared

with the larger variation of W_G , which shows a $\sim 60\%$ increase with respect to the initial value. In general, as F_p increases, the area covered with grooves increases accordingly as a consequence of the fact that the region of the beam with a fluence larger than the threshold value for grooves formation progressively extends over a larger area. Moreover, ripples remain confined in zones of the beam at lower fluence (between thresholds values for grooves formation and target ablation), thus leading to the observed weak dependence of the width of the rippled regions with F_p . As for the variation with the number of pulses N , panels (b) of Fig. 3.4 shows that W_G increases also with N , eventually tending to level off at high number of pulses. This condition typically corresponds to the progressive formation of a deeper ablation crater. W_R does not show any noticeable dependence on N for $N \leq 200$. At larger N this trend is, then, followed by a gradual increase of W_R with N , which can be associated to progressive reduction of the fluence threshold for ablation typical of an incubation behavior [15], [19] and the observed levelling off of the width of the grooved region.

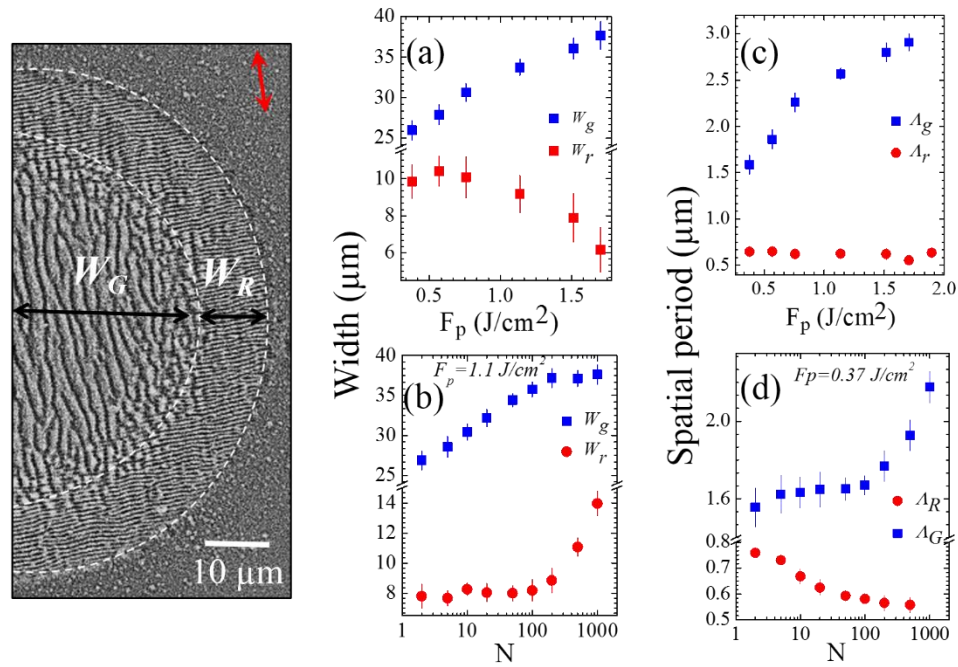


Figure 3.4| Variation of the width of the different structured surface regions recognized in the craters produced as a function of the laser pulse peak fluence, F_p , and laser pulse number, N . Left part: zoomed views of SEM images corresponding to a portion of the crater generated by a Gaussian beam. W_R , W_G and A_R , A_G corresponds to the width and period of rippled and grooved regions, respectively.

Considering the period variation, we observe that the average ripple period, Λ_R , remains almost constant over a rather broad range of pulse energies but shows a noticeable dependence on N . This is because conditions of ripple formation are always met by certain range of fluence region near the beam edge. When F_p increases, the area with high local fluence also increases, thus shifting the annular strip of rippled region more outward without changing the period. As a result the grooved region increases consistently, as observed in the plot of W_R with F_p . Fig. 3.4(d) displays a progressive decreases of Λ_R for $10 < N < 100$, then reaching a stationary regime for larger N , which is reported as a general characteristics of the ripples formation process [2], [4], [15], [20], [21]. Interestingly, we observe that the reduction with N is then followed by a plateau, suggesting a progressive saturation at a large number of laser pulses. The reduction of Λ_R with N is associated to two coexisting mechanisms proposed by Huang et al. that are the field effect and the grating-assisted SPP coupling [2]. Field effect is related to the progressive confinement of the ripples to regions of the beam periphery characterized by a gradual lowering of the local fluence with N which further causes the reduction in the excited carrier's local density, N_e . This reduction in N_e can result in an increase of $Re(n)$ [22] and a consequent reduction of the ripple period according to the relation $\Lambda = \lambda_{las}/Re(n)$, where λ_{las} is the laser wavelength and $Re(n)$ is the effective refractive index of the excited target surface [1], [2], [4]. The grating-assisted SPP coupling considers the fact that, as N increases, the ripples becomes gradually deeper with a reduction of the SPP periodicity and a consequent decrease of Λ_R to satisfy the appropriate condition of optimal coupling [2]. The spatial period of grooves Λ_G shows an increasing dependence on F_p over the entire range and a steep increase with N for $N > 200$. Our experimental findings on the variation of Λ_G with N is in agreement with other recent experimental observations [4], addressing an approximately linear rise of the grooves period with N during irradiation of silicon with a Gaussian beam (≈ 470 fs, 800 nm) at an average laser fluence of 0.7 J/cm^2 . However, in this study the analysis was limited to $20 < N < 100$. As we have seen in Fig. 3.3, progressive aggregation of large clusters of nanoparticles has major role in the development of grooves over underlying ripples. In particular, the smooth central part of the grooves suggests that their formation mechanisms possibly involve melting and re-solidification of clusters of nanoparticles. Thus, an increase of the peak fluence F_p and number of pulses N can likely favor aggregation of rudimental grooves structures thus leading to the progressive rise of the average grooves period in either case.

3.3.3 Threshold of surface structure formation

Ablation occurs when the peak laser fluence is larger than the ablation threshold of the material. The properties of the ablation process are then related to the beam characteristics. For laser beams with a Gaussian spatial intensity profile, a well-established method, based on the analysis of the lateral dimensions of the ablation crater produced on the target [8], [23], allows determining important parameters such as beam waist, peak fluence of the laser pulse, as well as material related information like fluence threshold for ablation of the target material as well as threshold for the formation of specific surface structures. All mentioned parameters are fundamental for an accurate description of the experimental conditions and for a clear analysis of the investigated processes. Considering the Gaussian spatial beam profile with a $1/e^2$ -beam waist w_0 , the peak fluence is $F_p=(2E_0)/(\pi w_0^2)$ and the squared outer radius r_k of the two patterned regions ($k=R$ and G for ripples and grooves, respectively) is related to the corresponding energy threshold $E_{th,k}$ by:

$$r_k^2 = \frac{1}{2} w_0^2 \ln \left(\frac{E_0}{E_{th,k}} \right) = \frac{1}{2} w_0^2 \ln \left(\frac{F_p}{F_{th,k}} \right) \quad (1)$$

where $E_{th,k}$ and $F_{th,k}$ are the threshold energy and fluence for ripples ($k=R$) and grooves ($k=G$), respectively, and $F_{th,k}=(2 E_{th,k})/(\pi w_0^2)$. Fig. 3.5(a) reports r_R and r_G as a function of the laser peak fluence F_p , for a fixed irradiation sequence $N=100$, which are well described by Eq. (1). From fits we obtain $w_0=(34.2\pm 0.5) \mu\text{m}$ both from ripples and grooves, $E_{th,R}(N=100)=(1.22\pm 0.06) \mu\text{J}$ and $E_{th,G}(N=100)=(4.72\pm 0.06) \mu\text{J}$. Consequently, the threshold fluences are $F_{th,R}(N=100)=(66\pm 5) \text{mJ/cm}^2$ and $F_{th,G}(N=100)=(260\pm 20) \text{mJ/cm}^2$. It is found that, the fluence threshold $F_{th,k}$ for ripples and grooves formation varies with the number of pulses N . This is referred to as incubation effect, which is known to reduce the multiple-pulse ablation threshold as the number of pulses increases as a consequence of defect creation and related feedback effects for laser-induced surface modification [7], [8]. As the surface texture depends on the local beam fluence, the variation of $F_{th,k}$ with N is obtained by measuring the values of the radii $r_{k,in}$ and $r_{k,ex}$ of the two circles delimiting the grooved area formed after irradiation with different values of the pulse number N , and estimating the corresponding value of the fluence threshold $F_{th,k}$ from the spatial profile of the pulse fluence $F(r)$. The values of the fluence at the margin of the rippled and grooved regions correspond to the threshold fluences $F_{th,R}$ and $F_{th,G}$ for ripples and grooves formation, respectively, as illustrated in Fig. 3.1(a). Fig. 3.5(b) reports the variation of the threshold fluences with N in the form $N \times F_{th,k}(N)$ vs N , for $F_p=1.5 \text{ J/cm}^2$. The experimental data are well described by a linear

dependence on a semi-logarithmic plot, supporting a power law dependence of the threshold fluence typical of an incubation behavior [8]:

$$F_{th,k}(N) = F_{th,k}(1)N^{\xi_k-1} \quad (2)$$

where $F_{th,k}(1)$ is the threshold fluence for $N=1$ and ξ_k is the incubation factor, with $k=R$ for ripples and $k=G$ for grooves, respectively.

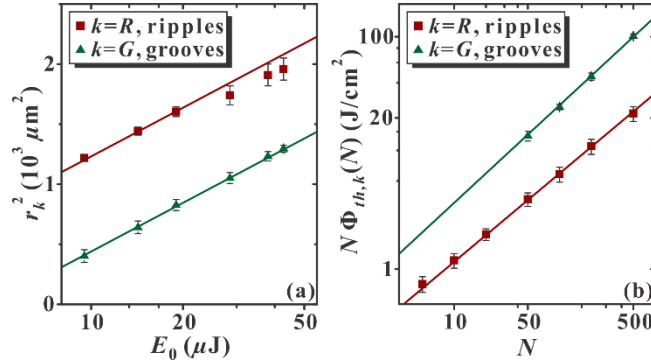


Figure 3.5/ (a) Variation of r_R and r_G with pulse energy E_0 . (b) Threshold fluence variation with the number of pulses N in the form $N\Phi_{th,k}(N)$ vs N ($k=R$ for ripples and $k=G$ and grooves). The lines in (a) and (b) are fits according to Eqs. (1) and (2), respectively.

Considering first ripples, fit to experimental data gives $F_{th,R}(1)=(0.20\pm 0.04)$ J/cm^2 and $\xi_R=(0.76\pm 0.04)$ (see Fig. 3.5(b), square symbols). As for the grooves, we notice that for N lower than ≈ 50 only isolated groove rudiments are observed, which is not considered in the measurement, at $F_p=1.5$ J/cm^2 . Moreover, the value of the number of pulses at which well-developed grooves start appearing varies with laser pulse peak fluence indicating that a minimum pulse number is needed for grooves formation, in agreement with earlier reports [8], [24]. Therefore, in Fig. 3.5(b) the values of $F_{th,G}$ starts at $N=50$. Interestingly, when a groove pattern starts forming $F_{th,G}(N)$ also follows Eq. (2), with $F_{th,G}(1)=(0.54\pm 0.08)$ J/cm^2 and $\xi_G=(0.84\pm 0.03)$. In our studies, these incubation behavior has been applied to rationalize the variation of the threshold fluence needed to induce modification or ablation of the target surface. We have expanded it to describe the dependence of the ripples and grooves formation threshold on N . Our experimental findings strikingly indicate that it also describes rather well the dependence on N of the threshold fluence for the formation of both ripples and grooves. Moreover, the estimates of the incubation coefficient are consistent with the value $\xi\approx 0.84$ reported by Bonse et al. for the modification threshold of silicon [8], minor differences being expected to depend on specific experimental conditions, e.g. wavelength and duration of laser pulses, and repetition rate. Incubation behavior has been reported

earlier for laser induced damage and ripples formation of different materials, but it was never associated to the generation of specific surface structures formation. The existence of an incubation effect for ripples and grooves formation suggests that the dynamic evolution of the target surface during multi-pulse exposure to laser pulses is also a key factor for the creation of these surface structures.

SEM images of the surface (Fig. 3.2 and Fig. 3.3) and also earlier works [14], [15] demonstrate that a multi-pulse feedback mechanism occurs in fs surface structuring leading to ripples and grooves formation [15], [16], [25]. This further indicates influence of the mechanisms leading to the incubation phenomenon discussed above on the features of the generated surface pattern. As the number of pulses N increases, the incubation effect progressively reduces the threshold fluence for LIPSS formation, thus suggesting that a varying level of effective excitation is associated with the cumulative effect of pulse number N . We propose to introduce such an effect by considering an effective fluence F_{eff} rescaled with respect to the experimental single-shot threshold fluence for surface structure formation $F_{th,k}(1)$ in the same proportion as the actual local fluence F scales with the threshold fluence for N pulses $F_{th,k}(N)$. The scaling can be denoted as,

$$F_{eff} = N^{1-\xi_k} \times F \quad (3)$$

The scaling shown in Eq. (3) can be associated to an effective value of the local fluence to any position along the beam radius in multiple shot experiments.

3.4 Mechanism of LIPSS formation

The surface scattered wave model by Sipe *et al.* [26] represents the first principle theory describing the mechanism of laser induced periodic surface feature formation, taking into consideration the interaction of electromagnetic wave with a microscopically rough surface. The Sipe-Drude model is an extension of the surface-scattered wave theory by considering the effects of the carrier-dependent variation of the dielectric permittivity ϵ of the target surface induced by fs laser pulse irradiation [27]. This model essentially provides the possible aspect of the electromagnetic energy modulation on the surface which is eventually responsible for the morphological change occurred in the irradiated surface. This also includes the possibility of excitation of coupled state of surface electron oscillation and light called surface plasmon polaritons.

3.4.1 Surface scattered wave model

The fundamental idea of surface-scattered wave theory came from the pioneering work of Emmony *et al.* [28]. This theory was later developed and formulated by Sipe *et al.* in 1983[26]. According to the theory, the modulation of energy over the laser irradiated surface has been attributed to the interference of the incident beam with a "surface-scattered wave" originating from the pre-existing surface defects. This results in an inhomogeneous energy deposition over the irradiated surface and eventually leads to ripples formation by modification of surface over periodic locations. With the aid of model predictions a scalar factor called efficacy factor η is calculated at different levels of material excitation, which suggests a possible mechanism of subwavelength ripples and micro-grooves formation.

The theoretical interpretation of the surface structure formation is based on an extension of surface-scattered wave theory of Sipe *et al.* which takes into account the effects of the variation of the dielectric permittivity ϵ of the silicon target surface induced by laser pulse irradiation. This approach allows to numerically calculate a spatial pattern of energy deposition on a rough target surface, and the formation of periodic surface structures is rationalized in terms of the spatial modulation induced by the interaction of the incoming radiation and the scattered surface wave. The carrier dependent inhomogeneous energy absorption pattern over the silicon surface can be simulated by combining two-temperature model, free-carrier dynamics and Sipe theory [26], for different values of the laser pulse fluence. Detailed information on the model is provided in Appendix 1.

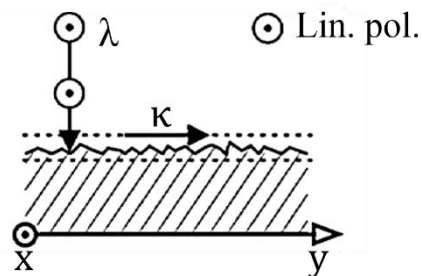


Figure 3.6 | Sketch showing the geometry of the rough surface irradiated with linear polarized light at wavelength λ and the surface wave vector κ [26].

Fig. 3.6 displays the basic interaction geometry of polarized laser beam in normal incidence with material surface with a wave vector of the surface roughness k , over the irradiated target surface (where $|k| = 2\pi/\Lambda$, where Λ is the spatial period of the surface roughness). While interaction occurs between laser pulse and target surface, the local free-carrier number density $N_e(r = 0)$ at the center of the laser focus progressively increases achieving its maximum value at a certain time t^* . At t^* , the real part of the dielectric permittivity ϵ reaches its minimum, and we indicate this value as ϵ^* . Fig. 3.7 (a) & (b) reports the variation of the real and imaginary part of ϵ^* as a function of peak fluence F_0 , for different values of the pulse duration τ_p . A significant dependence of ϵ^* on fluence and laser pulse duration is observed.

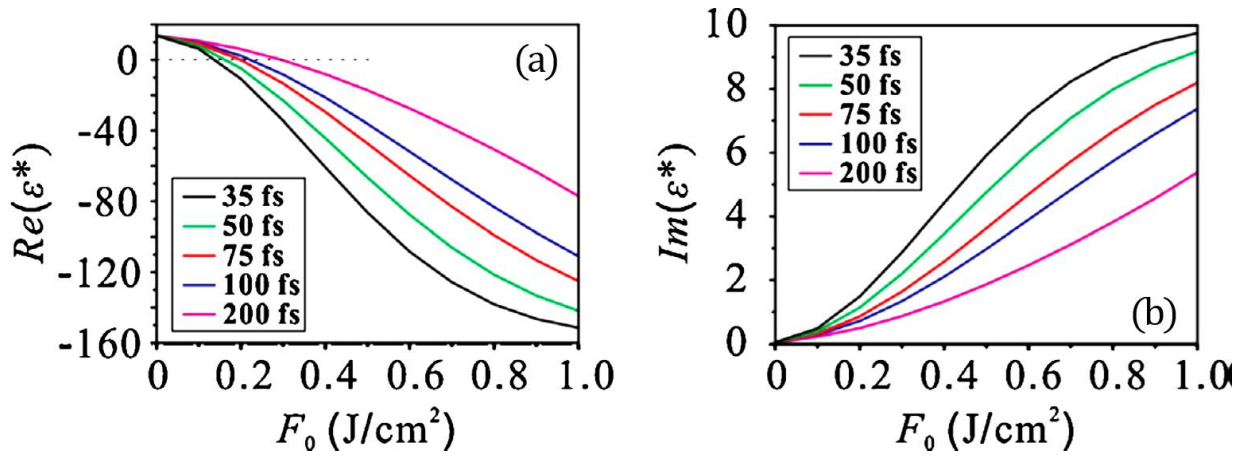


Figure 3.7/ Panel (a) and (b) report the variation of the real (a) and imaginary (b) part of the dielectric permittivity ϵ^* , as a function of the peak fluence F_0 , for various values of the pulse duration. The dashed line in the left panel marks the transition to a negative value of $Re(\epsilon^*)$.

It is worth noticing that the LIPSS theory used here to calculate the efficacy factor $\eta(k)$ does not take into account multi-pulse irradiation and the corresponding feedback influence, which is very difficult to simulate numerically. Therefore, single pulse irradiation is generally simulated and compared with experimental observations [26], [29]. In our case, we assume that a single 35 fs, linear polarized, laser pulse hits a silicon surface, with a surface roughness defined by the classical parameters $s = 0.4$ and $f = 0.1$ [16] depicted as spherically shaped islands, at normal incidence. However, from the experimental point of view it is hard to produce clear surface ripple structures with number of laser pulses lower than ten, or to adjust the laser pulse energy so precisely to follow in a single shot the transition from ripples to grooves formation. Therefore, we carried out

experiments at fixed laser pulse fluence and varied the number of laser pulses N . In this case, a clear evolution of the surface patterns showing both ripples and grooves is obtained. The modification threshold follows the incubation relation as mentioned earlier. Therefore, one can rationalize the experimental dependence on laser pulse number as an effective increase of the absorbed laser pulse fluence. Moreover, simulations at different laser fluences allow interpreting the characteristics of the surface structures produced at different levels of excitation, depending on the number of laser pulses N , used to irradiate the target surface.

One unique property of well-formed ripples is the presence of many bending and dividing/bifurcation features in their arrangement over the spot. We strongly believe these are not arbitrary effects but come from congenital properties of the generation mechanism. 2D inverse Fourier transform (2D-IFT) maps of η are predicted addressing the ripples properties and their spatial arrangement. In the next two sub-sections, we address how 2D-IFT of η maps predicted by Sipe-Drude model can allow shedding light on both the generation of ripples and their spatial arrangement and the formation of grooves in relation with the excitation level of the irradiated surface. The IFT is performed with Origin software (*OriginLab Corp.*) in order to obtain the real domain representation from calculated η map.

3.4.2 Formation and characteristic bending/bifurcation of ripples

Many experimental works on silicon clearly show that the single ripple line or strip is not always straight [15], [30], i.e. its orientation bends and is not always exactly perpendicular to the direction of the incident laser polarization. Therefore, ripples should be characterized as quasi-periodic surface structures. Fig. 3.8(a) & (d) illustrate SEM images of the ripples generated by irradiation with 800 nm, 35 fs laser pulses at $N=2$ and 100 respectively, depicting two main formation phases, the early stage and fully developed. In Fig. 3.8(d), three different typical morphologies, which are frequently occurring in all displayed ripple patterns, are indicated as I, II and III. Types I and II show the bifurcation of a ripple into two and three separated stripes (fork like structures), respectively. Type III depicts the bending of ripples. Fig. 3.8(g) reports schematic diagrams of the types I–III morphological features defining the bending angle formed by a vertex, at the position where the ripple bends or splits, and with the two sides provided by ripples making an obtuse angle. According to our experimental results for all the structures of the types I–III observed, the bending angle varies between 143° and 163° .

Figs. 3.8(b) and (e) report two examples of the efficacy factor $\eta(\kappa)$ as a function of the normalized LIPSS wave vectors components (κ_x, κ_y) , calculated for two different excitation levels of the material in conditions similar to those of Fig. 3.8(a) and (d) (namely, $F_p = 0.2 \text{ J/cm}^2$ and $F_p = 0.6 \text{ J/cm}^2$) in the form of a two-dimensional (2D) gray-scale intensity map. The direction of the incident laser polarization is parallel to the κ_y axis. The intensity scale on the right of the map indicates that darker points in the (κ_x, κ_y) plane correspond to larger values of energy absorption. In both cases, the darker areas are located in a very thin annular region with a radius of ≈ 1 from the center at $(\kappa_x, \kappa_y) = (0, 0)$, indicating that they represent the LIPSS wave vectors with higher absorption that eventually lead to ripple formation. We notice that $\eta = 0$ at the points $(\kappa_x, \kappa_y) = (0, \pm 1)$, which indicates the general feature that the inhomogeneous spatial distribution of absorbed energy eventually hinders the formation of LSFL directed along the laser pulse polarization. The 2D maps of Fig. 3.8(b) and (e) demonstrate a clear dependence on the excitation level of the characteristic features of the efficacy factor $\eta(\kappa)$. At $F_p = 0.2 \text{ J/cm}^2$, a rather distributed sets of values (κ_x, κ_y) confined in a sickle shaped feature can be recognized in the map of Fig. 3.8(b), meanwhile at $F_p = 0.6 \text{ J/cm}^2$ the map of Fig. 3.8(e) shows the appearance of very sharp peaks. In particular, two major features are identified, indicated as peaks P_A and P_B , respectively. These two peaks correspond to the highest (P_A) and the second highest (P_B) intensity values of $\eta(\kappa)$.

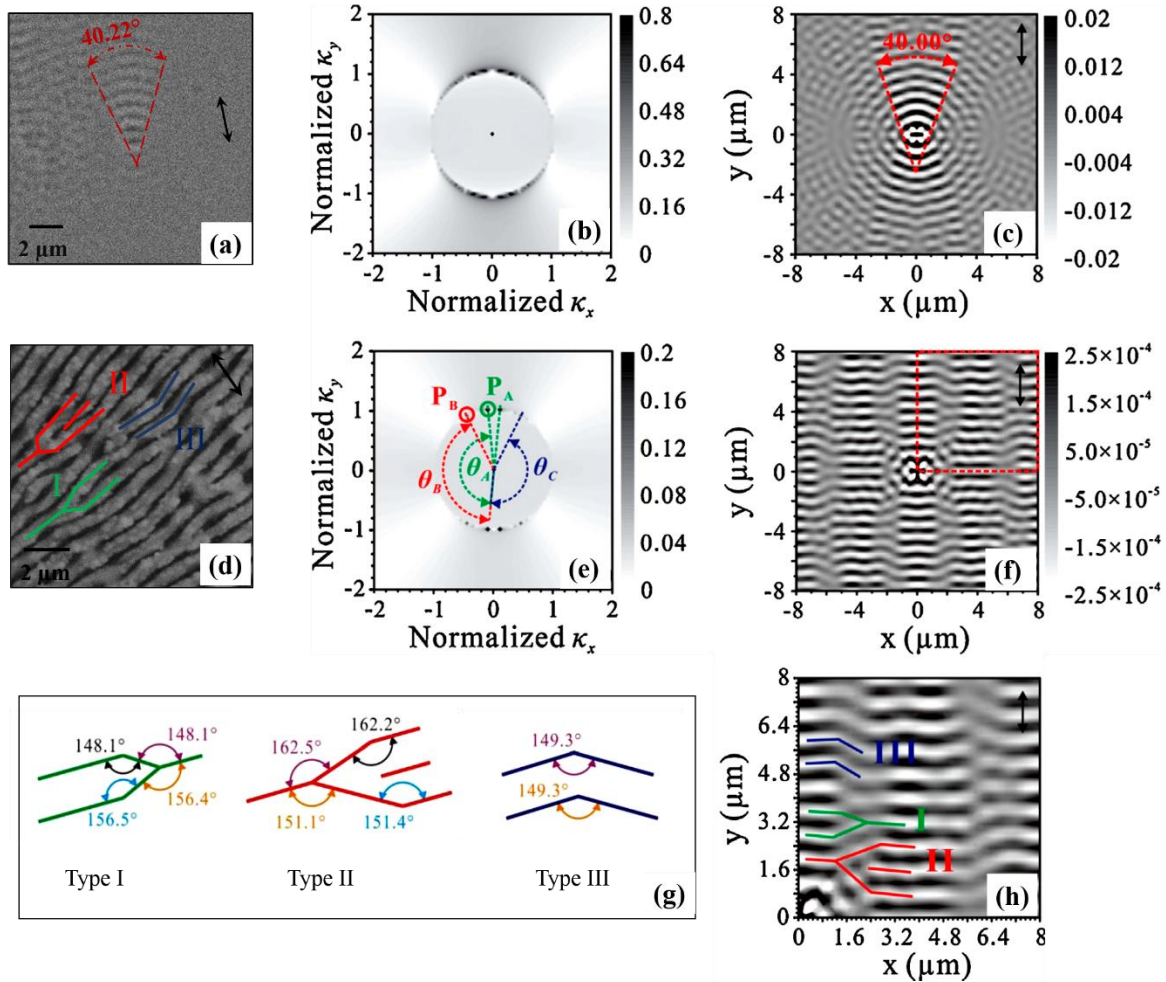


Figure 3.8/ Panels (a) and (d) report SEM images of silicon surface irradiated with fs laser pulses at $N=2$ and 100 which corresponds to an effective peak fluence $F_{p,eff} = 0.2 \text{ J/cm}^2$ and $F_p = 0.6 \text{ J/cm}^2$ respectively evaluated in reference to Eq. (3). Panels (b) and (e) are the representative 2D gray-scale intensity maps of the efficacy factor $\eta(\kappa)$ as a function of the normalized LIPSS wave vectors components (κ_x, κ_y) , calculated for similar excitation conditions mentioned for (a) and (d) respectively. The gray scale on the right of each map indicates that darker points in the (κ_x, κ_y) plane correspond to larger values of energy absorption. Panels (c) and (f) are the 2D-IFTs corresponding to the maps of panels (b) and (e), respectively, in the real scale coordinates (x, y) showing original wave-like curved ripple formation from local defects. Panel (h) shows a zoomed view of the dashed square area in red of the 2D map of panel (f). The gray scale on the right of each 2D-IFT map indicates the spatial modulation of the deposited energy, i.e. negative and positive values are associated to a reduction and an increase of the effective energy absorption with respect to that corresponding to the absence of the inhomogeneous redistribution driven by surface roughness. In panel (g) a schematic representation of the bending and bifurcation structures named Type I, II and III with the corresponding angle measured are shown. The black double-headed arrow indicates the direction of the incident laser polarization.

Since the distribution of η is central symmetric, there are four features with the same amplitude values of peaks P_A or P_B . The transition from a more dispersed region of high intensity to well-defined peaks indicates the progressive transition from less defined surface modifications to regular structures with ripples aligned along specific directions as the excitation level increases

[3]. This trend is similar to that observed experimentally as a function of the number of pulses N , as reported in Fig. 3.2. In Fig. 3.7(b), $F_p = 0.2 \text{ J/cm}^2$ corresponds to an excitation level of the irradiated surface at which $\text{Re}(\epsilon^*)$ becomes negative, and it can be associated to the initial state of the surface morphology modification at low N shown in Fig. 3.8(a). Therefore, the map of Fig. 3.8(b) should be representative of the localized angular structures observed at $N = 2$. Instead, $F_0 = 0.6 \text{ J/cm}^2$ can be considered representative of the situation for the formation of regular ripples illustrated in Fig. 3.8(e), for $N = 100$. Fig. 3.8(a) also reports the similar condition of well-defined ripples and the bending/bifurcation properties are displayed in the zoomed view as Fig. 3.8(b). The principal morphological features depend on the relative locations of the high intensity peaks, as P_A and P_B . Therefore, we measured the characteristics obtuse angles formed between the LIPSS wave vectors as indicated in the map of Fig. 3.8(e), obtaining $\theta_A = 169^\circ$ for the highest intensity features as P_A , and $\theta_B = 148^\circ$ and $\theta_C = 158^\circ$ for those involving both P_A and P_B . Interestingly, the values of θ_A , θ_B and θ_C are similar to those observed in Fig. 3.8(d) and schematically illustrated in Fig. 3.8(g). In order to provide a clear visualization of the corresponding energy modulation and a more direct comparison with experimental observations, we applied discrete 2D-IFT to convert 2D maps of $\eta(\kappa)$ from the (κ_x, κ_y) wave vector space to a 2D real spatial domain in the corresponding (x, y) coordinates. Panels (c) and (f) of Fig. 3.8 show the 2D-IFT maps of Fig. 3.8 (b) and (e), respectively, already rescaled into real scale coordinates. The gray scale on the right of each 2D-IFT map indicates the modulation of the deposited energy, i.e. negative and positive values are associated to a reduction and an increase of the effective energy absorption, respectively, with respect to that corresponding to the absence of the inhomogeneous redistribution driven by the surface roughness. The 2D-IFT map of Fig. 3.8(b) corresponding to $F_p = 0.2 \text{ J/cm}^2$ can be associated to the inhomogeneous energy distribution pattern occurring for a relatively flat target surface, possibly presenting a very low roughness with sparse and localized defect points. The scattered wave fields generated at a local defect are more intense than that corresponding to the relatively smoother region of the rest of the irradiated area. This, in turn, causes a localized inhomogeneous energy deposition only in a region adjacent to a defect point, giving rise to a wavelike, circular pattern as sketched in Fig. 3.8(c). It clearly exemplifies the formation of a wavelike, circular pattern of energy distribution which explains the formation of the angular structures reported in Fig. 3.8(a), for $N = 2$. In the map of Fig. 3.8(c) a sharp boundary confining a more pronounced pattern to an angular sector of $\approx 40^\circ$ can be identified. It is remarkable that this

is very similar to the characteristic feature observed experimentally for $N = 2$ shown in Fig. 3.8(a). The progressive formation of localized, rippled structures as N raises gradually increments the surface roughness, thus reducing surface reflectivity and ablation threshold and increasing the excitation level [1], [31]. The quasi-periodic pattern of the 2D-IFT map of Fig. 3.8(e) well represents the generation of ripples perpendicular to the laser polarization. Fig. 3.8(h) reports a zoomed view of the dashed square area indicated in red in Fig. 3.8(e) which shows the presence of finer modulations in the inhomogeneous distribution of the absorbed energy addressing the splitting and bending of ripples. Moreover, the different LIPSS structures recognized in Fig. 3.8(f) are consistent with the three types of characteristic morphological features indicated as I, II and III in Fig. 3.8(d). This, in turn, demonstrates that the various absorption peaks characterizing at high excitation level shown in Fig. 3.8(e) are responsible for bending and bifurcation of the generated ripples pattern. Hence, the structures of type I, II and III can be ascribed to the superposition of the LIPSS wavevectors peaking at P_A and P_B . Interestingly, the predicted bending angles are $(148^\circ \pm 5^\circ)$ and $(158^\circ \pm 5^\circ)$, thus consistent with the values observed in the experiment and schematically summarized in Fig. 3.8(g).

The good agreement between model predictions and experimental results discussed above leads to two important remarks. First, the model is able to retain the main physical features influencing ripples formation in silicon. Second, it singles out the possibility to describe the dependence of the surface structures on pulses number N observed in experiments, with a corresponding increase of the level of excitation, expressed in the model by a simple parameter, the input peak fluence F_p . Therefore, we carried out a more systematic analysis of the evolution of the 2D-IFT maps as a function of the peak fluence F_p , and the corresponding surface morphologies are summarized in Ref. [3].

3.4.3 Formation of Grooves

The comparatively larger LIPSS feature are formed after the irradiation of much higher N than that of ripples. Using the Sipe-Drude model to simulate higher excitation conditions related to an increased fluence F_p a progressive blurring of the nanoscale morphological features in 2D-IFT map is seen. In particular, one can observe a progressive formation of larger stripes with lower intensity overlapping the quasi-periodic ripple pattern observed at lower F_p values. These stripes, preferentially aligned along the laser polarization, tend to form another quasi-periodic pattern and

to wipe out the relatively straight structures, thus progressively restricting the ripple to a residual region of the surface. This phenomenon becomes more and more important as the excitation level increases. We believe that this feature can explain the progressive formation of grooves in the central region of the irradiated area (as in Fig. 3.1). Fig. 3.9 (a) reports the SEM image of the ablation crater where grooves are fully formed after the irradiation of 200 pulses with $E_0=10 \mu\text{J}$. This corresponds to a peak fluence $F_p \approx 0.8 \text{ J/cm}^2$. The marked region shows three main characteristics feature most commonly found in the grooves in silicon, which are marked as A, B and C in different colors.

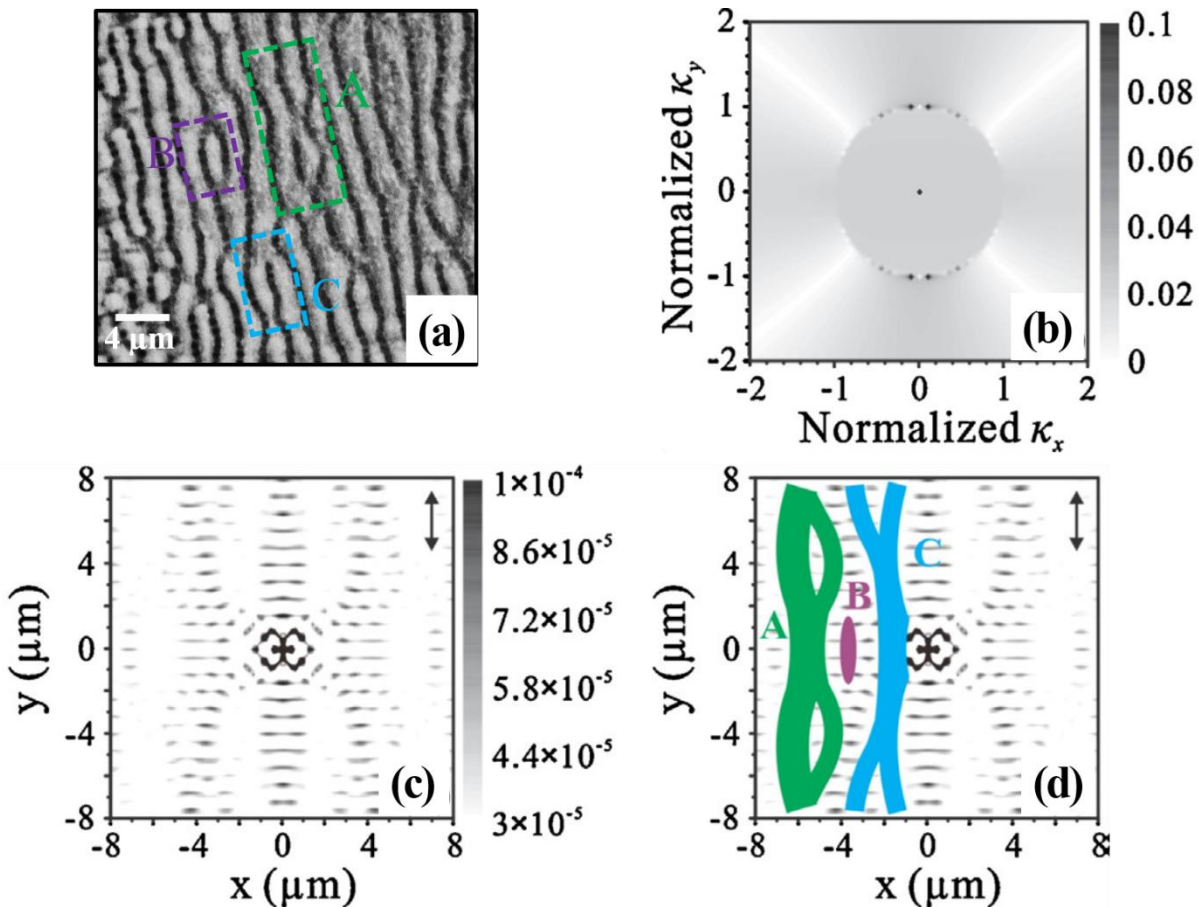


Figure 3.9| (a) SEM image showing central portion of the ablation crater where grooves are completely formed. (b) 2D gray-scale intensity map of the efficacy factor $\eta(\kappa)$ as a function of the normalized LIPSS wave vector components (κ_x, κ_y) , calculated for $F_p = 0.8 \text{ J/cm}^2$. (c) 2D-IFTs corresponding to the map of panel (b) in the real scale coordinates (x, y) . The intensity scale has been chosen to enhance the contrast between regions of lower (white) and higher (black) amplitude. (d) Sketch showing the morphological features identified on the 2D-IFT reflecting the groove pattern evidenced in the SEM micrograph of panel (a). The black double-headed arrow indicates the direction of the incident laser polarization.

Fig. 3.9(b) and (c) reports the 2D map of the efficacy factor $\eta(\kappa)$ and the corresponding 2D-IFT map for $F_p = 0.8 \text{ J/cm}^2$. The intensity scale in Fig. 3.9(c) has been chosen for better reading of different regions of high (black) and low (white) amplitude. In Fig. 3.9(c), one can observe the coexistence of two quasi-periodic patterns of the efficacy factor, one with a period of few μm occurs along the y-direction (along the laser polarization) which is superimposed over a sub-wavelength modulation depicting the ripples formation. The white stripes in Fig. 3.9(c) are characterized by amplitude ≈ 3 times lower than the maximum value (in black) with a negligible variation of intensity along white stripe. Fig. 3.9(d) depicts the possible morphologies of structures belonging to the white stripes evidenced in color, which resemble the three characteristic patterns A, B, C observed in the grooved area, as shown in Fig. 3.9(a). The measured spatial intervals between two white stripes of the grooves among pattern A, B and C also vary from $1.7 \mu\text{m}$ to $2.5 \mu\text{m}$, in agreement with experimental results. The close correspondence in the morphology either indicates the validity of possible explanation using Sipe-Drude model in predicting the formation mechanism. The quasi-periodic pattern of white stripes points to a spatial redistribution of the absorbed energy, and to the formation of regions where the absorbed fluence is not high enough to induce effective ablation, while being able to melt the surface nanostructures present in these regions, eventually leading to the progressive generation of the groove stripes covering the underlying ripples. In addition, the modulation of the energy in the gap between the white stripes observed in Fig. 3.9(c) suggests that the areas of maximum energy absorption in such a case are located close to the ripples, thus explaining the gradual increase of the separation distance between the ripples remnants under the fully generated grooves as observed in Fig. 3.3(d) due to more spatially selective ablation in these areas. This effect gives rise to formation of regularly arranged holes, in the order of ripples, in either side of each groove structures.

3.5 Effect of nanoparticle in surface structure formation

The experiments on surface structures formation that we have described so far are completely carried out in ambient air. One of the main characteristics of pulsed laser ablation is the generation of nanoparticles and the amount of nanoparticles are much more abundant for ablation with fs pulse. During the laser ablation with multiple shots, it can be found that surface morphology keeps on changing every time after it gets interaction with laser pulse, and a considerable part of the surface gets decorated with nanoparticles. These nanoparticles result from the significant

backward deposition of the abundant nanoparticulate fraction of ablated material produced during ultrashort laser ablation [32] that occurs at atmospheric pressure [1], [33], [34]. The result of our ablation experiments point out that a crucial role may be played by nanoparticles always decorating the surface structures for irradiation with ultrashort pulses in air [3], [14], [19]. Here we discuss about an experimental investigation of direct laser surface structuring of silicon with ≈ 900 fs laser at $\lambda=1055$ nm in atmospheric pressure, and in high vacuum conditions ($\sim 10^{-5}$ mbar). Structuring at high vacuum is selected to avoid any re-deposition of nanoparticles back on the surface and the comparison with the one done in air can help developing the idea about role and influence of nanoparticles in various surface structure formation. The morphological changes of the irradiated surface, in air and vacuum, could be helpful to provide interesting results and also further insights into the process of laser surface structuring.

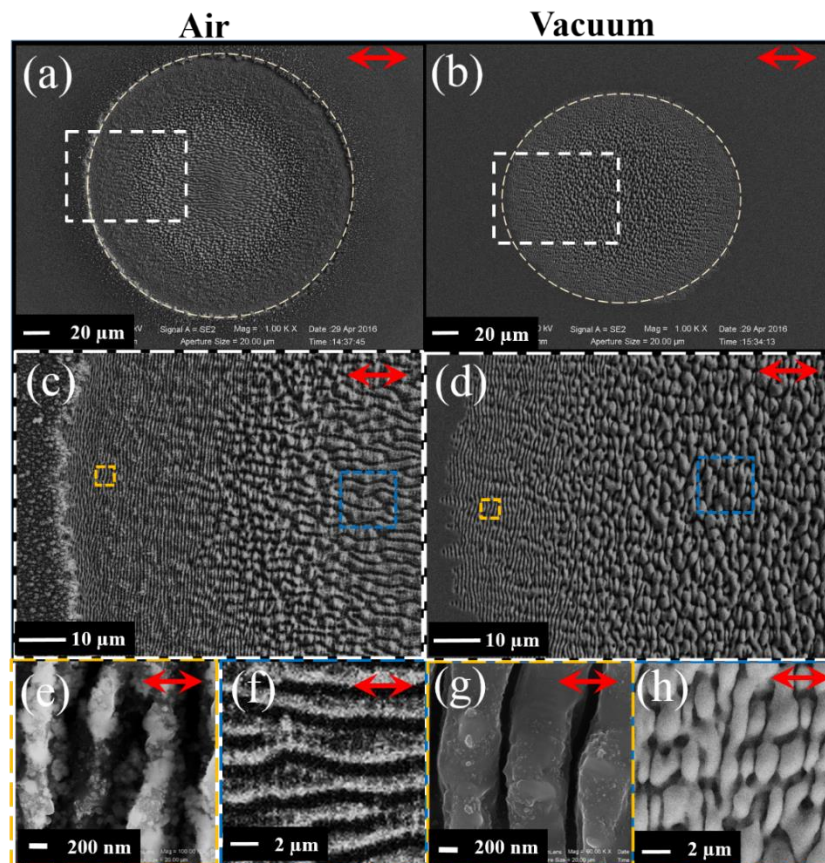


Figure 3.10| Examples of SEM micrographs illustrating the morphology of the surface spots generated in (a) air and (b) high vacuum, for an irradiation sequence of $N = 300$ laser pulses at a peak fluence $F_p = 0.64$ J/cm². The red arrows indicate the polarization direction. Panels (c) and (d) are zoomed views of the areas indicated by a box in (a) and (b), respectively. Panels (e), (g) and (f), (h) report SEM images of the corresponding, marked region as blue and yellow dotted squares in panel (c) and (d), registered at higher magnification, addressing the typical surface morphology characteristics for air and vacuum. The white dotted circle in panels (a) and (b) evidence the surface structured regions.

3.5.1 Direct comparison of surface structure generated at air & high vacuum conditions

Fig. 3.10 report typical SEM micrographs of the silicon surface spots in air (left panels) and high vacuum (right panels), for an irradiation sequence of $N = 300$ laser pulses at an energy $E_0 = 170 \mu\text{J}$ (peak fluence $F_p = (0.64 \pm 0.06) \text{ J/cm}^2$). In this case, experiments were carried out both in air and in high vacuum in with the same experimental setups. In the former case, the chamber is held at atmospheric pressure, while in the latter it is pumped down to a base pressure of $\sim 10^{-5}$ mbar. Therefore, the characteristics of the laser beam hitting the target surface are the same in both cases, except the ambient pressure. In the case of irradiation in air, Fig. 3.10(a) shows that the ablation spot is characterized by a circular shape with a radius of $\approx 92 \mu\text{m}$. From the Gaussian beam profile a corresponding ablation threshold of $F_{th,air} \approx 0.23 \text{ J/cm}^2$ is estimated, for $N=300$ pulses. The ablated crater presents a central, circular region with a radius $R_{G,air} \approx 50 \mu\text{m}$ characterized by quasi-periodic structure preferentially aligned along the beam polarization and with a spatial period of roughly 2-3 μm , which corresponds to grooves (Fig. 3.10(c) and inset). The grooved region is surrounded by an external ring-shaped area with a width of about 30 μm with sub-wavelength ripples aligned perpendicular to the laser polarization with an average period $\Lambda_{R,air} = (0.70 \pm 0.05) \mu\text{m}$ and present finer nanoscale structural features in forms of nanoparticle aggregates decoration. The intermediate narrow transitional region, between ripple and groove areas, of width $\approx 10 \mu\text{m}$ is characterized by grooves rudiments. This indicates a threshold fluence for the passage from ripples to grooves of $\sim 0.47 \text{ J/cm}^2$, for $N=300$ pulses. Finally, the crater is surrounded by a halo of nanoparticle aggregates extending for about 15-20 μm around the ablated spot.

One of the primary feature of ablation in vacuum is that there is a negligible decoration of nanoparticle aggregates both in the periphery of the ablation spot and over the ripples. The difference between vacuum and air can be easily appreciated by comparing Fig. 3.10(e) and (h), which show zoomed views of the processed surface in the rippled region and central part of the spot for air and vacuum, respectively. Besides the negligible presence of nanoparticle aggregates, the ripples morphology is rather different with respect to air. The ripples produced in high vacuum (HV) are characterized by a larger average period $\Lambda_{R,HV} = (0.85 \pm 0.04) \mu\text{m}$, a wider characteristic thickness and a narrower separation channel with respect to air. Ripples are present in an external area limited on the inner side by a circle with a radius of $\sim 58 \mu\text{m}$. Then, after a very narrow transition region (width $\sim 3\text{-}5 \mu\text{m}$), the surface spot presents a central, nearly circular area whose

topography is completely different from the grooves observed in air, at similar local values of the laser pulse fluence. In particular, the central area is characterized by a peculiar microstructure in form of a multicellular pattern with elemental constituents preferentially elongated in direction normal to the laser polarization, whose length varies from few to tens of μm . These surface structures seem to result from the bulging of ripples or fusion of two or more ripples in the region of higher laser fluence, as suggested by the progressive coarsening of their size in direction of the laser polarization by moving towards the center of the spot.

Other noticeable differences are the size and shape of the ablated area. Unlike in air, reduced size of the spot suggests a higher ablation threshold in vacuum, $F_{th,HV}$. From the Gaussian beam profile and the sizes of the ellipse semi-axes the value of $F_{th,HV}$ varies between $\approx 0.30 \text{ J/cm}^2$ and $\approx 0.35 \text{ J/cm}^2$, which corresponds to a reduction in fluence threshold of $\sim 35\%$ passing from vacuum to air. This can be associated to the different morphology of the target surface in air due to the surface roughness developed by the progressive decoration of nanoparticle with N. This gradual change in the texture can modify its absorption properties, eventually producing colored or blackened surfaces in the visible region [1], [35], [36]. Associating a defined threshold of absorbed laser fluence $F_{th,abs}$ to the material thermo-physical properties, one should then expect that $F_{th,abs} = A_{air} \times F_{th,air} = A_{HV} \times F_{th,HV}$. Consequently, one can estimate that $A_{air}/A_{HV} = F_{th,HV}/F_{th,air} \approx (1.30-1.52)$, which is consistent with the increased absorbance of the silicon target surface processed in air at the laser wavelength due to the generated surface texture. Hence, the size reduction of the structured surface spot in vacuum can be reliably associated to a change of absorption of the targets surface for laser irradiation in air and in high vacuum conditions. However, additional investigations are needed to clarify further possible effects related to the influence of the oxygen ambient inducing chemical effects that possibly affect the final sample morphology during processing in air.

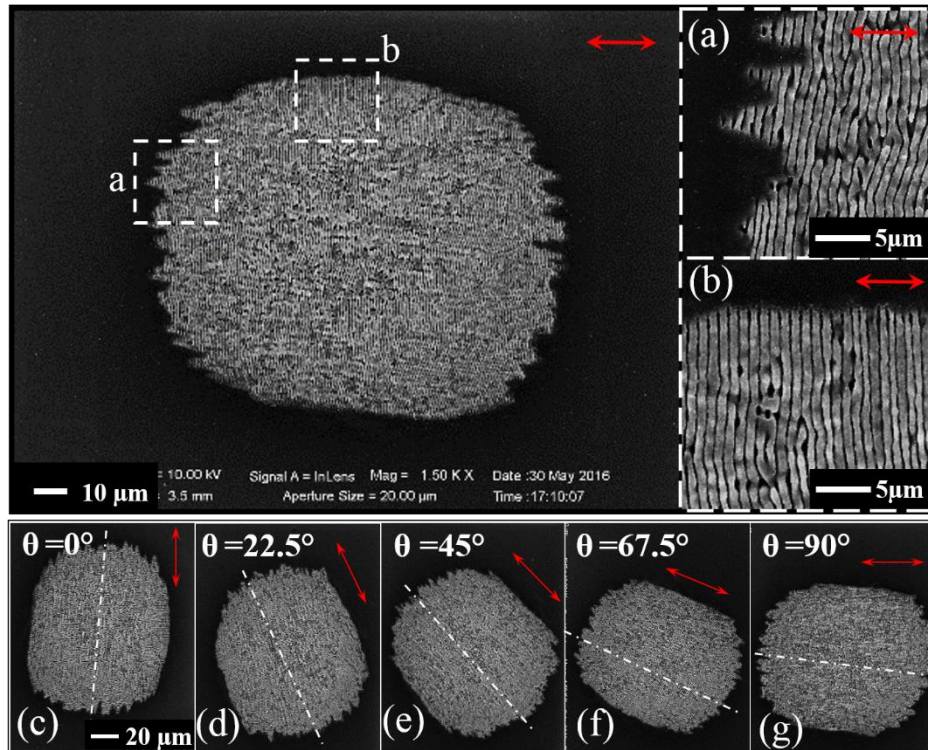


Figure 3.11/ SEM micrograph of the surface spot generated in high vacuum, for an irradiation sequence of $N = 200$ laser pulses at a peak fluence $F_p = 0.45 \text{ J/cm}^2$. The red arrows indicate the polarization direction. Panels (a) and (b) are zoomed views of the area indicated by boxes in the main panel. IL image of the spot showing the rotation of the elliptical spot from $\theta = 0^\circ$ to 90° is shown in panel (c) to (g).

As for the elliptical shape of the spot in vacuum, it is worth noticing that its edges parallel and normal to the laser beam polarization evidence a different morphology. This is addressed in Fig. 3.11(a), which reports a typical example of the elliptical surface structured spot generated with an irradiation sequence of $N=200$ laser pulses at a peak fluence $F_p = 0.45 \text{ J/cm}^2$. Zoomed views of the spot boundaries along the two directions are shown in insets (b) and (c) of Fig. 3.11. The periphery of the spot parallel to laser polarization ends abruptly. Instead, the spot contour normal to the laser polarization presents a jagged texture with many rippled arrowhead protrusions extending for several microns and preferentially pointing along the direction of the laser polarization. This diverse morphology of the peripheral regions of the spot is responsible for the approximately elliptical envelope of the surface structured area observed in high vacuum conditions. This effect can be rationalized as resulting from the interference between nearly-longitudinal scattered surface waves and the tail of the laser beam. A consistency analysis supports the idea that these scattered waves can be due to SPP generation at the plume periphery favored by ripples grating and surface roughness produced by previous laser pulses. Furthermore, this

clearly shows that the ripples formation is more favored along polarization direction and can be the reason for noticeable elongation of rippled spot parallel to the polarization. In the multiple-pulse case the SPP generation might be favored by the presence of the rather regular grating-like surface generated by previous pulses enhancing the coupling of the incoming radiation to SPP. Panel (c) to (g) of the Fig. 3.11 shows the IL image of the ablation spot in HV with rotating the beam polarization from $\theta=0^\circ$ to 90° with a steps of 22.5° , displaying the complete rotation of the elliptical ablation spot from vertical to horizontal direction by the rotation of rippled arrowhead formed at the spot periphery. The white dotted line is to follow the rotation of elliptical ablation spot corresponding to each laser polarization direction. As we discussed before, the side of the spot normal to the direction of polarization seems to be almost flat cut, instead along the polarization the edges are characterized by rippled arrowhead always pointing to direction of polarization irrespective of the rotation of linear polarization of laser beam. This further shows the effect of polarization on geometrical alignment of the ablation spot in relation with the directional scattering characteristics of SPP in gratings structure near the edge of the ablation crater [37].

3.5.2 Structure evolution with varying ambient pressure

There is an extensive literature which deals with the laser ablation and related plume characterization. Moreover, the nanoparticle dynamics and its evolution with ambient pressures are well characterized with different materials. Surface structure experiments done in ambient air suggests that nanoparticles have a strong influence in the formation of different surface structures [3], [6]. We have seen above that ambient pressure has a great effect on the ultrafast laser surface structuring by means of controlling the re-deposited nanoparticles flux on the target surface during the comparison studies done in air and vacuum. In order to further address these features, hereafter we discuss the variation occurring to ripples characteristics by carrying out surface structuring over a range of pressures. We focus on ripples because they are the only surface features present over the entire investigated pressure interval, ranging from 10^{-4} mbar to 1 bar.

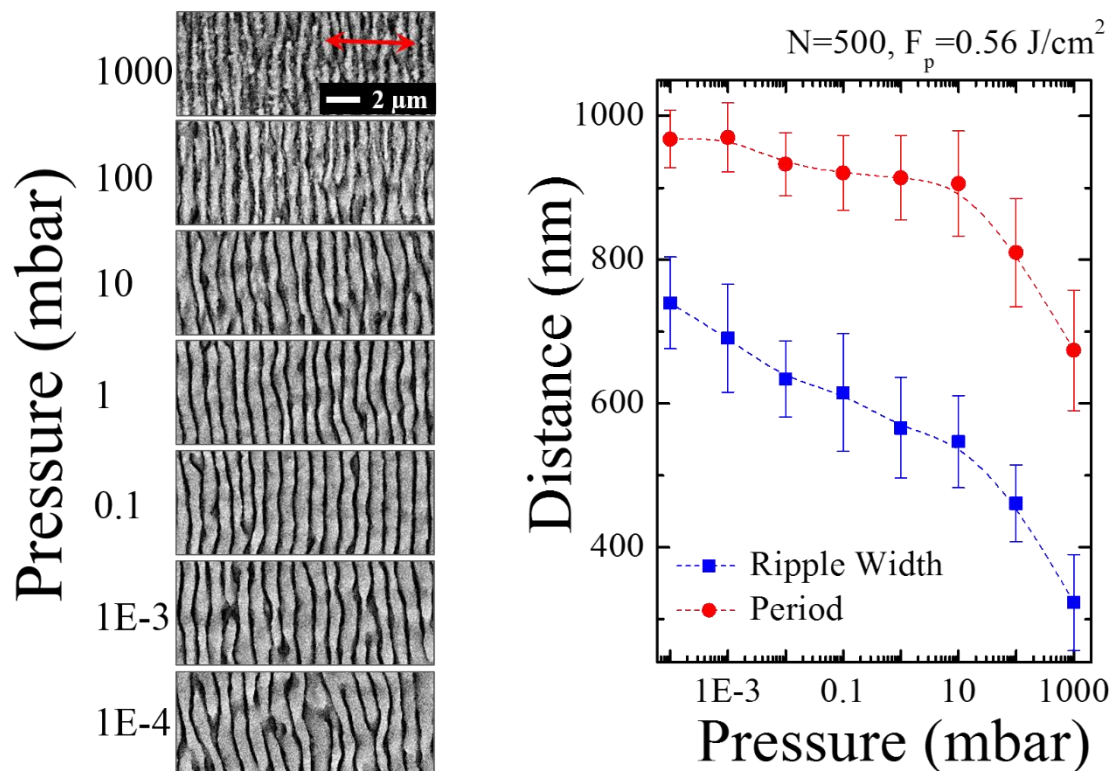


Figure 3.12| Left panel shows SEM micrographs of ripples generated at various ambient pressure ranging from 10^4 to 1000 mbar, for an irradiation sequence of $N = 300$ laser pulses at a peak fluence $F_p=0.56$ J/cm². The red arrows indicate the polarization direction. Right panel shows the variation of spatial period of ripples measured at each individual pressure values.

The left panel of the Fig. 3.12 reports SEM images of the ripple patterns clearly demonstrating a progressive change of the structure characteristics with pressure. The right panel of Fig. 3.12 shows the variation of the spatial period (Λ_R) and width (W_R) of individual ripples as a function of the pressure. The average ripples period varies from 970 nm to almost 650 nm, while ripples width reduces from more than 740 nm to a value around 323 nm during the variation of pressure from 1.5×10^{-4} mbar to 10^3 mbar. The contrast of surface structure is much larger at lower pressure, likely up to 10 mbar, and above which the surface gets decorated with nanoparticles. From the graph, W_R reduces much faster than the Λ_R , in fact slope of the both curve shows a sudden change at a pressure value around 10 mbar. This clear variation can be associated to the expansion dynamics of nanoparticle plume which gets confined after an ambient pressure of 10 mbar, restricting the free expansion of the nanoparticle plume away from the target surface [36]. As a result after 10 mbar the target surface is richly decorated with the re-deposited nanoparticles. Earlier, it has been shown that a target surface densely decorated with nanoparticle aggregates and nanostructures generated by multi-pulse ultrashort laser irradiation progressively modifies surface absorption properties [1], [38], [39]. This

change in the absorption parameters with elevation of pressure could be one reason for diverse change in the surface morphology of the ripples in silicon. Finally, such structure may exhibit contrasting optical and wetting properties opening possibility of one more degree of freedom in tuning the surface characteristics. This aspect will deserve focused investigations in the next future.

3.6 Conclusive Remarks

The interesting aspects of the direct ultrashort laser surface structuring process with Gaussian beam which allow gaining deeper information on the mechanisms involved in the generation of quasi-periodic surface structures on silicon are addressed. The two commonly formed fs LIPSS quasi-periodic patterns, subwavelength ripples and micron-sized grooves with a preferential alignment normal and in the direction of laser polarization, respectively, are investigated. The generation mechanism of ripples are explained as a result of inhomogeneous absorption of the laser pulse energy due to an energy modulation over the laser irradiated surface. Sipe's theory that states the interference of the incident beam with a "surface-scattered wave" originating from the pre-existing surface defects, as a responsible mechanism for the energy modulation is associated to Drude model to include the dielectric variation of target surface during ultrashort pulse irradiation with the aid of two-temperature model and free carrier dynamics. The good agreement between 2D-IFT maps of efficacy factor predicted by Sipe-Drude model and experimental results provide a direct clue on the fact that the energy modulation is responsible for annular ripples formation as well as bending/bifurcation features of ripples observed at different excitation conditions. Experiments done at different ambient pressures supports an important influence of nanoparticle, coming from the re-deposition of ablated material flux, in the generation and morphology of the surface structures. The absence of grooves and increase in the spatial period and width of the ripples are primary effect of direct fs laser surface structuring in reduced ambient pressure. The ripples formation is monitored over pressures ranging from 10^{-4} mbar to 10^3 mbar gaining information on the complete evolution of their period and width. The gathered data on the various surface patterns achieved in different experimental conditions lends itself as a useful knowledge for designing structures on solid targets by using ultrashort pulses. Moreover, it might offer further striking possibilities in tailoring and controlling the final properties (e.g. optical, wetting, hydrophobicity, sensing, and so forth) of LIPSS fabricated by direct ultrashort laser surface structuring.

References

- [1] A. Y. Vorobyev and C. Guo, "Direct femtosecond laser surface nano/microstructuring and its applications," *Laser Photon. Rev.*, vol. 7, no. 3, pp. 385–407, May 2013.
- [2] M. Huang, F. Zhao, Y. Cheng, N. Xu, and Z. Xu, "Origin of laser-induced near-subwavelength ripples: interference between surface plasmons and incident laser," *ACS Nano*, vol. 3, no. 12, pp. 4062–4070, 2009.
- [3] S. He, J. JJ Nivas, K. K. Anoop, A. Vecchione, M. Hu, R. Bruzzese, and S. Amoruso, "Surface structures induced by ultrashort laser pulses: Formation mechanisms of ripples and grooves," *Appl. Surf. Sci.*, vol. 353, pp. 1214–1222, 2015.
- [4] G. D. Tsibidis, C. Fotakis, and E. Stratakis, "From ripples to spikes: A hydrodynamical mechanism to interpret femtosecond laser-induced self-assembled structures," *Phys. Rev. B - Condens. Matter Mater. Phys.*, vol. 92, no. 4, p. 41405, 2015.
- [5] J. Song, J. Ye, X. Lin, Y. Dai, G. Ma, H. Li, Y. Jiang, and J. Qiu, "Discussion of the possible formation mechanism of near-wavelength ripples on silicon induced by femtosecond laser," *Appl. Phys. A Mater. Sci. Process.*, vol. 118, no. 3, pp. 1119–1125, 2014.
- [6] S. He, J. JJ Nivas, A. Vecchione, M. Hu, and S. Amoruso, "On the generation of grooves on crystalline silicon irradiated by femtosecond laser pulses," *Opt. Express*, vol. 24, no. 4, pp. 3238–3247, Feb. 2016.
- [7] T. H. Her, "Femtosecond-Laser-Induced Periodic Self-Organized Nanostructures," *Compr. Nanosci. Technol.*, vol. 4, pp. 277–314, 2011.
- [8] J. Bonse, S. Baudach, J. Krüger, W. Kautek, and M. Lenzner, "Femtosecond laser ablation of silicon - modification thresholds and morphology," *Appl. Phys. A*, vol. 74, no. 1, pp. 19–26, Jan. 2002.
- [9] M. Duocastella and C. B. Arnold, "Bessel and annular beams for materials processing," *Laser Photon. Rev.*, vol. 6, no. 5, pp. 607–621, 2012.
- [10] S. Höhm, M. Herzlieb, A. Rosenfeld, J. Krüger, and J. Bonse, "Femtosecond laser-induced periodic surface structures on silicon upon polarization controlled two-color double-pulse irradiation," *Opt. Express*, vol. 23, no. 1, p. 61, Jan. 2015.
- [11] S. Höhm, M. Rohloff, A. Rosenfeld, J. Krüger, and J. Bonse, "Dynamics of the formation of laser-induced periodic surface structures on dielectrics and semiconductors upon femtosecond laser pulse irradiation sequences," *Appl. Phys. A*, vol. 110, no. 3, pp. 553–557, Mar. 2013.
- [12] S. Höhm, A. Rosenfeld, J. Krüger, and J. Bonse, "Area dependence of femtosecond laser-induced periodic surface structures for varying band gap materials after double pulse excitation," in *Applied Surface Science*, 2013, vol. 278, pp. 7–12.
- [13] G. D. Tsibidis, E. Stratakis, P. A. Loukakos, and C. Fotakis, "Controlled ultrashort-pulse laser-induced ripple formation on semiconductors," *Appl. Phys. A Mater. Sci. Process.*, vol. 114, no. 1, pp. 57–68, 2014.
- [14] S. He, J. JJ Nivas, A. Vecchione, M. Hu, and S. Amoruso, "On the generation of periodic grooves on crystalline silicon irradiated by femtosecond laser pulses," *Opt. Express*, vol. 24, no. 4, pp. 3238–3247, 2015.
- [15] J. Bonse and J. Krüger, "Pulse number dependence of laser-induced periodic surface structures for femtosecond laser irradiation of silicon," *J. Appl. Phys.*, vol. 108, no. 3, p. 34903, 2010.
- [16] J. Bonse, M. Munz, and H. Sturm, "Structure formation on the surface of indium phosphide irradiated by femtosecond laser pulses," *J. Appl. Phys.*, vol. 97, no. 1, p. 13538, 2005.
- [17] O. Varlamova, M. Bounhalli, and J. Reif, "Influence of irradiation dose on laser-induced surface nanostructures on silicon," *Appl. Surf. Sci.*, vol. 278, pp. 62–66, 2013.
- [18] O. Varlamova and J. Reif, "Evolution of Femtosecond Laser Induced Surface Structures at Low Number of Pulses near the Ablation Threshold," *JLMN-Journal of Laser Micro/Nanoengineering*, vol. 8, no. 3, p. 300, 2013.
- [19] J. JJ Nivas, S. He, A. Rubano, A. Vecchione, D. Paparo, L. Marrucci, R. Bruzzese, and S. Amoruso, "Direct Femtosecond Laser Surface Structuring with Optical Vortex Beams Generated by a q-plate," *Sci. Rep.*, vol. 5, p. 17929, Dec. 2015.
- [20] Y. Han and S. Qu, "The ripples and nanoparticles on silicon irradiated by femtosecond laser," *Chem. Phys. Lett.*, vol. 495, no. 4, pp. 241–244, 2010.
- [21] G. D. Tsibidis, M. Barberoglou, P. A. Loukakos, E. Stratakis, and C. Fotakis, "Dynamics of ripple formation on silicon surfaces by ultrashort laser pulses in subablation conditions," *Phys. Rev. B*, vol. 86, no. 11, p. 115316, 2012.
- [22] J. Bonse, A. Rosenfeld, and J. Krüger, "Implications of transient changes of optical and surface properties of solids during femtosecond laser pulse irradiation to the formation of laser-induced periodic surface structures," *Appl. Surf. Sci.*, vol. 257, no. 12, pp. 5420–5423, 2011.

- [23] J. M. Liu, "Simple technique for measurements of pulsed Gaussian-beam spot sizes," *Opt. Lett.*, vol. 7, no. 5, pp. 196–198, May 1982.
- [24] S. L. Chin, T.-J. Wang, C. Marceau, J. Wu, J. S. Liu, O. Kosareva, N. Panov, Y. P. Chen, J.-F. Daigle, S. Yuan, A. Azarm, W. W. Liu, T. Seideman, H. P. Zeng, M. Richardson, R. Li, and Z. Z. Xu, "Advances in intense femtosecond laser filamentation in air," *Laser Phys.*, vol. 22, no. 1, pp. 1–53, 2012.
- [25] K. K. Anoop, A. Rubano, R. Fittipaldi, X. Wang, D. Paparo, A. Vecchione, L. Marrucci, R. Bruzzese, and S. Amoruso, "Femtosecond laser surface structuring of silicon using optical vortex beams generated by a q-plate," *Appl. Phys. Lett.*, vol. 104, no. 24, p. 241604, Jun. 2014.
- [26] J. E. Sipe, J. F. Young, J. S. Preston, and H. M. van Driel, "Laser-induced periodic surface structure. I. Theory," *Phys. Rev. B*, vol. 27, no. 2, pp. 1141–1154, Jan. 1983.
- [27] J. Bonse, A. Rosenfeld, and J. Krüger, "On the role of surface plasmon polaritons in the formation of laser-induced periodic surface structures upon irradiation of silicon by femtosecond-laser pulses," *J. Appl. Phys.*, vol. 106, no. 10, p. 104910, Nov. 2009.
- [28] D. C. Emmony, R. P. Howson, and L. J. Willis, "Laser mirror damage in germanium at 10.6 μm ," *Appl. Phys. Lett.*, vol. 23, no. 11, p. 598, 1973.
- [29] J. Bonse, S. Höhm, A. Rosenfeld, and J. Krüger, "Sub-100-nm laser-induced periodic surface structures upon irradiation of titanium by Ti: sapphire femtosecond laser pulses in air," *Appl. Phys. A*, vol. 110, no. 3, pp. 547–551, 2013.
- [30] T. J.-Y. Derrier, R. Koter, J. Krüger, S. Höhm, A. Rosenfeld, and J. Bonse, "Plasmonic formation mechanism of periodic 100-nm-structures upon femtosecond laser irradiation of silicon in water," *J. Appl. Phys.*, vol. 116, no. 7, p. 74902, Aug. 2014.
- [31] J. Bonse, S. Baudach, J. Krüger, W. Kautek, and M. Lenzner, "Femtosecond laser ablation of silicon - modification thresholds and morphology," *Appl. Phys. A*, vol. 74, no. 1, pp. 19–25, 2002.
- [32] A. Pereira, P. Delaporte, M. Sentis, W. Marine, A. L. Thomann, and C. Boulmer-Leborgne, "Optical and morphological investigation of backward-deposited layer induced by laser ablation of steel in ambient air," *J. Appl. Phys.*, vol. 98, no. 6, p. 64902, 2005.
- [33] K. C. Phillips, H. H. Gandhi, E. Mazur, and S. K. Sundaram, "Ultrafast laser processing of materials: a review," *Adv. Opt. Photonics*, vol. 7, no. 4, p. 684, Dec. 2015.
- [34] N. Tsakiris, K. K. Anoop, G. Ausanio, M. Gill-Comeau, R. Bruzzese, S. Amoruso, and L. J. Lewis, "Ultrashort laser ablation of bulk copper targets: Dynamics and size distribution of the generated nanoparticles," *J. Appl. Phys.*, vol. 115, no. 24, p. 243301, Jun. 2014.
- [35] S. Amoruso, R. Bruzzese, N. Spinelli, R. Velotta, M. Vitiello, X. Wang, G. Ausanio, V. Iannotti, and L. Lanotte, "Generation of silicon nanoparticles via femtosecond laser ablation in vacuum," *Appl. Phys. Lett.*, vol. 84, no. 22, pp. 4502–4504, 2004.
- [36] S. Amoruso, R. Bruzzese, X. Wang, and J. Xia, "Propagation of a femtosecond pulsed laser ablation plume into a background atmosphere," *Appl. Phys. Lett.*, vol. 92, no. 4, p. 41503, Jan. 2008.
- [37] J. Bonse, S. Hohm, S. V. Kirner, A. Rosenfeld, and J. Krüger, "Laser-Induced Periodic Surface Structures—A Scientific Evergreen," *IEEE J. Sel. Top. Quantum Electron.*, vol. 23, no. 3, pp. 1–15, May 2017.
- [38] A. Y. Vorobyev and C. Guo, "Enhanced absorptance of gold following multipulse femtosecond laser ablation," *Phys. Rev. B*, vol. 72, no. 19, p. 195422, Nov. 2005.
- [39] A. Y. Vorobyev and C. Guo, "Direct creation of black silicon using femtosecond laser pulses," *Appl. Surf. Sci.*, vol. 257, no. 16, pp. 7291–7294, 2011.

Surface structuring with femtosecond optical vortex beams

“This chapter highlights the main aspects of surface structuring with fs optical OV beams with $m=1$ generated by a q -plate ($q=+1/2$). OV beams with azimuthal, radial, spiral and linear SoP in the transverse plane are employed in the process which enables not only to generate complex surface patterns but also to characterize the OV beam in the focal plane. Interaction with more complex OV SoP, such as the one generated with additional $\lambda/4$ plates, gives interesting patterns of ripples and grooves. Results showing the laser structuring with higher OAM beams, such as $m=2$ and 5, are also included in order to illustrate the ability of laser induced structure in following the much more complex beam polarization pattern.”

4.1 Introduction

The crucial role of surface morphology in modifying the surface properties of the materials accounts for the growing interest in micro-machining of metals, semiconductors and insulators in view of diverse applications based on the properties of the processed surfaces. The previous chapter demonstrates the potential capabilities of direct fs laser surface processing in fabricating surface structures at nano- and micro-scales on solids by a fs beam with a Gaussian spatial intensity profile. The results demonstrate that beam characteristics, like polarization, spatial intensity distribution, number of pulses and laser fluence have great impact on the surface structuring and related processes. In particular, previous chapter demonstrates surface structuring by means of laser beam having a scalar optical field with a uniform polarization in the transverse plane. Recently, the so-called vector vortex beams [1] have gained considerable attention as a novel possibility in laser-matter interactions and related applications [2]–[4]. In comparison with the homogeneously polarized conventional Gaussian beam, vector beams have several unique features and are emphasized more clearly in [1], [5], [6]. Apart from the non-Gaussian spatial intensity profiles, such a kind of optical beam has a space-variant light polarization in the beam transverse plane. Above all, the singular vector beam gained great interest because the polarization

distribution in the beam transverse plane has a vectorial singularity, where the phase and polarization are undefined. Optical vortices are light beams carrying a definite Orbital Angular Momentum (OAM) being characterized by a helical wave-front and controllable polarization patterns [4], [7], which can offer the possibility of generating more complex surface structures [8]–[14] than conventional Gaussian beams. In vector vortex beams, polarization singular points are often coincident with corresponding singular points in the optical phase [5]. Radial or azimuthal polarized beam are the two most common kind of OV polarization configurations for the case of beam with OAM $m=1$. Recently, generation of high power vector beams such as fs OV beam has gained considerable attention in the field of material ablation due to its distinctive properties. In particular, radial/azimuthal polarized OV beams are studied because of their unique behavior of generating/hindering a strong longitudinal electric field under tight focusing conditions depending on their specific state of polarization (SoP). For example, under tight focusing conditions a radially polarized beam generates strong longitudinal field projecting maximum intensity on optical axis in the focal plane, which enables creating sharp focal points, significantly smaller ($0.16\lambda^2$) than that of a fundamental Gaussian beam with linear polarization ($0.2\lambda^2$). On the other hand, an azimuthally polarized beam does not support this longitudinal component that further makes it a suitable tool for precision nanostructuring to create annular geometries [15].

Before discussing our experiments with OV beams, it is worth briefly reviewing the current literature on material processing with this kind of beams. The OV laser ablation has proved its capability in numerous investigations. The use of OV beams in laser surface structuring has recently led to the generation of subwavelength annular ring structures on silicon or glass [16], [17] and the production of surface microstructures on stainless steel, silicon, and copper [11], [13], [14], [18]. Toyoda et al. demonstrated a twisting effect in metal by ablation with OV beam forming chiral nanoneedles caused by helicity transfer from the optical vortex to the melted material. Furthermore, just by changing the sign of the optical vortex helicity the chirality of the nanoneedles was controlled [19]. Other results showed that using nanosecond laser pulses in material such as stainless steel, brass and copper both azimuthal and radial polarizations are more efficient in drilling fine deep holes than a Gaussian beam with linear or circular polarization [20]. In another work Yoo et al., showed that the interaction of a donut-shaped laser beam with amorphous silicon film deposited over a fused silica substrate results in the effective collection of molten silicon in the beam center, thus producing a nanodome of dramatically increased height via thermocapillary

induced dewetting process. The fast melting and solidification process is responsible for the phase transformation from amorphous to crystalline structure [21]. In the case of tight focusing conditions, ablation with fs beam clearly demonstrates the polarization sensitive nature of the annular laser beam which becomes more pronounced close to ablation threshold of the material [17]. The work done by Takahashi et al. with picosecond laser demonstrates the formation of a monocrystalline silicon needle recrystallized by irradiation with a picosecond vortex pulse. The height of the needle was also enhanced by superimposing several vortex pulses on the target, reaching approximately 40 μm after almost 12 consecutive pulses [22]. The two-dimensional microstructures generated on the silicon by the fs vector field with different topological charges demonstrate a clear rippled pattern with a preferential direction always normal to the laser polarization featuring formation of complex quasi-periodic patterns on the surface [23]. A recent theoretical and experimental work by Tsibidis et al. studies the surface profile and the periodicity of the ripples formed upon irradiation of Ni with radially polarized fs laser pulses, demonstrating the significant influence of the incident beam polarization on both morphological profile and size of the produced structures [24].

This chapter illustrates experimental results on surface structures produced on crystalline silicon (100) target, in air, by fs OV beams with definite OAM. The annular intensity pattern and controllable polarization of OV beam can offer the possibility of generating more complex surface structures compared to the conventional Gaussian beam. Actually, there is minimal research addressing the optimal conditions for the formation of the diverse surface structures produced during laser irradiation of a solid target with fs OV beam. Therefore, a detailed understanding of the threshold fluences for ablation as well as the effects of different SoP in the formation of the various surface microstructures is essential to achieve an accurate and reliable determination of the OV beam properties. This chapter mainly covers the structuring with an OV beam with $q=+1/2$ ($m=1$), showing many possible polarization configurations. However, some examples of the ablation with OV beams with higher values of the OAM (e.g. $q=1$ and $5/2$ which correspond to $m=2$ and 5 , respectively) are also briefly described. The use of fs OV beams allows one to further extend the possibilities offered by the more standard Gaussian beam approach in tailoring the morphological features of the surface structures. Furthermore, the structuring with complex and non-uniform diverse state of polarization generated by keeping wave plates in the OV beam

displays the limitation of such surface structures in following the fine variation of the beam polarization in creating the quasi-periodic surface structure.

4.2 Generation of fs OV beam from Gaussian beam by a q-plate

As mentioned before in our structuring work the OV beam is generated by employing an optical element called q-plate which act as converter. Fig. 4.1 indicates a schematic representation of OV beam generation with a q-plate. Detailed description regarding the q-plate and OV generation scheme used in the experimental setup were illustrated in Chapter 2. The left panel of Fig. 4.1 represents the intensity profile of the incoming Gaussian beam taken by a CCD and its 3D representation. In central panel the electrically tuned q-plate of $q=+1/2$, acts as an optical converter of scalar Gaussian to a vector beam with an orbital helicity $m=\pm 2q$ (q is called the charge of the vortex) [1]. The optical vortex beam with a helical wave-front and annular intensity pattern is presented in the right panel of the Fig.4.1.

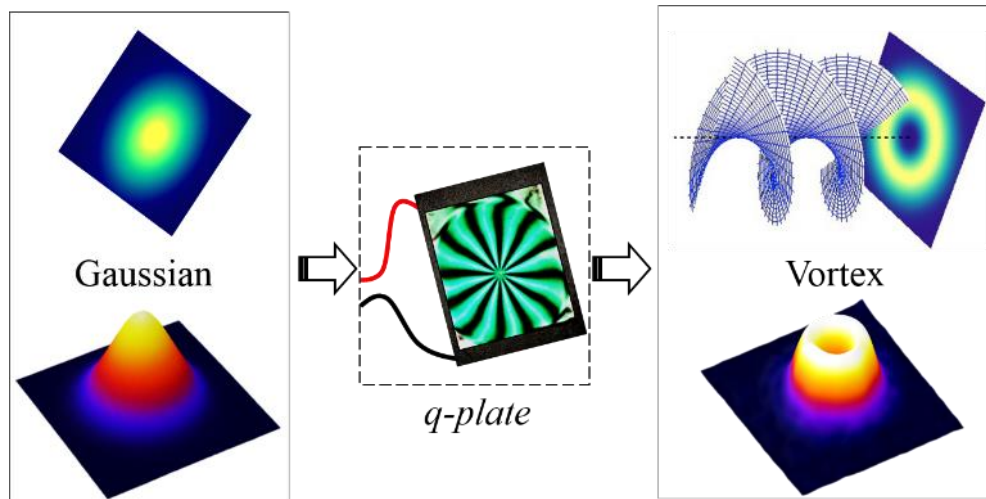


Figure 4.1/ Beam profile and 3D representation of incoming Gaussian and OV beams before and after the q plate module, respectively, are shown. The central panel shows a representative image of the q plate.

4.2.1 OV beams with $m=+1$ generated by a q-plate

Certainly polarization is an intrinsic and key element of light and the use of laser beams with a spatially inhomogeneous state of polarization (SoP) is bringing out novel breakthroughs on boundary line of fs laser material processing [25], [26]. OV beams offer numerous complex polarization patterns in a single laser beam, which open the possibility to generate complex surface

structures in a single step process. The employment of vector optical fields in direct fabrication of surface microstructures is emerging as a fascinating possibility and is proposed as an effective method for vector beams characterization [12], [13], [27] as well as for unconventional surface structuring [9]–[11], [14]. One interesting possibility to obtain an unconventional distribution of SoP is provided by a beam with non-vanishing OAM [4].

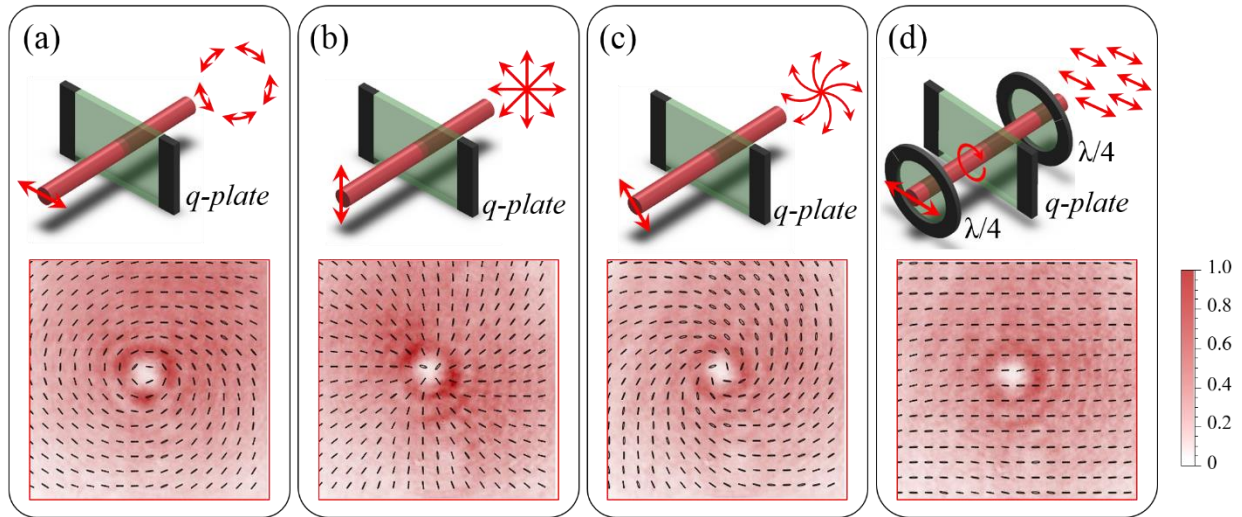


Figure 4.2| Schematics of the q -plate configurations used to generate OV beams with different polarization states. Panels (a) and (b) correspond to azimuthal and radial polarizations, respectively. Panel (c) displays the generation of spiral polarized OV beam and panel (d) corresponds to the case when a linear polarization is obtained in the transverse plane of the OV beam using two $\lambda/4$ wave plates before and after the q -plate with their optical axis orthogonal to each other.

This section reports on direct fs laser surface structuring using an optical vortex (OV) beam with OAM, primarily $m = \pm 1$ (per photon, in units of \hbar), with different spatial distributions of SoP. Indeed, radial and azimuthal SoP are the basic polarization patterns achieved with $m = \pm 1$ OV beams along with many intermediate spiral SoP which can be easily achieved by q -plate as illustrated in Fig. 4.2. Furthermore, an example of a linear polarized OV beam is shown in Fig. 4.2(d). The OV beam with radial, azimuthal and spiral SoP are obtained by rotating the incoming linear polarization to the q -plate as represented in Fig. 4.2(a), (b) and (c). The linear polarization is imparted to the OV beam by keeping two $\lambda/4$ wave plates before and after the q -plate with their respective axis 90° to each other. This provides a circularly polarized Gaussian beam to the q -plate which is then converted to a circularly polarized OV beam; the further passage through a second

$\lambda/4$ wave plate converts the local circular polarization to linear everywhere in the annular profile of the OV beam. The SoP is checked by using a horizontally-oriented polarizing filter and a beam profiler. To ensure the SoP of each complex OV beam a polarization tomography of each beam is conducted to achieve a 2D pattern of polarization distribution along the transverse direction of the beam as given in lower panel of Fig. 4.2. A brief description about the experimental set up and procedure for polarization tomography was given in chapter 2. For the surface structuring experiments, peak fluence, F_p , of the OV beam is varied by means of a system of half wave plate and polarizing beam splitter, while the number of pulses hitting the target surface, N , is selected by an electromechanical shutter. The system allows investigating the surface structuring with OV annular beams characterized by different SoP.

4.2.2 Direct material ablation with OV beams with $m=+1$

In the structuring of surface with OV beam a Ti:Sapphire laser having ≈ 35 fs and ≈ 800 nm central wavelength λ is employed. The fs OV beam is focused with a lens of 75 mm focal length on the crystalline silicon target. Detailed information regarding the entire experimental set up and procedure can be found in chapter 2.

Fig. 4.3(a) represents a CCD image of the OV beam showing an annular intensity profile. The spatial profile along the diameter is shown in Fig. 4.3(b). Fig. 4.3(c) reports the SEM image of the ablated target surface illustrating the complex surface pattern that can be generated by fs OV laser pulses with azimuthal SoP. The irradiating conditions are $N = 100$ and $E_0 = 48 \mu\text{J}$, which corresponds to a peak fluence $F_p = 0.53 \text{ J/cm}^2$. The resulting surface presents well oriented annular regions characterized by different surface morphologies. A central structure forms in the inner region of the OV beam with almost null intensity, which is constituted by an assembly of a large number of nanoparticles. A layer of nanoparticles is also present in the outer area of the OV beam. This indicates that random nanoparticles assembled nanostructures form in the central and external areas of the OV beam where the local fluence is lower than the ablation threshold. The ablated annular crater presents an inner ring-shaped region characterized by micron-sized grooves preferentially aligned along the local beam polarization. A zoomed view of these grooves is presented in the inset (red box) of Fig. 4.3(c) showing part of this region for azimuthal SoP. The grooved region extends over the most part of the ablation crater as shown in Fig. 4.3(c), and is surrounded by two adjacent, narrow ring-shaped areas (in either sides) with a characteristic texture

of subwavelength ripples aligned perpendicular to the laser local polarization. The other inset (yellow box) of Fig. 4.3(c) shows a zoomed view of the ripples for the azimuthal SoP.

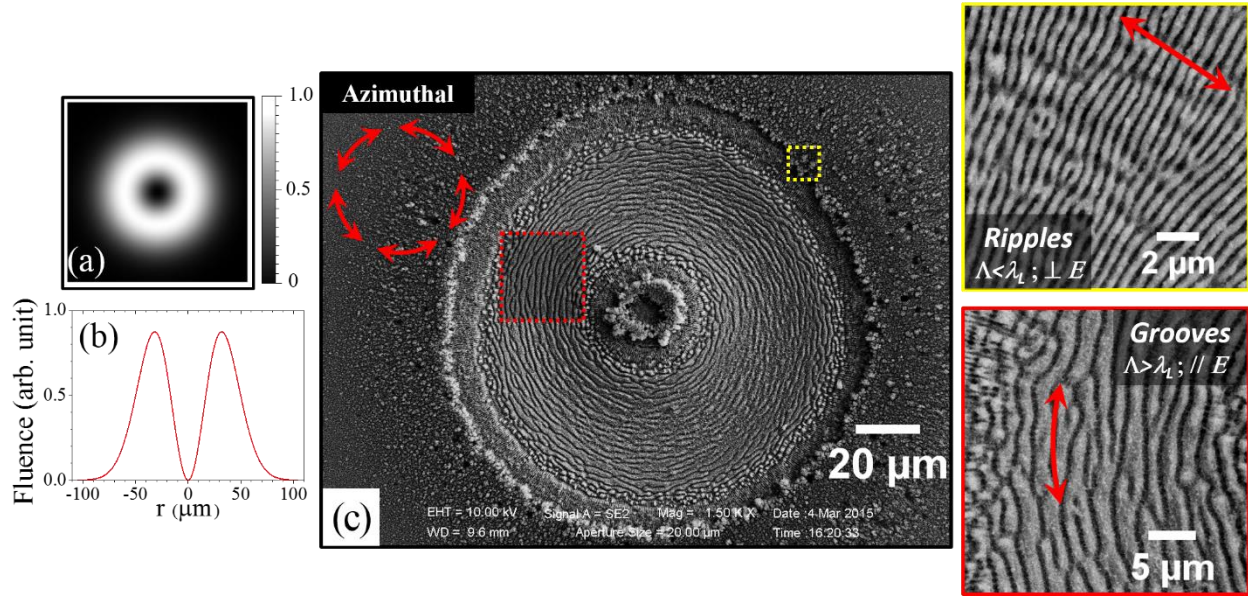


Figure 4.3 | Panel (a) reports an image of the OV beam and panel (b) shows its spatial intensity profile. Panel (c) is an example of surface structures developed on silicon after an irradiation sequence of $N=100$ pulses at an energy $E_0=48\mu\text{J}$ which equivalent to the pulse peak fluence $F_p=0.53\text{ J/cm}^2$ with azimuthal SoP. The two right panels illustrate the fine morphology of the surface structure: peripheral regions (yellow box) at the outer edges of the annular OV beam are namely characterized by subwavelength ripples oriented along the normal to the local laser polarization (double-ended arrow), while the internal region of the OV beam (red box) presents microgrooves preferentially directed along the local laser polarization. The fine surface texture observed for the other SoP shows the same characteristic features.

4.2.3 Influence of N and F_p on surface patterns

Both the overall width of the ablated crater and the thickness of the rippled and grooved annular regions depend on the spatial distribution of the OV laser peak fluence, F_p , as well as the number of pulses, N . As an example, Fig. 4.4 reports SEM images of the target surface after an irradiation sequence of N pulses with azimuthal SoP for two different values of the pulse fluence and number of pulses, namely (a) $N = 100$, $F_p = 0.21\text{ J/cm}^2$; (b) $N = 100$, $F_p = 0.53\text{ J/cm}^2$ and (c) $N = 20$, $F_p = 0.53\text{ J/cm}^2$. The lower panels show zoomed views of the surface corresponding to the regions identified by the yellow dashed boxes.

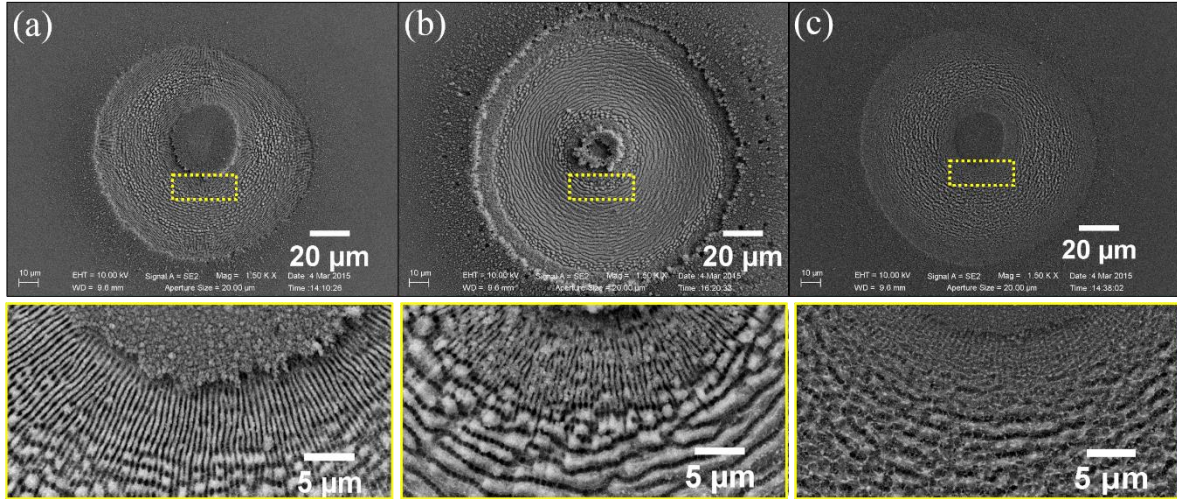


Figure 4.4/ SEM images of the surface structures on the silicon target after an irradiation sequence of N pulses with azimuthal SoP for two different values of the peak fluence and number of pulses: (a) $F_p = 0.21 \text{ J/cm}^2$, $N = 100$; (b) $F_p = 0.53 \text{ J/cm}^2$, $N = 100$; (c) $F_p = 0.53 \text{ J/cm}^2$, $N = 20$. The lower panels are zoomed views of the areas indicated by the red dashed box in the corresponding upper SEM images illustrating the dependence of the fine morphology of the surface structure on the laser pulse fluence F_p and number of irradiating pulses N .

At the lower fluence $F_p = 0.21 \text{ J/cm}^2$ for $N = 100$ (Fig. 4.4(a)), ripples dominate the surface texture of the annular crater, while grooves rudiments decorate the underlying ripples. At the same number of pulses $N = 100$ and higher fluence $F_p = 0.53 \text{ J/cm}^2$ (Fig. 4.4(b)), instead, well-developed grooves cover the inner part of the annular crater. Clear and sharp spatial transitions between the external rippled areas and the central grooved region occur, which suggests the existence of a well-defined threshold for the transition from ripples to grooves, as we have already seen in the case of Gaussian beams. Moreover, it also supports the idea that appropriate shaping of SoP and fluence profile can be used to fabricate diverse complex surface patterns. The comparison between Fig. 4.4(b) and (c) corresponding to $N = 100$ and $N = 20$, at the same fluence $F_p = 0.53 \text{ J/cm}^2$, allows addressing the role of the number of pulses. One can observe that at the lower value of N , at high fluence, the surface texture already shows characteristic features of grooves which are reinforced and well-developed as the pulse number increases.

4.2.4 Surface structuring with other possible SoP for an OV beam with $m=+1$

The SEM images in panels (a) and (b) of Fig. 4.5 show examples of ablation craters produced by radially and intermediate spirally polarized OV beams, respectively. The latter is generated by appropriate tuning of the half wave plate axis alignment with respect to the q-plate axis. Moreover,

as demonstrated in Fig. 4.5(c), linear surface patterns can also be realized within a ring-shaped region by exploiting two quarter wave plates (see Fig 4.2(d)).

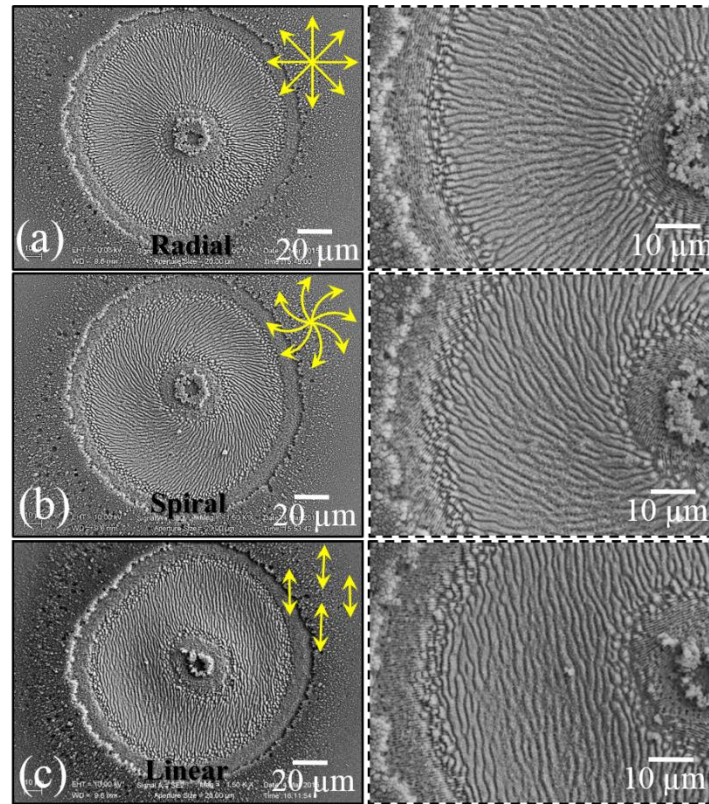


Figure 4.5/ SEM images of the surface structures on the silicon target after an irradiation sequence of $N=100$ pulses with $F_p=0.32 \text{ J/cm}^2$ with polarization of the OV beam radial, spiral and linear in panel (a),(b) and (c) respectively. The panels in the right side report zoomed views illustrating the closer view of the ripples and grooves alignments.

In each case, the grooves cover the significant part of the annular ablated area and ripples are located at the internal and external edges. It is interesting to note that, these micro and nano-structures display a clear relationship with the spatial distribution of laser beam intensity and polarization. Therefore, laser-induced structures and crater profiles can also be exploited as a direct way to diagnose intense, cylindrical vector beams in the focal plane [9], [12], [13], [17], [27], [28]. In all polarization conditions, it is demonstrated that the overall width of the ablated crater and the width of the rippled and grooved annular regions depend on the spatial distribution of the OV laser pulse fluence, F_p , as well as the number of pulses, N . The zoomed view corresponding to each images are provided in the right panel of Fig. 4.4 displaying the fine structure in the region of

annular crater within the dotted envelope. This illustrates the fact that appropriate shaping of SoP and fluence profile can be used to fabricate diverse complex surface patterns.

4.3 Threshold calculation for OV beam

Laser-induced structures and crater profiles have been used as a direct way to diagnose intense, cylindrical vector beams in the focal plane [8], [29]. Actually, there are not many studies addressing the optimal conditions for the formation of the diverse surface structures produced during laser irradiation of a solid target with fs OV beam. Therefore, a detailed understanding of the diverse threshold fluences for ablation and formation of the various surface microstructures is essential to achieve an accurate and reliable determination of the OV beam properties. For a fixed target, the properties of the ablation process are related to the specific beam characteristics. For laser beams with a Gaussian intensity profile, the beam characteristics are generally obtained by a well-established method based on the analysis of the lateral dimensions of the crater produced on the target [30], [31]. In particular, crater analyses allow determining beam waist, peak fluence of the laser pulse, as well as the fluence threshold for ablation of the target material and the conditions for the formation of specific surface structures. All these parameters are fundamental for an accurate description of the experimental conditions and for a clear analysis of the investigated processes. In this section the attention is given to an extensive analysis of crater and surface structures produced in direct fs laser ablation of silicon with an OV beam, illustrating an effective method for characterizing its properties [29]. The case we considered is with an OV beam carrying an OAM $m=1$, produced by a q-plate with a $q=1/2$. The spatial profile of the pulse fluence $F(r)$, along the diameter of an OV beam with $m=2q=1$, as a function of the radial coordinate r is described by the following distribution [4]:

$$F(r) = 2^2 E_0 \frac{r^2}{\pi w_0^4} e^{-\frac{2r^2}{w_0^2}} \quad (1)$$

where E_0 is the beam energy and w_0 the waist of the corresponding fundamental Gaussian beam. The distribution shows the presence of a null fluence at the beam center, and of a peak at the positions r_p given by:

$$r_p = \frac{w_0}{\sqrt{2}} \quad (2)$$

The corresponding peak fluence value F_p is:

$$F_p = F(r_p) = 2e^{-1} \frac{E_0}{\pi w_0^2} \approx 0.736 \frac{E_0}{\pi w_0^2} \quad (3)$$

Let us consider first the variation of the internal, R_{in} , and external, R_{ex} , radii as a function of E_0 . R_{in} and R_{ex} mark the threshold for ablation and ripples formation, respectively. Fig. 4.6(a) reports two examples of the experimental dependence of R_{in} and R_{ex} as a function of E_0 , for $N = 20$ and $N = 100$, in the case of irradiation with an azimuthally polarized OV beam. One can observe a progressive reduction of the width of the ablated annulus ($R_{ex} - R_{in}$) as the energy E_0 decreases. This annulus eventually degenerates into a limiting circumference with a radius $R_{in} = R_{ex} = r_p$ when E_0 reaches the threshold level E_{th} . Hence, the corresponding threshold peak fluence F_{th} can be obtained as:

$$F_{th} = 2^2 e^{-1} \frac{E_{th}}{\pi w_0^2} \quad (4)$$

The data were fitted through a numerical procedure and fitting curves are reported as solid lines in Fig. 4.6(a). The experimental data are well described by the two branches departing from the point of coordinates (E_{th}, r_p) and corresponding to R_{in} and R_{ex} versus E_0 . The beam waist w_0 and the threshold fluence F_{th} were used as fitting parameters, thus obtaining $w_0 = (46 \pm 2) \mu\text{m}$, and the values of F_{th} reported in Fig. 4.6(b) for three different N values. A progressive reduction of F_{th} with N is observed, which indicates the same incubation behavior observed with a Gaussian beam. The fit to the curve (solid line in Fig. 4.6(b)) yields $F_{th,1} = (0.27 \pm 0.04) \text{ J/cm}^2$ and $\xi = (0.81 \pm 0.05)$, consistent with the previous results observed with a Gaussian beam on silicon [31].

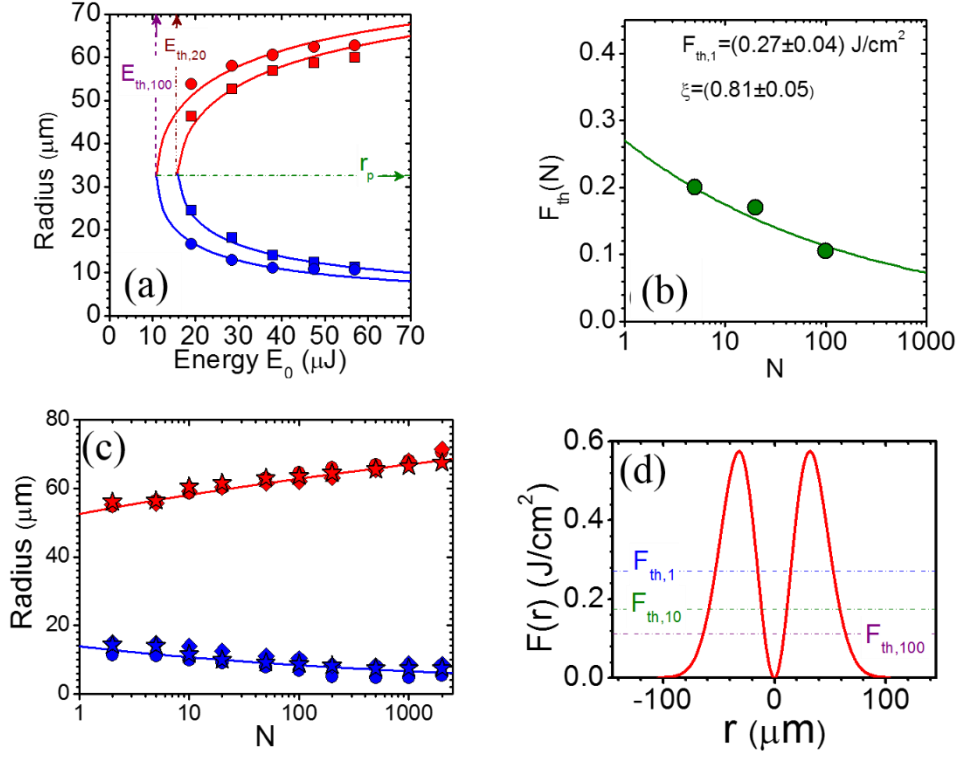


Figure 4.6| (a) Variation of the internal (R_{in} , blue) and external (R_{ex} , red) radii as a function of the OV beam energy E_0 for two different numbers of pulses N : squares, $N = 20$; circles, $N = 100$. The solid line indicates fits to the experimental data obtained through a numerically solving the Eq.(4) coupled with a minimization procedure. (b) Variation of F_{th} with N . The uncertainties on the experimental data points are contained within their respective size. The line is a fit to the dependence $F_{th,N} = F_{th,1} \times N^{\xi-1}$ with the values of the fitting parameters shown in the figure. (c) R_{in} and R_{ex} as a function of the number of pulses N for the OV beam with azimuthal (circles), radial (diamond), and circular (stars) polarizations, at a pulse energy $E_0 \approx 50 \mu\text{J}$ which is equivalent to a peak fluence $F_p = 0.53 \text{ J/cm}^2$. The solid lines are model dependence according to the incubation effect. (d) OV beam spatial profile and values of $F_{th,N}$ for $N = 1, 10$, and 100 as predicted by the incubation relation.

The analysis is also done for variation of the internal and external radii with the number of pulses N , in the case of OV beams characterized by azimuthal, radial, and circular polarizations, at a pulse energy $E_0 \approx 50 \mu\text{J}$ which corresponds to a peak fluence $F_p \sim 0.53 \text{ J/cm}^2$. The different OV polarization patterns were generated by appropriate rotation of the linear polarization of the input beam before the q-plate or by using a quarter-wave plate. The results are summarized in Fig. 4.6(c). A progressive rise in the width of the ablated annulus ($R_{ex} - R_{in}$) is observed as the number of laser pulses N increases, independent of the specific polarization. The solid curves in Fig. 4.6(c) show a model dependence obtained by taking into account the progressive reduction of the fluence threshold due to the incubation effect and illustrated in the inset for $N = 1, 10$, and 100 . The model prediction describes the experimental results quantitatively.

4.4 Effect of polarization using a shorter focal lens

The surface structuring with OV beam exemplified so far in this chapter are done at weak focusing conditions by using a simple plano-convex lens with a focal length of 75 mm. In the experimental conditions specified in Chapter 2, this generates an ablation spot with a diameter of about 100 μm to 120 μm on crystalline silicon. Under those circumstances, indeed, the local polarization controls the directional distribution of quasi-periodic structures but the overall crater geometry is pretty similar, irrespective of the OV beam polarization at fixed irradiation conditions. In fact, the area of the ablation crater is the same for irradiation with different SoP under the weak focusing conditions, as illustrated in the Fig. 4.6(c), which also suggests similar values of the ablation threshold for all SoP of OV beam.

As an additional investigation on the possible effects of polarization, an experiment was carried out with a focal length of about 25 mm, which is almost three times shorter compared to the earlier case (75 mm). Since the “depolarization effect” scales with the numerical aperture (NA) of the focusing optics [17], ablation at relatively tight focusing conditions should exhibit a significant change in the ablated area. Fig. 4.7(a) reports the variation of the radius of the ablation spot as a function of N registered in this case.

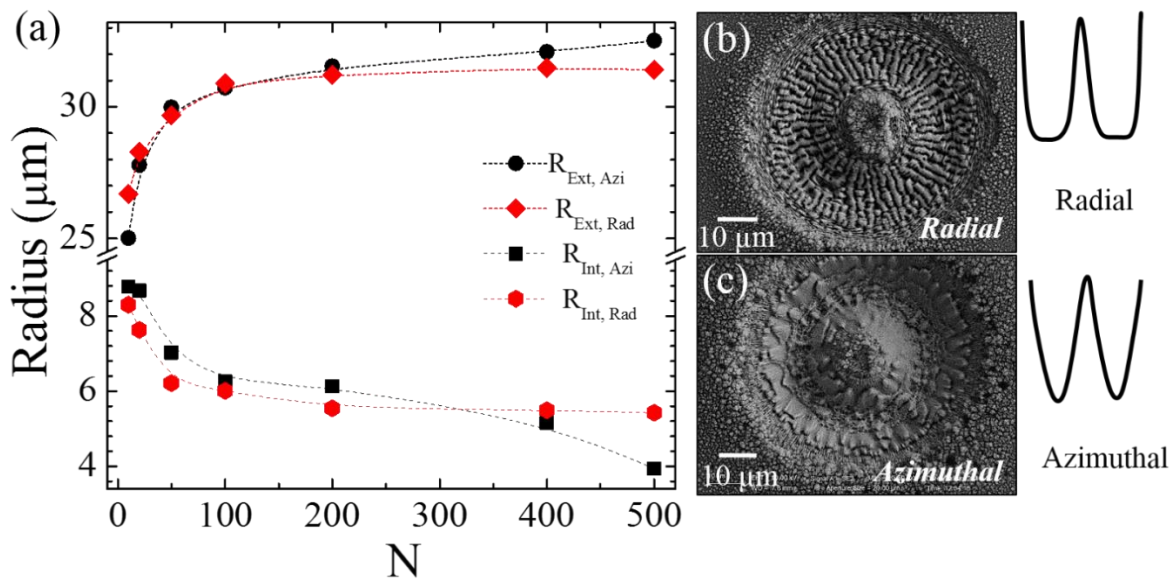


Figure 4.7/ Panel (a) shows the variation of internal and external radii of the spot for radial and azimuthal polarizations in medium focusing condition. Panels (b) and (c) show SEM images of the ablation spots generated by OV beams with radial and azimuthal polarizations, respectively, for an energy $E_0=0.5 \mu\text{J}$ corresponds to a peak fluence $\sim 0.12 \text{ J/cm}^2$ at $N=500$. Inset of panels (b) and (c) shows the diagram of expected shape of the hole cross sections in each polarization.

Fig. 4.7(a) reports the variation of the radius of the external and internal edges for azimuthally ($R_{\text{ext,azi}}$, $R_{\text{int,azi}}$) and radially ($R_{\text{ext,rad}}$, $R_{\text{int,rad}}$) polarized beams as a function of N . A change becomes clearly visible after $N > 200$. Since the radial and azimuthal SoP is obtained by rotating the incoming linear polarization to q-plate from horizontal to vertical direction, the intensity profile does not show any change in either condition. This primarily suggests a corresponding change in the ablation threshold at radial and azimuthal SoP for OV beam irradiation. SEM images of the ablation crater at $N=500$ for both radial and azimuthal case are reported in Fig. 4.7(b) and (c), respectively. In contrast to the previous results for weak focusing conditions, here the crater morphology shows great difference in either SoP of OV beam. In the case of Fig. 4.7(b), which corresponds to the radial polarized OV beam, majority of the ablated part is decorated with clear and well contrasted grooves covering an area with a width of $\sim 16 \mu\text{m}$. An annular region of thickness $\sim 3.2 \mu\text{m}$ with ripples is found near the external edge of the spot and very thin band ($\sim 1.4 \mu\text{m}$) of ripples near the internal edge. The central region of the spot with a diameter of $\sim 13 \mu\text{m}$ is decorated with abundant nanoparticles forming an island structure. On the other hand, for azimuthal polarization conditions, the crater forms a conical ablation crater (compared to a relatively flat geometry for the radial polarization) along the intense part of the beam with an annular profile. This further hinders the formation of any grooves but only a wavy like pattern is present over the inclined surface of the conical part of the crater with a characteristic width of $\sim 18.5 \mu\text{m}$. Here approximately $4.5 \mu\text{m}$ in external and $\sim 3.8 \mu\text{m}$ in internal part is covered by ripples. In comparison to the radial case, the ablated area and consequently the entire size of the spot results larger for ablation with the azimuthal polarized OV beam, as indicated in the Fig. 4.7(a). Hence, Fig. 4.7 illustrates an experimental situation in which the OV beam generated ablation crater presents very dissimilar geometries and the formation of surface structures with rather different fine features. However, presence of a non-ablated central part for radial SoP points to the fact that the intensity at center part of the beam at the focus is almost negligible, in our experimental conditions. Consequently, this phenomenon is not related to the longitudinal field effect usually found in tight focusing conditions for which the central singularity vanishes at higher values of N for radial SoP using objective lens [17]. Instead, this can be addressed as a way to evidence the diverse characteristics of the OV beam SoP in the case of medium focusing conditions provided by a simple short focal lens, in which the main component of the electric field is transverse (i.e. it is directed in the plane of the target) and the longitudinal field is almost

negligible. In the case of both radial and azimuthal SoP conditions, the energy deposition on the sample is independent of azimuthal angle since both polarization possess cylindrical symmetry [20]. Therefore, the increased absorption for radial SoP, compared to azimuthal, can be rationalized as due to the fact that in the case of OV beam and shaped crater, the radial SoP can have p-polarized components, while in the azimuthal case the beam will be always s-polarized with respect to the interface. In fact, in comparison with s-polarized beam, p-polarized light is absorbed more efficiently [32]. This leads to an increased ablation depth per pulse for the radially polarized OV beam irrespective of relative incident angle for annular intensity profile along radial direction. Subsequently, a depth profile that lacks intermediate angles and becomes more and more box-like is generated for radially polarized beam at larger N due to more effective ablation. In contrast, for an azimuthal polarized beam, absorption coefficient shows minor changes on the angle of incidence and the depth profile should more or less resemble the beam intensity profile [20]. This explains the differences between the craters produced by OV beams with the two SoPs reported in Fig. 4.7. Such an effect is pretty much used in laser drilling with cylindrical beams.

4.5 Surface pattern generated by OV beams with more complex polarization

As shown earlier, OV beams with radial, azimuthal, spiral and linear SoP facilitate the generation of complex surface patterns on silicon. In this respect, the analysis of surface structures was also pointed out as an effective method to characterize ultrashort laser pulses with complex distribution of polarization in the transverse plane. However, it should be worth to understand how far this ripples and grooves can effectively follow the fine features of the local polarization pattern when the SoP of the laser beam becomes more and more complex. Similarly, the following discussion emphasizes on the generation of OV beams with spatially variant polarization in the transverse plane and the analysis of the surface pattern engraved in the crystalline silicon.

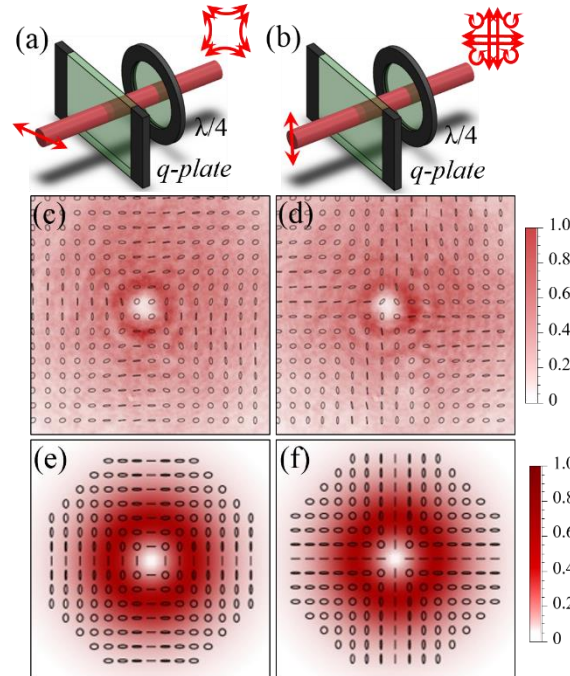


Figure 4.8/ Complex SoP generated for OV beam with $m=1$: Panel (a) and (b) show two optical setups consisting of q-plate and $\lambda/4$ wave plate converting radial and azimuthal polarization to corresponding complex SoP as indicated. Panel (c) and (d) represent the beam polarization patterns in the near-field obtained vector field have been generated by point-by-point Stokes parameters tomography in the beam transverse plane as explained in Ref. [5]. The polarization intensity pattern in the far-field is obtained by simulation and is provided in the panel (e) and (f), respectively.

In the search of more complex OV beam with $m=1$, an experiment was carried out to study the kind of SoP generated with additional optical elements, like wave plates, in the OV beam path. In particular, two cases of OV beam polarization are considered, such as (i) OV with azimuthal polarization entering to the $\lambda/4$ plate and (ii) radially polarized beam entering the $\lambda/4$ plate. In Fig. 4.8 panels (a) and (b) represent the optical set up consisting of q-plate and $\lambda/4$ plate generating complex SoP. In order to understand the exact polarization pattern of the OV beam after the wave plate, a polarization tomography is conducted by imaging laser beam in the near-field by point-by-point Stokes parameters tomography in the beam transverse plane [5]. The results are displayed in the panels (c) and (d) of the Fig. 4.8, in which the local beam polarization is represented as the orientation of a polarization ellipse. By following the method described in the Ref. [33], the theoretical spatial profiles of the laser fluence and SoP in the focal plane in both cases are obtained by simulating the optical field propagation corresponding to the OV beam and are displayed in panel (e) and (f) of Fig. 4.8. The simulation results of the beam corresponds to a smooth transition in the local polarization from linear to circular while advancing the azimuthal angle of 45° in each

quadrant. The direction of local linear polarization and the azimuthal angle in the transverse plane of the beam where linear and circular polarization exist depending on the SoP of incoming OV polarization (azimuthal or radial) and optical axis of the $\lambda/4$ plate.

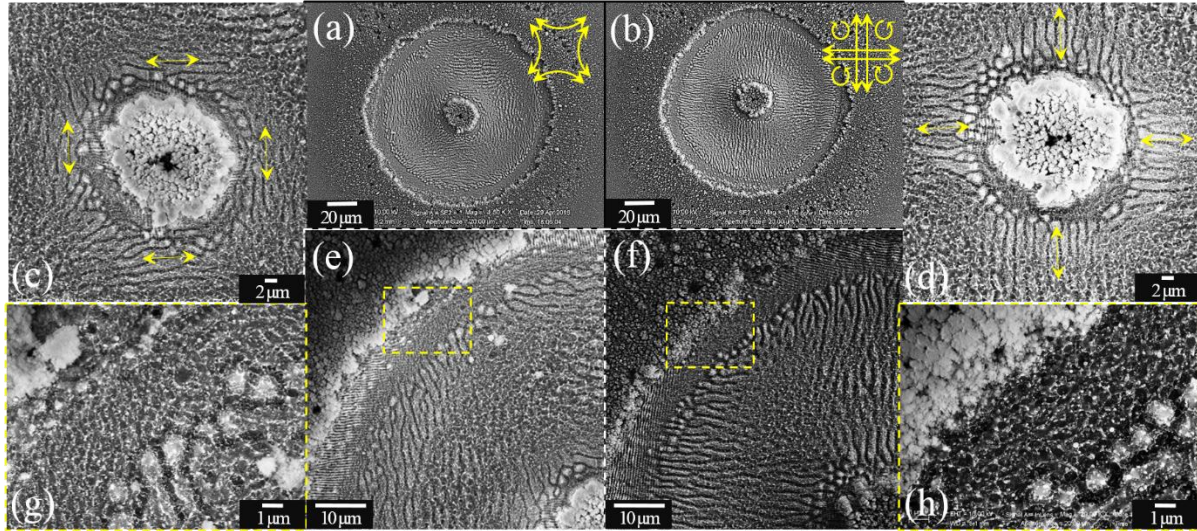


Figure 4.9| Example of structuring with OV beam of $m=1$ with complex polarization distribution: Panel (a) and (b) shows two complex OV polarization schemes obtained by using a $\lambda/4$ retardation plate as shown in Fig. 4.8. Panel (c) and (d) represent the central region of the ablated spot corresponding to the beam singularity. The region near the spot edge with an annular geometry is reported in panels (e) and (f) and zoomed views of the outer rippled area are shown in panel (g) and (h), respectively.

Fig. 4.9(a) and (b) display SEM images of the structures generated with OV beams with complex polarization distribution reported in Fig. 4.8(a) and (b), respectively. Panel (c) and (d) of Fig. 4.9 represent the non-ablated central region of the spot corresponding to the beam singularity. The double headed arrows indicated the direction of local polarization. The center region, of null intensity, is decorated with clusters of nanoparticles which are surrounded by differently oriented grooves in all four directions. Moreover, a thin band of ripples oriented normal to the local polarization direction is also visible near the central region. The SEM image of the region displaying one quarter of the spot edge with an annular geometry is given in panel (e) and (f), while their zoomed views in the outer area are shown in panel (g) and (h), respectively. Grooves oriented along the direction of the local polarization are present in the region where the local polarization is either linear or slightly elliptical. Instead, in the region of the spot where local polarization smoothly transforms to circular, no periodic surface features are formed. IL-SEM images showing the zoomed view of the region corresponding to circular polarization are provided

in panel (g) and (h) of Fig. 4.9. They show nanometer scale random features in the lower fluence part and similar larger structures in the higher fluence region with an interface featured with spherical island structures. This suggests that laser induced quasi-periodic surface features are not effectively generated in the case of fs OV beam composed of different polarizations varying from the circular to linear in the same transverse plane. From the first understanding, no clear ripples or grooves are formed in the region corresponding to circular polarization. By comparing the polarization pattern generated from the tomography method or the simulation result, it is clear that in the region of elliptical polarization, the ripples or grooves are formed along a direction of major axis of the polarization ellipse. This depicts one possible limitation of laser induced surface structuring as a tool of characterizing local polarization distribution of the intense fs OV beam with very complex polarization in the transverse plane.

4.6 Ablation with higher OAM optical vortex beam

Laser beams with OAM $m=1$ offer the possibility to generate surface patterns with still larger variety of available polarization states compared to scalar laser beams. In addition to the ultrashort behavior, the changeable spatial distribution of SoP of the fs OV beam can undoubtedly produce a miscellaneous of surface structures and thus open up numerous possible applications. Furthermore, a beam with higher OAM ($m>1$) possess still more complex distribution of the polarization in the transverse plane in addition to the auxiliary rotation in the phase pattern. Fig. 4.9 shows the intensity (upper panel) and phase pattern (lower panel) for the case of $m=-2, -1, 0, 1$ and 2. The $-ve$ and $+ve$ 'm' value simply denotes the direction of rotation of helical phase front and $m=0$ denotes the general scalar field of Gaussian beam. The color scales on the right side represent normalized intensity value for images of central panels and the phase for the phase profiles reported in the lower panels.

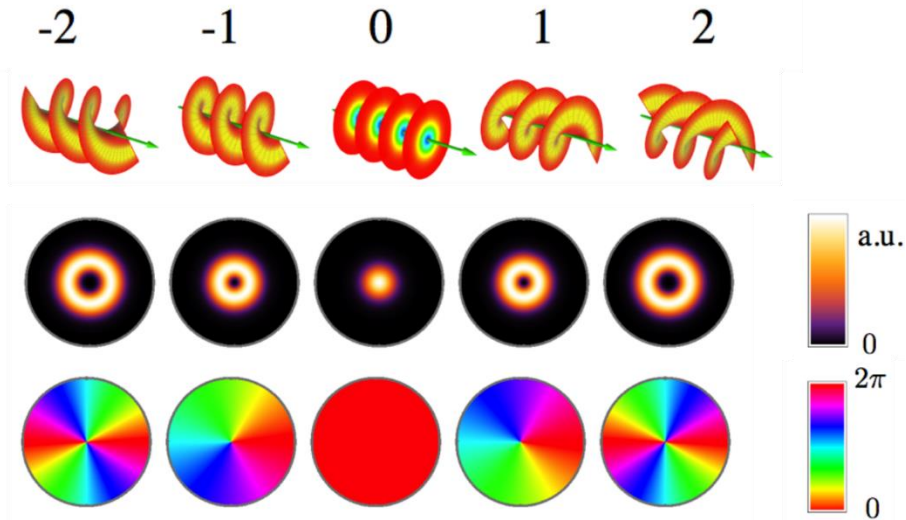


Fig. 4.10 | Representation of intensity (upper panel) and phase (lower panel) pattern of OV beam for different m values [34].

Fig. 4.11 reports some examples of SEM images of a silicon target surface after irradiation with OV beams characterized by different OAM, namely $m=1$ (panel (a)), 2 (panel (b)) and 5 (panel (c)), respectively. These enable the visualization of polarization patterns in the transverse plane by the orientation of formed surface structures. The direction of arrow represents the polarization in each case. The inset of panel (a), (b) and (c) of Fig. 4.11 represent the image of the beam after a polarizer in the beam path displaying intense region with number of lobes 2, 4 and 10 corresponding to an OV beam with $m=1$, 2 and 5, respectively. Moreover, this increase in the OAM also results in the corresponding increase in the size of the non-ablated central part. For higher m , the higher the number of the twist per λ , the faster the light is spinning around the optical axis. This usually makes the singularity larger and the correspondingly non-ablated part in the center of the crater. Panel (g) of the Fig. 4.11 depicts the variation of the outside radius of the spot, R_{out} , and the radius of the singularity inner area, R_{in} , for different m values of the beam OAM. The central non-ablated area, corresponds to the singularity of the beam that grows much faster, almost linearly, compared to the outside area of the spot, at increasing OAM values. For $m=2$ and 5 the alignment of the formed surface structures becomes more and more complex, as expected from the corresponding polarization distribution of the OV beam.

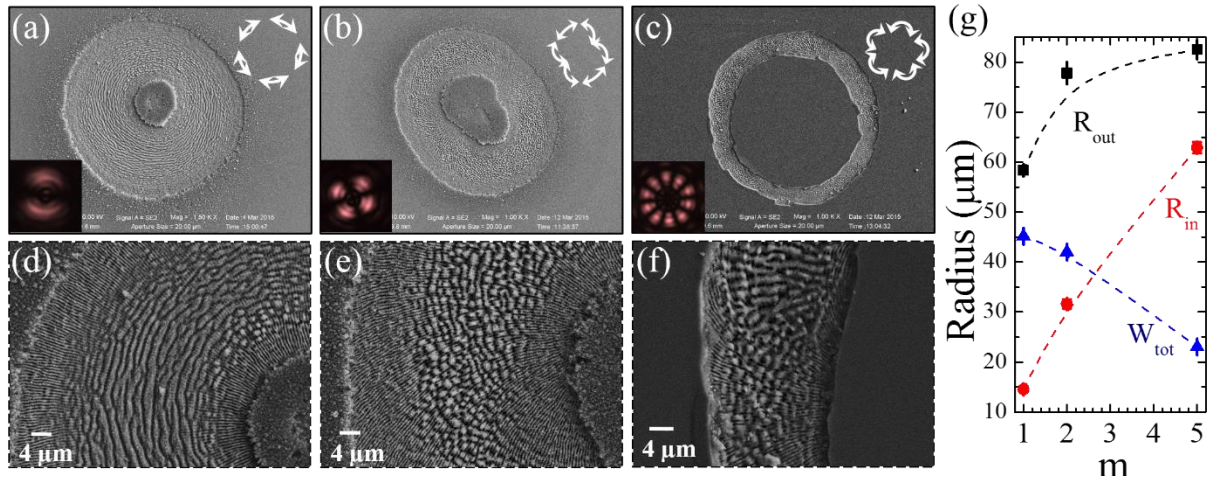


Figure 4.11/ Surface structuring of silicon by OV beam with higher OAM for $N=100$ and $E_0=30 \mu\text{J}$. Panel (a), (b) and (c) represent ablated spot generated by beam with $m=1$, 2 and 5, respectively. Zoomed view of the corresponding surface structures are provided below, labelled as panel (d), (e) and (f). Panel (g) depicts the variation of the outside radius of the crater, R_{out} , the radius of the singularity inner area, R_{in} , and the width of the ablated region, W_{tot} , as a function of the m value of the beam OAM.

In Fig. 4.11(g), the dotted line represent the total width of the ablated region, W_{tot} , where different surface features are formed on the silicon target as a consequence of irradiation. It shows a clear decrease in the width of the ablated annular region as a function of the OAM of the beam. In particular, changing the value of m from 1 to 5 leads to a corresponding reduction of almost 48% in W_{tot} . As a result, for the case of $m=5$ the surface structures are found to be confined in a narrow band with an approximate width of $W_{tot}=23 \mu\text{m}$. Lower panels (d-f) of Fig. 4.11 display zoomed views of the respective upper panels illustrating the formation of quasi-periodic surface structures (ripples and grooves) with increasing complexity as the OAM of the OV beam increases. Furthermore, as OV beams with higher OAM are used the generated pattern becomes more and more complex as the beam polarization. In particular, it is clear that ultrafast laser surface structuring opens not only efficient fabricating method for complex and fine surface structures but a simple way to characterize high power laser pulses in the focal point.

4.7 Conclusive remark

This chapter illustrated an experimental study on direct surface structuring of silicon with fs OV beams generated by means of q-plate. Experimental findings demonstrate an accurate characterization of intense fs OV beams in weak focusing conditions, as those generally exploited for direct fs laser structuring. An empirical method is used to characterize the threshold fluence

for OV by following the variation of R_{in} and R_{ex} as a function of the OV laser pulse energy. The good correspondence between the complex beam polarization and experimentally observed surface structures suggests that this approach is able not only to generate diverse surface structures but also to characterize the main physical features of the beam state through analysis of formed ripples and grooves. In particular, the surface develops a texture according to the excitation level and the local SoP. The appropriate tuning of the level of excitation allows generating complex surface structures with regular pattern of subwavelength ripples, microgrooves or mixed systems of structures by varying the fluence and number of laser pulses.

Unlike the case of very weak focusing conditions, the experimental results at medium focusing displays a bit differences in the crater morphology that are expected to be still more pronounced if the beam is tightly focused. Surface structuring with OV beam having a varying polarization from linear to circular in the same laser beam spot shows the absence of any clear ripples or grooves in the region where the polarization is near to circular.

As an extension of structuring with the basic q-plate with a topological charge $q = + 1/2$, further investigations are performed with $q = + 1$, $q = + 5/2$ indicating that OV beams with even more complex SoP can be designed and used to fabricate still more complex surface micro-structures with higher values of q . Preliminary experiments with OV beams with larger OAM confirms the validity of using the imprinted structures as a direct visualization of the polarization pattern and intensity map in the focal plane. The information gathered on the creation of the different surface structures lends itself as a powerful tool for designing specific and well-controlled periodic structures on solid targets. Moreover, since the formation of periodic surface structures seems to be ubiquitous to fs laser irradiation of solid targets, the method can be directly extended to other materials of interest as preliminary findings indicate.

References

- [1] L. Marrucci, C. Manzo, and D. Paparo, "Optical spin-to-orbital angular momentum conversion in inhomogeneous anisotropic media," *Phys. Rev. Lett.*, vol. 96, no. 16, p. 163905, 2006.
- [2] M. Duocastella and C. B. Arnold, "Bessel and annular beams for materials processing," *Laser Photon. Rev.*, vol. 6, no. 5, pp. 607–621, 2012.
- [3] E. G. Gamaly and A. V. Rode, "Physics of ultra-short laser interaction with matter: From phonon excitation to ultimate transformations," *Prog. Quantum Electron.*, vol. 37, no. 5, pp. 215–323, 2013.
- [4] Q. Zhan, "Cylindrical vector beams: from mathematical concepts to applications," *Adv. Opt. Photonics*, vol. 1, no. 1, pp. 1–57, Jan. 2009.

- [5] F. Cardano, E. Karimi, S. Slussarenko, L. Marrucci, C. de Lisio, and E. Santamato, "Polarization pattern of vector vortex beams generated by q-plates with different topological charges," *Appl. Opt.*, vol. 51, no. 10, pp. C1–C6, Apr. 2012.
- [6] F. Cardano and L. Marrucci, "Spin–orbit photonics," *Nat. Photonics*, vol. 9, no. 12, pp. 776–778, Nov. 2015.
- [7] L. Marrucci, E. Karimi, S. Slussarenko, B. Piccirillo, E. Santamato, E. Nagali, and F. Sciarrino, "Spin-to-orbital conversion of the angular momentum of light and its classical and quantum applications," *J. Opt.*, vol. 13, no. 6, p. 64001, Jun. 2011.
- [8] J. JJ Nivas, S. He, A. Rubano, A. Vecchione, D. Paparo, L. Marrucci, R. Bruzzese, and S. Amoruso, "Direct Femtosecond Laser Surface Structuring with Optical Vortex Beams Generated by a q-plate," *Sci. Rep.*, vol. 5, p. 17929, Dec. 2015.
- [9] J. Ouyang, W. Perrie, O. J. Allegre, T. Heil, Y. Jin, E. Fearon, D. Eckford, S. P. Edwardson, and G. Dearden, "Tailored optical vector fields for ultrashort-pulse laser induced complex surface plasmon structuring," *Opt. Express*, vol. 23, no. 10, pp. 12562–12572, May 2015.
- [10] K. K. Anoop, A. Rubano, R. Fittipaldi, X. Wang, D. Paparo, A. Vecchione, L. Marrucci, R. Bruzzese, and S. Amoruso, "Femtosecond laser surface structuring of silicon using optical vortex beams generated by a q-plate," *Appl. Phys. Lett.*, vol. 104, no. 24, p. 241604, Jun. 2014.
- [11] K. K. Anoop, R. Fittipaldi, A. Rubano, X. Wang, D. Paparo, A. Vecchione, L. Marrucci, R. Bruzzese, and S. Amoruso, "Direct femtosecond laser ablation of copper with an optical vortex beam," *J. Appl. Phys.*, vol. 116, no. 11, p. 113102, Sep. 2014.
- [12] O. J. Allegre, Y. Jin, W. Perrie, J. Ouyang, E. Fearon, S. P. Edwardson, and G. Dearden, "Complete wavefront and polarization control for ultrashort-pulse laser microprocessing," *Opt. Express*, vol. 21, no. 18, p. 21198, Sep. 2013.
- [13] Y. Jin, O. J. Allegre, W. Perrie, K. Abrams, J. Ouyang, E. Fearon, S. P. Edwardson, and G. Dearden, "Dynamic modulation of spatially structured polarization fields for real-time control of ultrafast laser-material interactions," *Opt. Express*, vol. 21, no. 21, p. 25333, Oct. 2013.
- [14] K. Lou, S.-X. Qian, X.-L. Wang, Y. Li, B. Gu, C. Tu, and H.-T. Wang, "Two-dimensional microstructures induced by femtosecond vector light fields on silicon," *Opt. Express*, vol. 20, no. 1, pp. 120–127, 2012.
- [15] R. Dorn, S. Quabis, and G. Leuchs, "Sharper Focus for a Radially Polarized Light Beam," *Phys. Rev. Lett.*, vol. 91, no. 23, p. 233901, Dec. 2003.
- [16] C. Hnatovsky, V. G. Shvedov, W. Krolikowski, and A. V. Rode, "Materials processing with a tightly focused femtosecond laser vortex pulse," *Opt. Lett.*, vol. 35, no. 20, p. 3417, Oct. 2010.
- [17] C. Hnatovsky, V. G. Shvedov, N. Shostka, A. V. Rode, and W. Krolikowski, "Polarization-dependent ablation of silicon using tightly focused femtosecond laser vortex pulses," *Opt. Lett.*, vol. 37, no. 2, pp. 226–228, Jan. 2012.
- [18] K. K. Anoop, A. Rubano, R. Fittipaldi, X. Wang, D. Paparo, A. Vecchione, L. Marrucci, R. Bruzzese, and S. Amoruso, "Femtosecond laser surface structuring of silicon using optical vortex beams generated by a q-plate," *Appl. Phys. Lett.*, vol. 104, no. 24, p. 241604, Jun. 2014.
- [19] K. Toyoda, K. Miyamoto, N. Aoki, R. Morita, and T. Omatsu, "Using optical vortex to control the chirality of twisted metal nanostructures," *Nano Lett.*, vol. 12, no. 7, pp. 3645–3649, 2012.
- [20] M. Meier, V. Romano, and T. Feurer, "Material processing with pulsed radially and azimuthally polarized laser radiation," *Appl. Phys. A*, vol. 86, no. 3, pp. 329–334, Jan. 2007.
- [21] J.-H. Yoo, J. Bin In, C. Zheng, I. Sakellari, R. N. Raman, M. J. Matthews, S. Elhadj, and C. P. Grigoropoulos, "Directed dewetting of amorphous silicon film by a donut-shaped laser pulse," *Nanotechnology*, vol. 26, no. 16, p. 165303, 2015.

- [22] F. Takahashi, K. Miyamoto, H. Hidai, K. Yamane, R. Morita, and T. Omatsu, “Picosecond optical vortex pulse illumination forms a monocrystalline silicon needle,” *Sci. Rep.*, vol. 6, p. 21738, Feb. 2016.
- [23] K. Lou, S.-X. Qian, X.-L. Wang, Y. Li, B. Gu, C. Tu, and H.-T. Wang, “Two-dimensional microstructures induced by femtosecond vector light fields on silicon,” *Opt. Express*, vol. 20, no. 1, p. 120, Jan. 2012.
- [24] G. D. Tsibidis, E. Skoulas, and E. Stratakis, “Ripple formation on nickel irradiated with radially polarized femtosecond beams,” *Opt. Lett.*, vol. 40, no. 22, p. 5172, Nov. 2015.
- [25] K. Lou, S.-X. Qian, Z.-C. Ren, C. Tu, Y. Li, and H.-T. Wang, “Femtosecond Laser Processing by Using Patterned Vector Optical Fields,” *Sci. Rep.*, vol. 3, pp. 1729–1731, Jul. 2013.
- [26] C. Xie, V. Jukna, C. Milián, R. Giust, I. Ouadghiri-Idrissi, T. Itina, J. M. Dudley, A. Couairon, and F. Courvoisier, “Tubular filamentation for laser material processing,” *Sci. Rep.*, vol. 5, p. 8914, Mar. 2015.
- [27] C. Hnatovsky, V. Shvedov, W. Krolikowski, and A. Rode, “Revealing Local Field Structure of Focused Ultrashort Pulses,” *Phys. Rev. Lett.*, vol. 106, no. 12, p. 123901, Mar. 2011.
- [28] K. Toyoda, F. Takahashi, S. Takizawa, Y. Tokizane, K. Miyamoto, R. Morita, and T. Omatsu, “Transfer of Light Helicity to Nanostructures,” *Phys. Rev. Lett.*, vol. 110, no. 14, p. 143603, Apr. 2013.
- [29] J. J. J. Nivas, H. Shutong, K. K. Anoop, A. Rubano, R. Fittipaldi, A. Vecchione, D. Paparo, L. Marrucci, R. Bruzzese, and S. Amoruso, “Laser ablation of silicon induced by a femtosecond optical vortex beam,” *Opt. Lett.*, vol. 40, no. 20, p. 4611, 2015.
- [30] M. J. Liu, “Simple technique for measurements of pulsed Gaussian-beam spot sizes,” *Opt. Lett.*, vol. 7, no. 5, pp. 196–198, 1982.
- [31] J. Bonse, S. Baudach, J. Krüger, W. Kautek, and M. Lenzner, “Femtosecond laser ablation of silicon—modification thresholds and morphology,” *Appl. Phys. A*, vol. 74, no. 1, pp. 19–25, Jan. 2002.
- [32] Y. Cheng, “Ultrafast laser processing: from micro-to nanoscale,” Pan Stanford Publishing, 2013.
- [33] A. D’Errico, M. Maffei, B. Piccirillo, C. de Lisio, F. Cardano, and L. Marrucci, “Topological features of vector vortex beams perturbed with uniformly polarized light,” *Sci. Rep.*, vol. 7, p. 40195, Jan. 2017.
- [34] F. Cardano, “Engineering spin and orbital angular momentum interactions in a light beam: quantum and classical applications,” *Universitá degli Studi di Napoli Federico II*, 2015.

Surface structuring with generalized vector beams

“This chapter addresses an experimental investigation on direct femtosecond laser surface structuring with a higher class of vector beams generated by electrically tuning the optical retardation of a q-plate with $q=+1/2$. This allows generating a family of ultrashort laser beams with a continuous spatial evolution of polarization and fluence distribution in the focal plane by controlled coherent superposition of a uniformly polarized Gaussian beam with a vortex beam. The use of this generalized vector beam with ultrashort pulse duration in laser structuring can considerably improve the possibility of achieving a number of asymmetric surface patterns.”

5.1 Introduction

In recent years, ultrashort laser beams are constantly showing impressive scientific achievements in the fabrication of a plurality of surface structures, including e.g. LIPSS, cones arrays, random patterns, and so forth [1]–[4]. The practice of cylindrical vector beams with fs pulse duration has been proved as a remarkable laser surface fabrication method for the generation of surface patterns with axial symmetry. The easiness in tuning the SoP of OV beams generated by a q-plate enabled to access the numerous spatially variant surface structures with a single step process. Moreover, the direct relationship of surface structures orientation and morphological features with laser light polarization and fluence has also been demonstrated as an effective, direct way for the characterization of intense optical vector beams and are discussed in the previous Chapters [5]. In this chapter, we deal with direct fs laser surface structuring induced by a higher class of vector beams generated by a q-plate, going beyond standard radially and azimuthally polarized vector beams. These beams are obtained by varying the birefringence optical retardation δ of the optical device [6], which allows generating a family of ultrashort laser beams with a continuous spatial evolution of polarization and fluence distribution in the focal plane. The previous chapter discussed the experiments at optimal tuning, corresponding to a half-wave retardation ($\delta = \pi$) of the q-plate, that allows generating OV beams carrying a definite OAM through spin-to-orbital conversion of the angular momentum of light. Tuned q-plate ($\delta = \pi$) shined with linearly

polarized Gaussian beams indeed generates cylindrically symmetric vortex beams (e.g. radial, azimuthal, spiral, etc.). By detuning the q-plate, that is varying δ with respect to its optimal value, a variety of fs laser beams with an asymmetric spatial distribution of intensity and SoP in the focal plane can be generated, which in turn allow achieving lop-sided surface patterns on a silicon target. Here we exploit a q-plate with $q=+1/2$ for monitoring the beam generated during off tuning conditions. The various features of the surface patterns and the vector beams characteristics at the focal plane are contrasted, thus demonstrating how the spatial variation of the local state of the laser beam offers an effective way to both design unconventional, asymmetric surface structures and characterize complex ultrashort laser beams. In addition, the SoP of generated laser beams are optically characterized by evaluating the Stokes parameters before the focusing lens.

The laser source is a Ti:Sa laser system delivering ≈ 35 fs pulses at a central wavelength of 800 nm with a Gaussian beam spatial profile, at a repetition rate of 100 Hz. The detailed experimental setup can be found in Chapter 2. The q-plate is tuned at various optical retardation δ by means of the driving voltage V_{pp} (peak to peak) applied to the q-plate applying a square-wave at 11 kHz delivered by a signal generator.

5.2 Generation of asymmetric beam by q-plate

As mentioned earlier, the main element of our beam-shaping method is the q-plate, a device based on liquid crystal technology [7], [8] that is commonly used for generating light beams carrying OAM [9]. The q-plate essentially works as a birefringent wave plate characterized by an inhomogeneous distribution pattern of the local optic axis in the transverse plane and defined by a semi-integer topological charge q . Besides the topological charge, the action of the q-plate is determined by the value of the birefringent optical retardation δ , which is controlled electrically by applying an external voltage to the plate [10]. In particular, when acting on a horizontal (vertical) linearly polarized Gaussian beam, the output state is given by:

$$\psi = \text{Cos}\left(\frac{\delta}{2}\right) G_{H/V} + i \text{Sin}\left(\frac{\delta}{2}\right) OV_{rad/az}, \quad (1)$$

where $G_{H/V}$ stands for the input Gaussian beam with uniform Horizontal or Vertical SoP, respectively, and $OV_{rad/az}$ is an optical vortex (OV) beam with radial or azimuthal SoP. As

shown in Eq. (1), the q-plate acts as a transparent medium in the de-tuned condition $\delta=2\pi$, leaving unchanged the initial Gaussian beam. At the optimal tuning, $\delta=\pi$, it yields standard OV beams carrying an OAM $m=\pm 1$ [9]. After the q-plate, these OV beams present a spatial intensity distribution characterized by a central region of zero intensity, a principal intense annulus and several secondary rings at increasing radial distance from the axis [8], [11]. The central part of these beams is spatially filtered with an iris, thus obtaining OV beams with an annular spatial profile. The SoP of these OV beams is varied by appropriate tuning of the polarization of the input Gaussian beam [9], [12]. Fig. 5.1 reports a schematic of the configurations generating OV beams with radial SoP at optimal q-plate tuning ($\delta=\pi$, panel (c)) and with linear SoP for an un-tuned q-plate ($\delta=2\pi$, panel (a)). The spatial profiles of the SoP in the near-field after the q-plate obtained by optical tomography are illustrated in the corresponding lower panels. In these cases, the Gaussian and OV beams present a cylindrically symmetric distribution of the SoP and intensity with respect to the optic axis. This, in turn, is reproduced in the surface patterns generated on the target surface by direct fs laser structuring as will be illustrated later.

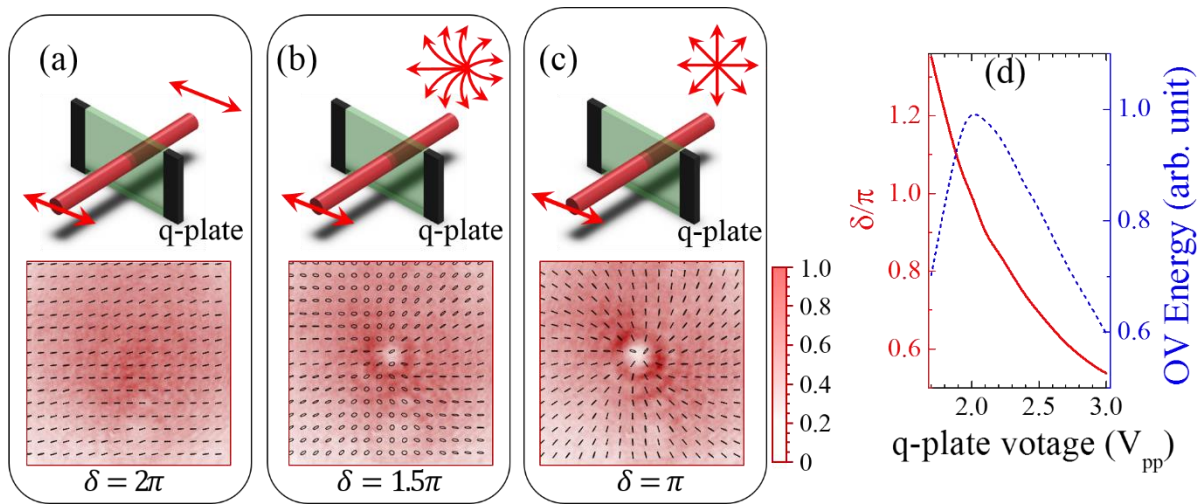


Figure 5.1| Schematic representation of q-plate setup in the case of voltage tuning for various optical retardation δ . (a) $\delta=2\pi$ leads to a linearly polarized Gaussian beam at the output of the q-plate ; (b) $\delta=1.5\pi$ shows an example of q-plate tuning condition leading to the generation of a generalized vector beam with an asymmetrical distribution of SoP. (c) $\delta=\pi$ corresponds to the q-plate tuning condition leading to the generation of optical vortex beams. The lower panel (a) to (c) represent the corresponding polarization pattern obtained by optical tomography in near field. The red arrows schematically represents the SoP of input and output at the q-plate. The lower images shows the examples of the spatial profile of the converted beams. The graph provided in panel (d) displays the optical retardation δ (in red) and energy of the OV beam (in blue) corresponding to the different tuning voltages of the q-plate.

As shown in Eq. (1), the q-plate however offers another degree of freedom. When driven by a voltage different from those leading to the tuned ($\delta=\pi$), and un-tuned ($\delta=2\pi$) conditions illustrated above, the beam generated by the q-plate is a coherent superposition of two fundamental optical states, the Gaussian and OV beams, with relative contributions that vary as the optical retardation changes [6]. An example is schematically shown in the Fig. 5.1(b). This, in turn, leads to a class of fs laser beams characterized by an inhomogeneous and asymmetric distribution of polarization and fluence, of which Gaussian and OV beams are the two limiting cases. Panel (d) of Fig. 5.1 shows the plot of δ and energy of OV beam as a function of the voltage applied to the q-plate.

Partial tuning of the q-plate allows generating light beams, here indicated as fs generalized vector beams, for which only a partial conversion to an OV state is achieved. Therefore, these beams can be described as a superposition of an OV and a Gaussian beam (see Eq. (1)), with a variable fraction of these two components [13]. When focused with a low numerical aperture (NA) lens, as in our experimental conditions, these two components become spatially shifted in the focal plane. This, in turn, allows generating lopsided, fs laser beams with a rather complex spatial variation of the SoP and fluence distribution as reported in Fig. 5.1(b). Direct fs laser surface structuring is performed by focusing these generalized vector beams with a low NA lens on a silicon target. Formed surface structures are compared with the simulated polarization and intensity distributions at the lens focal plane of the field reported in Eq. (1). This indeed can be computed at any propagation distance if considering the complete expression of OV beams generated by a q-plate. Further details regarding the theoretical and experimental analyses of these kind of beams can be found in Ref. [6].

5.3 Surface structuring with beams generated by tuning the q-plate optical retardation

The surface patterns generated in the two limiting cases of un-tuned and tuned q-plate corresponding to the Gaussian (G) and OV components of the generalized vector beams for a fixed value of the total pulse energy ($E_0=45 \mu\text{J}$) are shown in Fig. 5.2 (a) and (b) respectively. In particular, Fig. 5.2 report examples of SEM images of the target surface after an irradiation sequence of $N=200$ laser pulses. In Fig. 5.2 the upper panels (a & b) illustrates the different size and morphology of the craters formed on the silicon target, while the lower ones (c & d) show

zoomed views registered with the IL detector evidencing more details of the surface structures. Moreover, panel (e) reports the spatial distribution of the laser pulse fluence F as a function of the radial coordinate, r , which is well described by the expressions [5], [14]:

$$F_G(r) = \frac{2E_0}{\pi w_0^2} \exp\left(-\frac{2r^2}{w_0^2}\right) \quad (2)$$

$$F_{OV}(r) = \frac{2^2 E_0}{\pi w_0^4} r^2 \exp\left(-\frac{2r^2}{w_0^2}\right) \quad (3)$$

for the G and the OV beams with OAM= ± 1 , respectively, where w_0 is the waist of the fundamental Gaussian beam. In our experimental conditions, the beam waist w_0 is found to be $\approx 35 \mu\text{m}$.

In a recent report, we also compared the same two cases for a fixed value of the peak fluence, and found that surface structures locally produced at the same fluence level and number of pulses are characterized by rather similar morphological features [15]. However, hereafter we report an analysis carried out at a fixed energy, as opposed to a fixed peak-fluence level. The fluence profile of the un-tuned case ($\delta = 2\pi$) corresponding to the Gaussian beam and described by Eq. (2) is illustrated in Fig. 5.2(e). The OV beams generated in the tuned case ($\delta = \pi$) are characterized by an annular spatial profile with a central region of zero intensity due to an undefined phase on the OV beam axis, as described by Eq. (3) and illustrated in Fig. 5.2(e). At the same energy E_0 , the laser fluence of the two beams shows rather different spatial profiles and also different values of the peak fluence. In the present case, for a the pulse energy is $E_0=45 \mu\text{J}$, the Gaussian beam has a peak fluence $F_{G,peak} = 2E_0/\pi w_0^2 \approx 2.3 \text{ J/cm}^2$ at the beam centre ($r=0$). Instead, the OV beam has a null fluence at the centre ($r=0$), and the peak fluence occurs at the radial position $r_{OV,peak} = w_0/\sqrt{2}$. The corresponding maximum value of the OV beam fluence is $F_{OV,peak} = e^{-1} \times F_{G,peak} \approx 0.37 F_{G,peak}$, hence $F_{OV,peak} \approx 0.85 \text{ J/cm}^2$. This leads to the rather different characteristics observed for G and OV beams in the SEM images of Fig. 5.2, since the size of the ablation crater and the morphology of the surface structures critically depend on the local value of the laser fluence [3], [4], [16], [17].

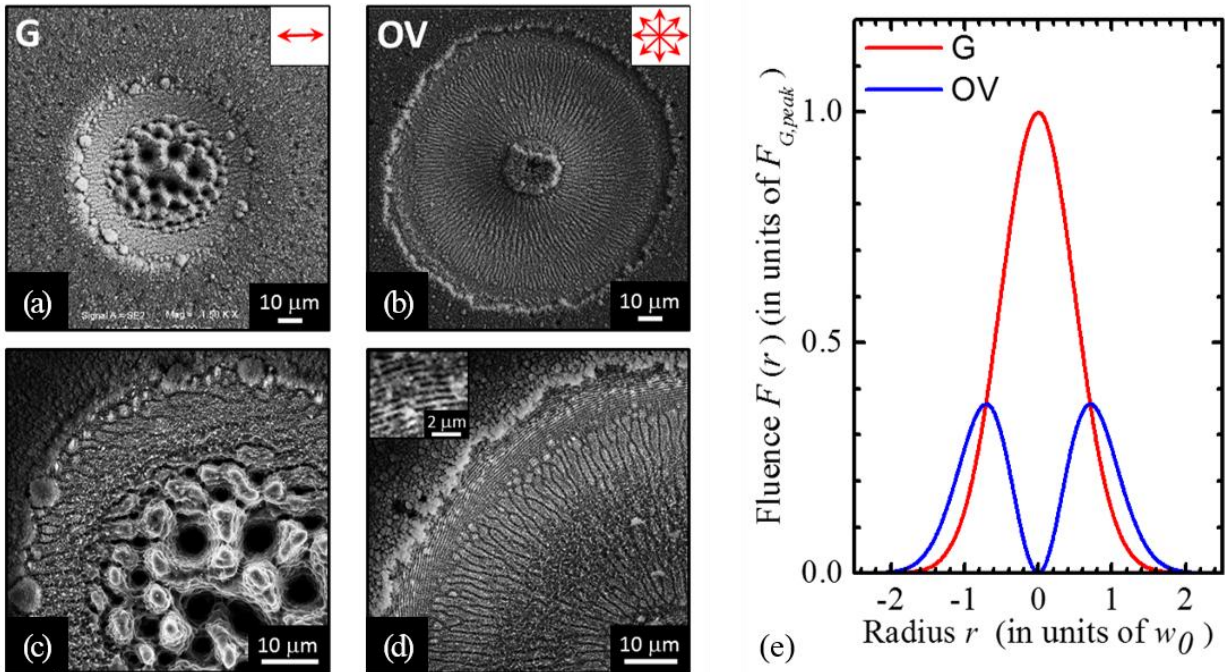


Figure 5.2| Panels (a) and (b) are examples of SEM images acquired with the SE detector showing the surface morphologies developed on the silicon target after an irradiation sequence of $N=200$ pulses at a pulse energy $E_0=45 \mu\text{J}$ for the (a) Gaussian beam with equivalent peak fluence $F_p=2.3 \text{ J/cm}^2$ (un-tuned q -plate at $\delta = 2\pi$) and the (b) OV beam corresponds to a peak fluence $F_p=0.85 \text{ J/cm}^2$ (tuned q -plate at $\delta = \pi$, radial SoP). Panels (c) and (d) are SEM images acquired at higher magnification with the IL detector illustrating the finer details of the surface texture for the two cases. The inset in panels (d) shows a zoomed view of the ripples generated in the peripheral, annular regions at lower fluence of the OV beams. Panel (e) shows the spatial profile of the laser fluence $F(r)$ as a function of the radius r along the diameter of the beam (in units of the beam waist w_0) for the Gaussian (G) and OV beam with the same pulse energy. The profiles are normalized to the peak fluence of the Gaussian beam $F_{G,peak}$.

The G beam produces a smaller crater with an external radius of $\approx 37 \mu\text{m}$, while OV beams generate larger annular craters characterized by internal and external radii of $\approx 10 \mu\text{m}$ and $\approx 60 \mu\text{m}$, respectively. Moreover, Fig. 5.2(a) and (c) show that, at the high peak fluence achieved with the Gaussian beam, the crater is characterized by grooves in the external region (for $r > 25 \mu\text{m}$), while the central region at higher fluence is characterized by coarser micro-wrinkles decorated with several columnar structures and deep cavities, whose typical size is in the range $3\text{--}5 \mu\text{m}$. This kind of surface structures typically forms in high laser fluence regions or after large number of pulses. In fact, craters produced by reducing the laser peak fluence shows a progressive reduction of the central area characterized by coarser wrinkles followed by an annular grooved region eventually surrounded by an external rippled area.

Similarly to what has been discussed in the previous chapter, in the case of OV beam, the central region ($r < 10 \mu\text{m}$) is characterized by an unprocessed area decorated with nanoparticles. The ablated crater shows an inner region with a width of $\approx 30 \mu\text{m}$ characterized by grooves aligned along the beam polarization. Besides, in the higher fluence region around the OV beam peak ($20 \mu\text{m} < r < 30 \mu\text{m}$), these grooves are partially smashed, suggesting that irradiation at larger fluence with a high number of shots can be responsible of a progressive modification of the grooves morphology as well as of the columnar structures observed in the case of the G beam. According to the spatial profiles of the fluence, columnar structures mainly form at fluence values larger than $\approx 0.9 \text{ J/cm}^2$ (for $N=200$), therefore they are not recognizable in the craters generated by the OV beam due to its lower peak fluence. At the lower fluence values attained in the external periphery of the OV beam (e.g. for $10 \mu\text{m} < r < 13 \mu\text{m}$ and $48 \mu\text{m} < r < 60 \mu\text{m}$), subwavelength ripples are formed in two annular regions surrounding the grooved area.

5.3.1 Patterning with generalized vector beams produced using the q-plate

We turn now to the case of the generalized vector beams obtained for intermediate tuning and to the main characteristics of the crater shape and surface patterns they produce on the silicon target. Several fs vector beams are generated by varying the optical retardation of the q-plate, δ . The theoretical spatial profiles of the laser fluence and SoP in the focal plane are obtained by simulating the optical field propagation, as described in Ref. [6].

Fig. 5.3 illustrates the variation of the beam characteristics by reporting examples of intensity and SoP spatial profiles at various values of δ . In particular, for each value of δ , the central panel reports a two-dimensional map that shows the SoP (ellipses) and the fluence (intensity, in false colour) spatial distributions of the laser beam. It is worth noting that the polarization ellipses defining the SoP in each location of the beam are very narrow, that is the SoP is approximately linear, and well approximated by a segment whose orientation indicates the dominant local component of the polarization. Moreover, the upper panel shows the one-dimensional profile of the fluence spatial distribution along the horizontal axis passing through the beam centre.

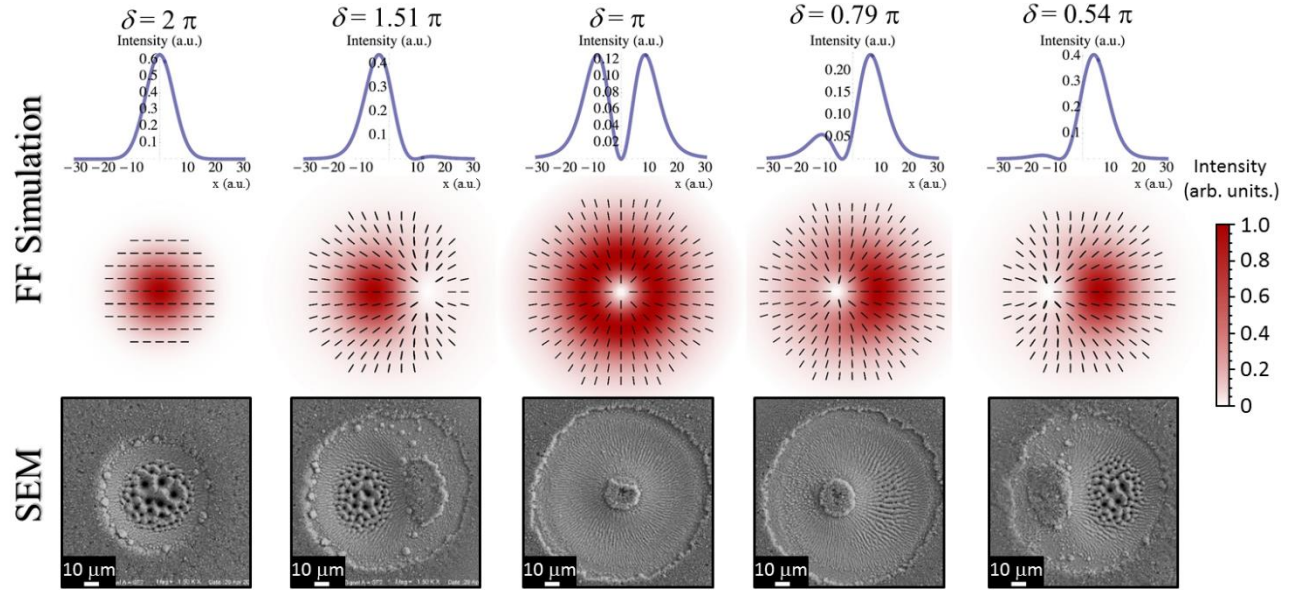


Figure 5.3/ The central panels show the spatial profiles, in the focal plane, of both the fluence and the SoP of various vector beams generated by changing the value of the q -plate optical retardation δ . The experimental configuration corresponds to that leading to a radially polarized OV beam at optimal tuning of the q -plate optical retardation $\delta = \pi$. For each panels, the fluence is normalized to its own maximum value according to the false color scale reported on the right. Moreover, the polarization ellipses defining the SoP in each location of the generalized vector beams are very narrow, i.e. the local polarization is approximately linear and well approximated by a segment indicating the orientation of its dominant component. The upper panels report the corresponding one-dimensional fluence profiles along the horizontal diameter. The lower panels show SEM images of the corresponding craters produced on the silicon target surface after an irradiation sequence of $N=200$ pulses at a pulse energy $E_0=45 \mu\text{J}$, registered with the SE detector.

As anticipated, in the focal plane the fs vector beam is described as a superposition of two fundamental components: the OV and G beams corresponding to the tuned and un-tuned q -plate discussed above. This property is clearly addressed by the maps reported in the central panels of Fig. 5.3. In particular, the optical retardation tuning produces a change of the relative contributions and a spatial separation of the two components with a shift of the position of the region of minimum fluence of the beam along the q -plate axis, which in Fig. 5.3 is horizontal. Finally, the lower panels of Fig. 5.3 show SEM images of the silicon target surface after an irradiation sequence of $N=200$ pulses at a laser energy $E_0=45 \mu\text{J}$.

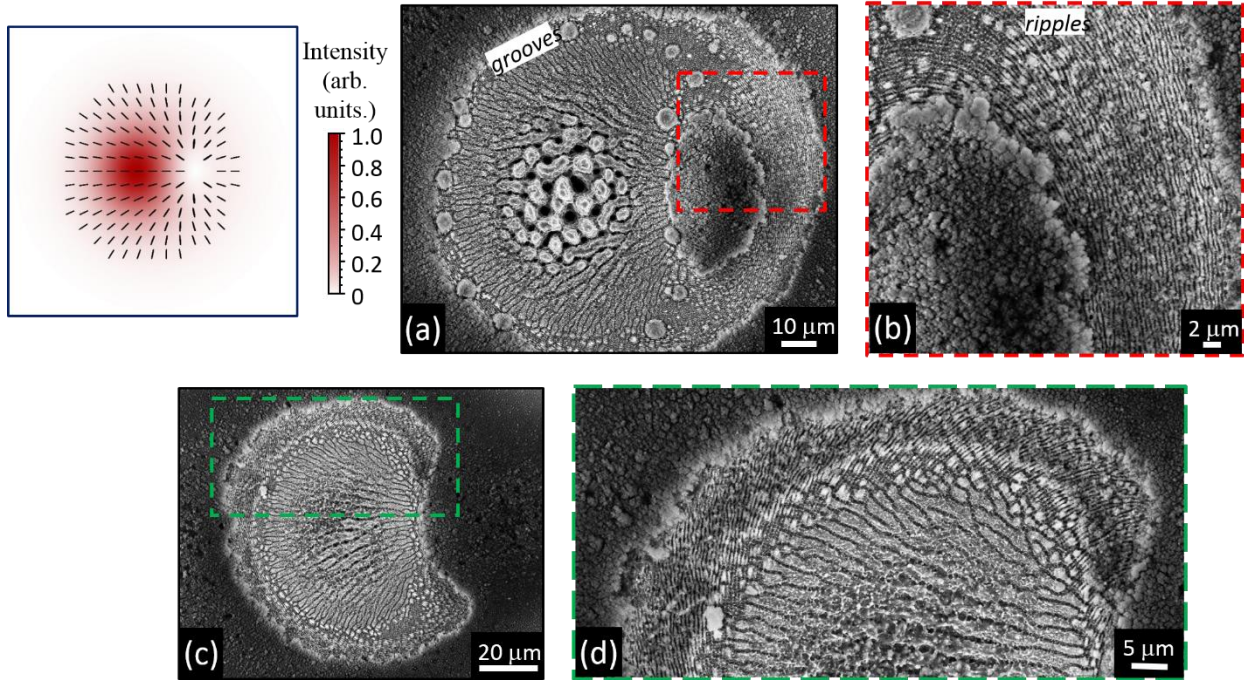


Figure 5.4| (a) SEM image, acquired with the IL detector, illustrating the surface morphology developed on the silicon target after an irradiation sequence of $N=200$ pulses at a pulse energy $E_0=45 \mu\text{J}$, for the radial vector beam generated at $\delta = 1.51 \pi$. (b) Zoomed view of the area indicated by the red dashed box in panel (a). (c) SEM image, acquired with the IL detector, illustrating the surface morphology developed on the silicon target after an irradiation sequence of $N=200$ pulses at a pulse energy $E_0=27 \mu\text{J}$ at $\delta = 1.51 \pi$. (d) Zoomed view of the area indicated by the green dashed box in panel (c). Upper-left inset: map of the SoP and fluence of the radial fs-PSB generated at $\delta=1.51 \pi$.

Besides a perfectly G beam with uniform horizontal polarization at $\delta = 2\pi$ and the radially polarized OV beam at $\delta = \pi$, a variety of fs vector beams with a prevalent radial SoP can be generated, which we indicate as radial vector beams. The examples in Fig. 5.3 show two cases of radial fs vector beams with the region of minimum fluence located off-axis at the two opposite sides with respect to the beam centre for $\delta = 1.51 \pi$ and $\delta = 0.54 \pi$, respectively. Moreover, radial vector beams characterized by a small shift of the position of the region of minimum fluence and a slight asymmetric distribution of the fluence and SoP are also achieved, as e.g. at $\delta = 0.79 \pi$. The SEM images of Fig. 5.3 demonstrate that the shapes of the ablation craters closely reflect the variation of the fluence spatial distribution of the various fs vector beams. Voltage tuning also influences the SoP of the fs vector beam allowing to create optical states with an asymmetric spatial distribution of the polarization direction for values of δ different from π and 2π . The corresponding effect on the surface structures is illustrated in Fig. 5.4(a) and (b), which report SEM images of the crater produced at $\delta = 1.51 \pi$ and registered with the IL detector. In particular, Fig. 5.4(b) is a zoomed view of a part of the crater, close to the region of minimum fluence that better evidences the spatial arrangement of

the surface ripples. In Fig. 5.4(a) one can easily appreciate the fairly good correspondence between the surface structures and the fs vector beam map, reported in the upper-left inset for easiness of comparison. In particular, the SEM image shows an area characterized by columnar structures and coarse micro-wrinkles located in the higher fluence region of the beam which is surrounded by grooves directed along beam polarization over intermediate region of fluence. Opposite to the high intensity area, an elliptically shaped, nearly unprocessed area decorated with nanoparticles is formed in the part corresponding to the lower intensity region of the beam [18]. This area is slightly elongated in the vertical direction resembling the asymmetric shape of the region of minimum fluence present in the corresponding radial vector beam map (Fig. 5.4, inset). Around this region, a rippled zone corresponding to rather low fluence values is recognized in the zoomed view of Fig. 5.4(b).

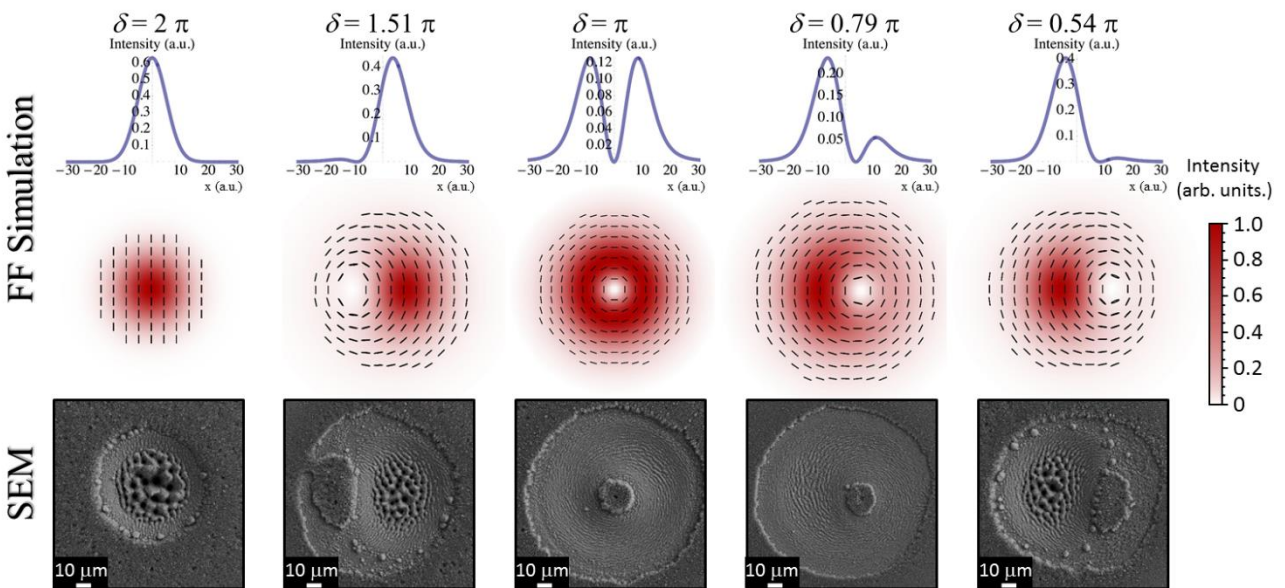


Figure 5.5 | The central panels show the spatial profiles, in the focal plane, of both the fluence and the SoP of various vector beams generated by changing the value of the q -plate optical retardation δ . The experimental configuration corresponds to that leading to an azimuthally polarized OV beam at optimal tuning of the q -plate optical retardation $\delta = \pi$. For each panels, the fluence is normalized to its own maximum value according the false color scale reported on the right. The upper panels report the corresponding one-dimensional fluence profiles along the horizontal diameter. The lower panels show SEM images of the corresponding craters produced on the silicon target surface after an irradiation sequence of $N=200$ pulses at a pulse energy $E_0=45 \mu\text{J}$, registered with the SE detector.

Fig. 5.4(c) addresses the variation of the crater shape when the energy of the radial fs vector beam ($\delta = 1.51 \pi$) is reduced to $E_0=27 \mu\text{J}$. Due to the lopsided distribution of the laser intensity, bow-shaped craters are generated on the target surface. The example reported in Fig. 5.4(c) resembles the figure of a half-moon. A zoomed view of a portion of this crater is reported in Fig. 5.4(d) to evidence the arrangement of the various

surface structures: ripples, well-developed grooves and smashed grooves progressively appear going from the crater edges, at lower fluence, towards the more intense part of the beam. Craters with a shape nearly specular with respect to the vertical to the one of Fig. 5.4(c) are obtained when tuning the voltage to a value close to $\delta = 0.54 \pi$ (not shown) as a consequence of both the redistribution of the laser intensity and the shift of the position of the region of minimum fluence (see Fig. 5.3).

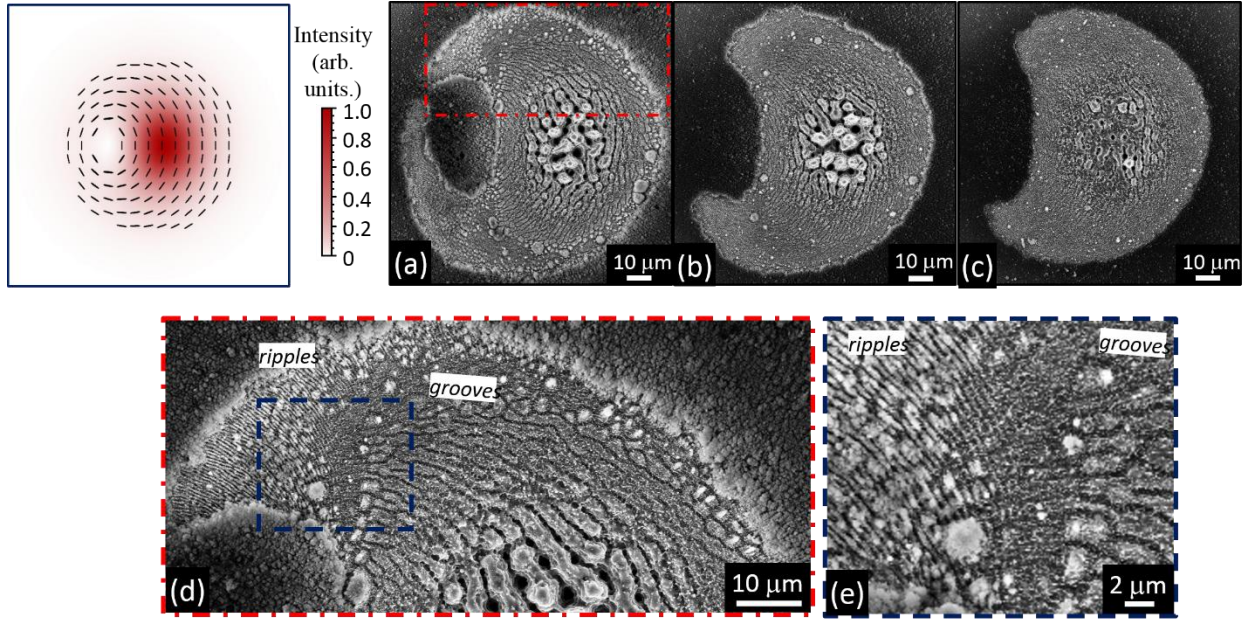


Figure 5.6| SEM images, acquired with the IL detector, illustrating the surface morphology developed on the silicon target after irradiation sequences of (a) $N=200$, (b) $N=100$ and (c) $N=50$ pulses, respectively, at a pulse energy $E_0=45 \mu\text{J}$, for the azimuthal fs vector beam generated at $\delta = 1.51 \pi$. (d) Zoomed view of the area indicated by the red dashed box in panel (a). (e) Zoomed view of the area indicated by the blue dashed box in panel (d). Upper-left inset: map of the SoP and fluence of the azimuthal fs vector beam generated at $\delta = 1.51 \pi$.

We turn now to the case of an OV beam with an azimuthal SoP at optimal tuning of the q-plate ($\delta = \pi$). Likewise the previous case, we name the generated singular beams as azimuthal fs vector beams. Fig. 5.5 reports examples of the beam properties generated by varying the value of δ . At $\delta = 2\pi$, a perfect G beam with uniform vertical polarization is produced. Then, several asymmetric, azimuthal vector beams like the one shown in Fig. 5.5 for $\delta = 1.51 \pi$ are progressively generated reducing the values of δ finally approaching the perfect azimuthally polarized OV beam at $\delta = \pi$. As δ is further decreased, other azimuthal fs vector beams are obtained with a continuous rightward shift of the region of minimum fluence. Interestingly, the azimuthal fs vector beams show a displacement of the region of minimum fluence in a reverse direction with respect to radial fs vector

beams as a function of the q-plate optical retardation (see Fig. 5.3 and 5.5). Moreover, the fluence spatial profiles of the azimuthal and radial fs vector beams, at the same value of δ , are specular with respect to the vertical line passing through the location of the G or OV beams centers.

Also for azimuthal vector beams, the SEM images of the target surface reported in the lower panels of Fig. 5.5 show SEM images of the silicon target surface after an irradiation sequence of $N=200$ pulses at a laser energy $E_0=45 \mu\text{J}$. Panels (a)-(c) of Fig. 5.5 address the change of the crater shape as a function of the number of pulse N for an azimuthal fs vector beam ($\delta=1.51 \pi$) at an energy $E_0=45 \mu\text{J}$. The progressive reduction of N leads to the gradual formation of half-moon shaped craters as a consequence of the asymmetric distribution of the laser fluence. Moreover, the various surface structures become vaguer and less defined for lower number of pulses. Figs. 5.6(d) and (e) report SEM images acquired at higher magnification of portions of the crater shown in Fig. 5.6(a) addressing the arrangement of the various surface structures produced by azimuthal fs vector beams. The surface structures display a good correlation with the fs vector beam map shown in the upper-left inset of Fig. 5.6 to facilitate the comparison. The region corresponding to the more intense part of the beam presents the characteristic coarser wrinkles decorated by columnar structures. This region is enclosed by an array of well-defined grooves displaying a preferential azimuthal orientation in the areas of the fs vector beam at intermediate values of the fluence, eventually verging towards the elliptically shaped, nearly unprocessed area decorated with nanoparticles located in the sector corresponding to the region of minimum fluence of the laser beam. Finally, ripples covering the low intensity part of the beam is shown in Fig. 5.6(e).

The result illustrated above show how the use of ultrashort laser beams with inhomogeneous spatial distribution of the polarization can be an extraordinary way to handle very complex and rich structural surface patterns with relatively few control parameters (N, E_0, δ). This control can be achieved remotely and programmatically, thus opening the route to fabricate more complex surface structures by direct fs laser surface structuring.

In all cases, a rather good correspondence between the state of the optical beam and the experimentally observed surface structure is observed. In an attempt to underline such reliable consistency, we decide to carry out a more quantitative comparison, as reported in Fig. 5.7. In the figure, the solid dots represent experimental data points obtained by estimating the central position (panel (a)) and the area (panel (b)) of the nearly unprocessed region decorated with nanoparticles

that identifies the region of minimum fluence in the crater produced on the target surface, meanwhile the corresponding values for the beam obtained from the calculation are reported as solid lines. Simulation results are obtained by measuring the shift of low intensity part corresponding to the central singularity (in the case of tuned OV beam) from the far-field simulation of intensity profile of beam generated by varying the optical retardation of q-plate as explained in [6]. Since the removal of material in the ablation process is a threshold phenomenon, the area of the region of minimum fluence of the beam is derived from the map of the fluence spatial profile by fixing an appropriate fraction of the peak fluence coherent with the experimental case. Moreover, the variation of the central position of the region of minimum fluence corresponds to the shift of the location of the minimum of the beam fluence spatial profile. The data in Fig. 5.7(a) are normalized to the maximum value achieved by the shift of the region of minimum fluence position corresponding to $\delta=0.54 \pi$, while in Fig. 5.7(b) the area of the region of minimum fluence is normalized to the minimum value achieved at optimal tuning ($\delta= \pi$). Due to the symmetric behavior with respect to the optimal tuning condition, the data are only reported for $\delta \leq \pi$. Moreover, data for values lower than $\delta=0.54 \pi$ are not considered because the region of minimum fluence shifts in areas of very low fluence which makes it not possible for identifying the corresponding area in the crater generated on the target surface (see e.g. Fig. 5.4 (c)). Fig. 5.7 shows that the simulation results reproduce fairly well the observed experimental trend, thus indicating that the predicted features of the fs vector beams are very consistent with the main characteristics of the craters formed on the silicon target. In addition, the accurate matching between the directional arrangements and spatial distribution of the produced surface structures and the SoP and fluence distribution of the fs vector beams further confirms that analysis of ablation craters and surface structures can be effectively used as a profiling method to diagnose intense and complex ultrashort laser beams.

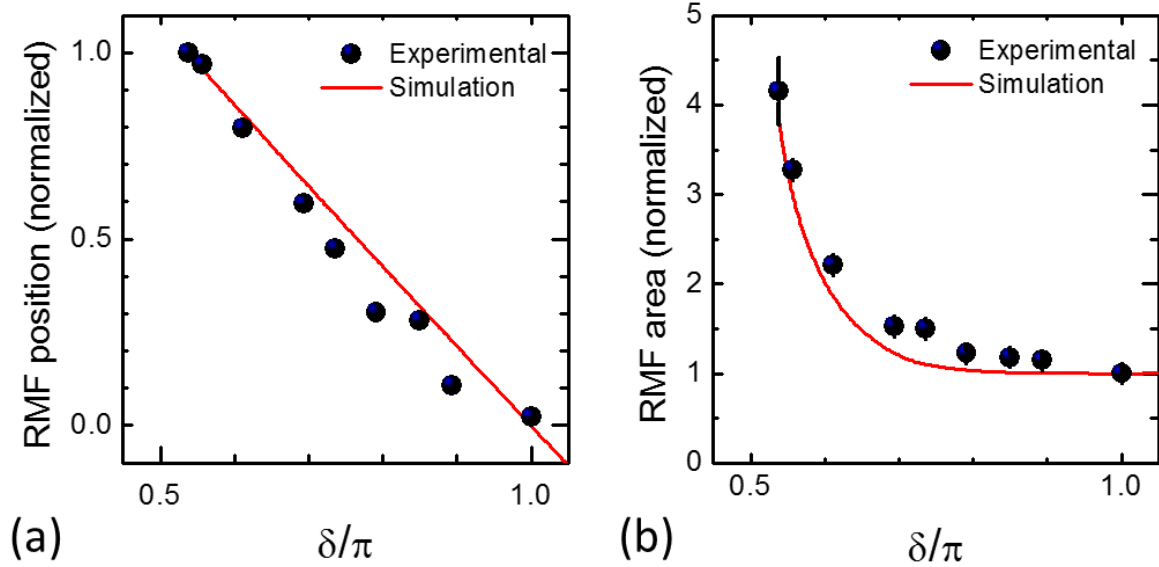


Figure 5.7/ Variation of the central position (a) and area (b) of the region of minimum fluence (RMF) as a function of the optical retardation δ . The experimental values of the region of minimum fluence correspond to the central position and area of the nearly unprocessed area decorated with nanoparticles present in the crater produced on the target surface. The corresponding simulation values represent the location of the minimum beam fluence and the area of a region of the beam delimited by fixing an appropriate fraction of the peak fluence coherent with the experimental value of the ablation fluence threshold. In panel (a), the error bars are contained within the data point symbols.

5.4 Conclusive remark

In this last chapter we have demonstrated that a beam converter based on a q-plate can be effectively exploited to generate fs generalized vector beams and experimentally investigated, for the first time, the application of these optical beams to direct surface structuring of silicon. Our findings single out the possibility of using the voltage tuning of the q-plate beam converter to vary its optical retardation δ , thus generating several complex surface structures decorated with patterns of ripples, grooves or more complex forms directly associated to the local state of the optical vector beam. Moreover, the direct association between the various features of the observed surface structures and the local state of the fs vector beam suggests that direct analysis of ablation craters can be a valuable way to diagnose complex ultrashort laser beams. Our results evidence that an appropriate tuning of the level of excitation achieved through a suitable selection of the energy and number of laser pulses can lead to the elaboration of asymmetric shaped craters and lopsided distributions of the surface structure. While our investigation was limited to fs vector beams generated with a q-plate with a topological charge $q=+1/2$ in two specific configurations (i.e. radial and azimuthal OV beams at optimal q-plate tuning), other experimental arrangements of the q-plate beam converter,

as for example higher values of q or OV beams with even more complex SoP at optimal tuning, can be designed and used to fabricate still more complex surface micro-structures. Since the formation of surface structures seems to be ubiquitous to laser irradiation of solid targets with ultrashort pulses, the method we describe can be directly extended to other materials of interest. Finally, the possibility of fast switching intrinsic to a voltage tuning of the state of the q-plate can be joined to switchable wave-plates, as e.g. electronic controlled liquid crystal retarders, allowing the implementation of a setup based on high-speed generation and tuning of fs vector beams for an efficient fabrication of complex arrays of surface structures based on direct fs laser processing of solid targets.

References

- [1] K. C. Phillips, H. H. Gandhi, E. Mazur, and S. K. Sundaram, "Ultrafast laser processing of materials: a review," *Adv. Opt. Photonics*, vol. 7, no. 4, p. 684, Dec. 2015.
- [2] K. Sugioka and Y. Cheng, "Ultrafast lasers—reliable tools for advanced materials processing," *Light Sci. Appl.*, vol. 3, no. 4, p. e149, Apr. 2014.
- [3] A. Y. Vorobyev and C. Guo, "Direct femtosecond laser surface nano/microstructuring and its applications," *Laser Photon. Rev.*, vol. 7, no. 3, pp. 385–407, May 2013.
- [4] T. H. Her, "Femtosecond-Laser-Induced Periodic Self-Organized Nanostructures," *Compr. Nanosci. Technol.*, vol. 4, pp. 277–314, 2011.
- [5] J. J. J. Nivas, H. Shutong, K. K. Anoop, A. Rubano, R. Fittipaldi, A. Vecchione, D. Paparo, L. Marrucci, R. Bruzzese, and S. Amoruso, "Laser ablation of silicon induced by a femtosecond optical vortex beam," *Opt. Lett.*, vol. 40, no. 20, p. 4611, 2015.
- [6] A. D'Errico, M. Maffei, B. Piccirillo, C. de Lisio, F. Cardano, and L. Marrucci, "Topological features of vector vortex beams perturbed with uniformly polarized light," *Sci. Rep.*, vol. 7, p. 40195, Jan. 2017.
- [7] L. Marrucci, C. Manzo, and D. Paparo, "Optical spin-to-orbital angular momentum conversion in inhomogeneous anisotropic media," *Phys. Rev. Lett.*, vol. 96, no. 16, p. 163905, 2006.
- [8] L. Marrucci, E. Karimi, S. Slussarenko, B. Piccirillo, E. Santamato, E. Nagali, and F. Sciarrino, "Spin-to-orbital conversion of the angular momentum of light and its classical and quantum applications," *J. Opt.*, vol. 13, no. 6, p. 64001, Jun. 2011.
- [9] F. Cardano, E. Karimi, S. Slussarenko, L. Marrucci, C. de Lisio, and E. Santamato, "Polarization pattern of vector vortex beams generated by q-plates with different topological charges," *Appl. Opt.*, vol. 51, no. 10, pp. C1–C6, Apr. 2012.
- [10] B. Piccirillo, V. D'Ambrosio, S. Slussarenko, L. Marrucci, and E. Santamato, "Photon spin-to-orbital angular momentum conversion via an electrically tunable q-plate," *Appl. Phys. Lett.*, vol. 97, no. 24, p. 241104, Dec. 2010.
- [11] E. Karimi, B. Piccirillo, L. Marrucci, and E. Santamato, "Light propagation in a birefringent plate with topological charge," *Opt. Lett.*, vol. 34, no. 8, pp. 1225–1227, Apr. 2009.
- [12] J. JJ Nivas, S. He, A. Rubano, A. Vecchione, D. Paparo, L. Marrucci, R. Bruzzese, and S. Amoruso, "Direct Femtosecond Laser Surface Structuring with Optical Vortex Beams Generated by a q-plate," *Sci. Rep.*, vol. 5, p. 17929, Dec. 2015.

- [13] T. Roger, J. J. F. Heitz, E. M. Wright, and D. Faccio, “Non-collinear interaction of photons with orbital angular momentum,” *Sci. Rep.*, vol. 3, no. 5, p. 3491, 2013.
- [14] Q. Zhan, “Cylindrical vector beams: from mathematical concepts to applications,” *Adv. Opt. Photonics*, vol. 1, no. 1, pp. 1–57, Jan. 2009.
- [15] J. JJ Nivas, S. He, Z. Song, A. Rubano, A. Vecchione, D. Paparo, L. Marrucci, R. Bruzzese, and S. Amoruso, “Femtosecond laser surface structuring of silicon with Gaussian and optical vortex beams,” *Appl. Surf. Sci.*, Oct. 2016.
- [16] S. He, J. JJ Nivas, A. Vecchione, M. Hu, and S. Amoruso, “On the generation of grooves on crystalline silicon irradiated by femtosecond laser pulses,” *Opt. Express*, vol. 24, no. 4, pp. 3238–3247, Feb. 2016.
- [17] G. D. Tsibidis, C. Fotakis, and E. Stratakis, “From ripples to spikes: A hydrodynamical mechanism to interpret femtosecond laser-induced self-assembled structures,” *Phys. Rev. B - Condens. Matter Mater. Phys.*, vol. 92, no. 4, p. 41405, 2015.
- [18] K. K. Anoop, A. Rubano, R. Fittipaldi, X. Wang, D. Paparo, A. Vecchione, L. Marrucci, R. Bruzzese, and S. Amoruso, “Femtosecond laser surface structuring of silicon using optical vortex beams generated by a q-plate,” *Appl. Phys. Lett.*, vol. 104, no. 24, p. 241604, Jun. 2014.

Chapter 6

Summary and perspectives

The main topic discussed in this thesis is based on surface structuring of silicon by fs laser pulses with Gaussian and OV beams. In the case of a solid material, the role of surface morphology is paramount in determining the surface properties of a material. Since diverse surface features can be generated by direct fs laser ablation, this can provide a single step processing method with great spatial resolution capable for modifying properties like optical, mechanical, chemical, biological, wetting, etc. Silicon is selected because of its exceptional properties and of the capability to show a multiplicity of surface structures. It was demonstrated that irradiation of crystalline silicon (100) with fs pulses produces a variety of structures generally termed as LIPSS. Among these, subwavelength ripples with spatial period Λ always near the laser wavelength λ are generally analyzed in the LIPSS studies. In contrast to the previous studies, here secondary quasi-periodic patterns, termed as grooves, which appear during high excitation, are also investigated. The grooves are characterized by above-wavelength period (more than $2 \times \lambda$), and are preferentially aligned along the laser polarization direction.

Regarding LIPSS generation, we addressed many issues seldom considered earlier, like bending and bifurcation of surface ripples, mechanism of micro-grooves formation, incubation factor related to ripples and grooves, etc. The inhomogeneous absorption over the laser irradiated surface by which ripples are generated is explained on the basis of Sipe-Drude theory which explains the interference of the incident beam with a "surface-scattered wave" originating from the pre-existing surface defects, as a responsible mechanism for the energy modulation. Our experimental results illustrate the diverse morphological features of surface structures, which are explained by considering the different excitation level obtained by means of a theoretical approach based on the combination of two-temperature model, free-carrier dynamics and Sipe model. This is done by calculating the spatial distributions of the deposited laser energy on the target surface which provide direct evidence of the diverse morphological characteristics of the produced structures, eventually explaining ripples bending and bifurcation phenomena, as well as grooves formation. The good agreement between 2D-

IFT maps of efficiency factor predicted by Sipe-Drude model and experimental results provides a direct evidence on the fact that the energy modulation is responsible for annular ripples formation as well as bending/bifurcation features of ripples observed at different excitation conditions. Moreover, experimental findings evidence a power law dependence of the threshold fluence on the number of pulses both for ripples and grooves formation, typical of an incubation behavior.

In the case of ablation at atmospheric pressure, the generated structures are always found to be decorated with large amount of NPs which come from the significant backward deposition of the abundant nanoparticles fraction of ablated material produced during ultrashort laser ablation. In order to understand the influence of re-deposited nanoparticles on the formation of surface features, structuring is done at varying pressure from high vacuum to ambient pressure. Interestingly, a comparative study done at high vacuum ($\sim 10^{-5}$ mbar) and atmospheric pressure with similar excitation conditions demonstrates a clear hindering of groove formation at reduced ambient pressure. This suggests that re-deposition of the ablated nanoparticles over the ripples can be one of important driving mechanism for grooves formation. Besides the groove formation, investigation on ripple by continuously varying the ambient pressure reveals a significant drop in the individual size and spatial period after 10 mbar while increasing the pressure from 10^{-4} mbar to higher values.

Apart from a Gaussian beam, ablation of crystalline silicon with spatially modified beams like, cylindrical OV beam with $m=+1$ having various SoP (radial, azimuthal, spiral and linear) enables the generation of diverse surface patterns over the silicon surface. Moreover, structuring with OV beam demonstrates how properties of complex beams can be obtained by analyzing the ablation crater. In this case, ripples are mostly situated over two annular ring-shaped regions near to inner and outer boundaries. In between these rings, an intermediate region with grooves is found surrounded by a narrow boundary consisting of rudiments of grooves. Due to the polarization dependency of the ripples and grooves, the morphology of the periodic structures formed in the annular crater allows direct visualization of the state of polarization complex OV beam, while analysis of the crater size provides beam spot parameters. We also determined the diverse threshold fluences for the formation of various complex microstructures generated within the annular laser spot on the silicon sample. Some examples of surface structuring at higher OAM (e.g. $m=+2$ and $m=+5$) are also done to demonstrate the large variation in the surface structures that can be created.

The thesis also addresses surface structuring of silicon with optical vector beams with much more complex polarization and asymmetric spatial intensity profiles. Here an experimental investigation was done on direct fs laser surface structuring based on the larger class of vector beams, generated by means of a q-plate. In addition to symmetric annular ablation crater by an OV beam, an asymmetric ablation crater in the shape of half-moon is generated with periodic surface structures inside, by electrically off-tuning the q-plate. The voltage tuning of the q-plate optical retardation allows producing a family of ultrashort laser beams with a continuous spatial evolution of polarization and fluence distribution in the focal plane, given by a controlled superposition of a uniformly polarized Gaussian beam and a standard, radially or azimuthally polarized, vortex beam. This, in turn, leads to a further extension of the diversity of achievable surface patterns. Moreover, the comparison of theoretical predictions of the vector beam characteristics at the focal plane and the generated surface patterns is used to rationalize the dependence of the surface structures on the local state of the laser beam offering an effective way to either design unconventional surface structures or diagnose complex ultrashort laser beams.

In perspective, the numerous kind of surface structures obtained by different optimization methods such as tuning the energy, number of pulses, ambient pressure, SoP, fluence profile, etc. obtained with Gaussian and vortex beams can be applied to large area surface structuring which might enable discovering further modifications in surface properties of materials. Moreover, the OAM and the tunability of optical retardation achieved by using q-plate can add more degrees of freedom in fs laser surface processing and allow designing more complex surface patterns. Since the asymmetrical surface patterns obtained on silicon closely resemble plasmonic structures used in some metamaterials, laser structuring might be extended in that direction selecting suitable material for the surface processing. Some initial trials have been done to optimize such asymmetrical pattern formation in silicon plate. However our investigation was mainly devoted to fs vector beams generated with a q-plate with a topological charge $q=+1/2$ in two specific configurations (i.e. radial and azimuthal OV beams at optimal q-plate tuning). Other experimental arrangements of the q-plate beam converter, as for example higher values of q or OV beams with even more complex SoP and variation of intensity pattern by optical retardation tuning, can be designed and used to fabricate still more complex surface patterns. Since the formation of surface structures seems to be ubiquitous to laser irradiation of solid targets with ultrashort pulses, the methods we have described can be directly extended to other materials of interest. Finally, the

possibility of fast switching intrinsic to a voltage tuning of the state of the q-plate can be joined to switchable wave-plates, as e.g. electronic controlled liquid crystal retarders, allowing the implementation of a setup based on high-speed generation and tuning of fs vector beams for an efficient fabrication of complex arrays of surface structures based on direct fs laser processing of solid targets.

Appendix I

Surface scattered wave model for the generation of periodic surface structures

According to the surface scattered wave theory by Sipe *et al.*, the modulation of energy over the laser irradiated surface is attributed to the interference of the incident beam with a "surface-scattered wave" originating from the pre-existing surface defects [1]. This results in an inhomogeneous energy deposition over the irradiated surface and eventually leads to ripples formation by modification of surface over periodic locations. With the aid of model predictions an empirical factor called efficacy factor η is calculated at different level of material excitation, which suggests a possible mechanism of subwavelength ripples and micro-grooves formation. Fig. 3.6 shows the geometry of the rough surface irradiated with s-polarized light at wavelength λ and the surface wave vector κ . In surface scattered wave theory, inhomogeneous energy absorption at the target surface, resulting from the interference of the incident laser beam with the surface scattered electromagnetic wave field caused by the surface roughness, is described by a function $A(k)$ that depends on the k and described as [2]:

$$A(k) \propto \eta(k)|b(k)| \quad (3)$$

where η is a response function describing the efficacy with which the surface roughness at k leads to inhomogeneous absorption of radiation and $b(k)$ is a measure of the surface roughness at k . $b(k)$ is a slowly varying function for a surface with a homogeneously distributed roughness and is obtained as Fourier spectrum of the spatial surface roughness. In particular, not all roughness contribute to η , instead there are some specific values of k that depend strongly on the incidence angle and beam polarization. The mentioned sharp peak occurs where the condition $|k_i \pm k| = k_0$ is satisfied, where k_0 is the wave vector corresponding to the incoming laser radiation with a central wavelength λ ($k_0 = 2\pi/\lambda$). This corresponds to the generation of non-radiative field structures which in the theory are called as "radiation remnants",

$$\eta(k; k_i) = 2\pi|v(k_+) + v^*(k_-)| \quad (4)$$

For the two cases of s- or p-polarized light, incident under an angle of θ and having polarization vectors and a wave vector component k_i as a complex function \mathbf{v} is given as,

$$v(k_{\pm}, s - \text{pol.}) = \left[h_{ss}(k_{\pm})(\hat{k}_{\pm} \cdot \hat{y})^2 + h_{kk}(k_{\pm})(\hat{k}_{\pm} \cdot \hat{x})^2 \right] \gamma |t_s(k_i)|^2 \quad (5)$$

$$\begin{aligned}
v(\mathbf{k}_\pm, \text{p-pol.}) &= \left[h_{ss}(\hat{\mathbf{k}}_\pm)(\hat{\mathbf{k}}_\pm \cdot \hat{\mathbf{x}})^2 + h_{kk}(\mathbf{k}_\pm)(\hat{\mathbf{k}}_\pm \cdot \hat{\mathbf{y}})^2 \right] \gamma_t |t_x(\mathbf{k}_i)|^2 \\
&+ h_{kz}(\mathbf{k}_\pm)(\hat{\mathbf{k}}_\pm \cdot \hat{\mathbf{y}}) \gamma_z \varepsilon t_x^*(\mathbf{k}_i) t_z(\mathbf{k}_i) + h_{zk}(\mathbf{k}_\pm)(\hat{\mathbf{k}}_\pm \cdot \hat{\mathbf{y}}) \gamma_t t_x(\mathbf{k}_i) t_z^*(\mathbf{k}_i) \\
&+ h_{zz}(\mathbf{k}_\pm) \gamma_z \varepsilon |t_z(\mathbf{k}_i)|^2
\end{aligned} \tag{6}$$

with linear products $(\hat{\mathbf{k}}_\pm \cdot \hat{\mathbf{y}})$ and $(\hat{\mathbf{k}}_\pm \cdot \hat{\mathbf{x}})$. An extended modeling details can be found in Refs. [2], [3]. Here $\kappa_\pm = \sqrt{\kappa_x^2 + (\sin\theta \pm \kappa_y)^2}$ and the dimensionless wave vectors $\kappa = \mathbf{k} \times \lambda / (2\pi) \equiv \lambda / \Lambda$.

Two numeric parameters, the shape factor (s) and the filling factor (f), are used to define the surface roughness and are related to γ_t and γ_z as follows:

$$\gamma_t = \frac{\varepsilon - 1}{4\pi \left\{ 1 + \left(\frac{1}{2}\right) (1 - f)(\varepsilon - 1)[F(s) - R \times G(s)] \right\}} \tag{7}$$

$$\gamma_z = \frac{\varepsilon - 1}{4\pi \{ \varepsilon - (1 - f)(\varepsilon - 1)[F(s) + R \times G(s)] \}} \tag{8}$$

where $R = (\varepsilon - 1)/(\varepsilon + 1)$, scalar function $F(s) = \sqrt{s^2 + 1} - s$ and

$$G(s) = \left(\frac{1}{2}\right) \left(\sqrt{s^2 + 4} + s \right) - \sqrt{s^2 + 1} \tag{9}$$

The values of the permittivity at ≈ 35 fs laser pulse duration, plotted in black in Fig. 3.7, provide the input parameters for the Sipe model described earlier, which allows calculating the inhomogeneous energy absorption pattern in the κ -space, for different experimental conditions. Then, discrete two-dimensional inverse Fourier transformation (2D-IFT) is applied to convert the efficacy factor distribution $\eta(\kappa)$ from wave vector κ -domain to real spatial domain, thus allowing an easier comparison of model predictions with the surface structures morphologies observed experimentally [2]. In particular, the inhomogeneous energy absorption pattern at the silicon

surface can be simulated by combining two-temperature model, free-carrier dynamics and Sipe theory [1], for different values of the laser pulse fluence.

Interaction of intense fs laser pulse triggers a variety of timescale dependent phenomena in the material depending on energy, pulse duration etc. As a result, material is already forced to an excited condition where the basic properties changes considerably and are very crucial in defining the resulting energy modulation. Therefore, Sipe-Drude model [2], [4], [5] calculate distribution of energy over the material surface by taking into account carrier dependent variation of surface dielectric permittivity induced irradiating the material with fs laser pulses [6], [7]. In fact, silicon irradiated by ultrafast laser pulses tends to exhibit metallic behavior with high temperature and high free-carrier number density, which can reach values as high as 10^{22} cm^{-3} [8]. The dielectric permittivity is evaluated by adding the effects of the free electron gas induced by the laser pulse to the unexcited bulk response [9]–[11] and can be described as [10]:

$$\epsilon = 1 + (\epsilon_{\text{si}} - 1) \left(1 - \frac{N_e}{N_0} \right) - \frac{\omega_p^2}{\omega^2 \left(1 + \frac{i\nu}{\omega} \right)} \quad (10)$$

where the $\omega_p = \sqrt{N_e e^2 / (m_e^* \epsilon_0)}$ corresponds to the plasma frequency with m_e^* being the effective electron optical mass. In equation (10) ν denotes the free carrier collision frequency and ω is the angular frequency of the incident laser pulse.

The temporal variation of the free-carrier density, N_e , induced by the laser pulse is described by the two-temperature model for the free-carriers temperature T_e and the lattice temperature T_l coupled to free-carrier dynamics equation [9], [10], [12]:

$$\left[C_l \pm \frac{\partial T_e}{\partial t} \Delta H_m \delta(T_l - T_m) \right] \frac{\partial T_l}{\partial t} = \nabla \cdot (\kappa_l \nabla T_l) + \gamma(T_e - T_l) \quad (11)$$

$$C_e \frac{\partial T_e}{\partial t} = \nabla \cdot (\kappa_e \nabla T_e) - \gamma(T_e - T_l) + Q_e \quad (12)$$

$$\frac{\partial N_e}{\partial t} = \nabla \cdot (k_B T_e \mu_e \nabla N_e) + G_e - R_e \quad (13)$$

where C_e and C_l are the heat capacity of electron-hole pairs and lattice, ΔH_m indicates the latent heat of fusion, $\delta(T_l - T_m)$ describes a smooth transition between solid and liquid phases at the silicon melting temperature, κ_l and κ_e are the lattice and free-carrier heat conductivities, γ is the energy coupling rate between free-carriers and lattice – here $\gamma = C_e/\tau_e$ with $\tau_e = \tau_e^0[1 + (N_e/N_{th})^2]$ where τ_e^0 and N_{th} are the initial energy relaxation time and critical density respectively. N_e is the free-carrier number density, evaluated by taking into account one- and two-photon absorption, avalanche processes, carrier diffusion and Auger recombination. In Eq. (13) $\mu_e = e/(m_e^*v)$ is the carrier mobility, k_B is the Boltzmann constant, $G_e = [(\sigma_1 I/\hbar\omega) + (\sigma_2 I^2/2\hbar\omega) + \delta_I N_e](1 - N_e/N_0)$ the gain of free-carriers produced by one-photon (σ_1) and two-photon (σ_2) absorption processes, and electron impact ionization δ_I and finally, $R_e = N_e/[\tau_{AR} + (C_{AR} N_e^2)^{-1}]$ describes the loss of free-carriers due to Auger recombination, in which τ_{AR} and C_{AR} are minimum Auger recombination time and Auger recombination rate, respectively. Finally the term Q_e in Eq. (12) is the input laser power density from the laser pulse and can be described as,

$$Q_e = \left[(\hbar\omega - E_g) \frac{\sigma_1 I}{\hbar\omega} + (2\hbar\omega - E_g) \frac{\sigma_2 I^2}{2\hbar\omega} - E_g \delta_I N_e \right] \left(1 - \frac{N_e}{N_0} \right) + \Theta N_e I + E_g R_e - \frac{3}{2} k_B T_e \frac{\partial N_e}{\partial t} \quad (14)$$

Here the first and second terms represent the net energy deposited in the target (per unit time and unit volume), and take into account photon and free-carrier absorption (Θ is free-carrier absorption cross section), and energy loss due to impact ionization (δ_I). The third and fourth terms describe the energy release caused by Auger recombination ($E_g R_e$), and the variation of the electronic heat capacity due to the time evolution of N_e , respectively. The temporal evolution of N_e calculated by solving Eqs. (11) to (13) allows deriving the time variation of the permittivity ϵ , through Eq. (1). The specific values of the coefficients used in the simulation are listed in Table 1. The initial target temperature is set at $T_0 = 300$ K (room temperature).

Table 1 | Parameters of silicon [2]

Coefficient	Symbol (Unit)	values
<i>Solid phase</i>		
Lattice heat capacity	$C_l (Jm^{-3}K^{-1})$	$10^6 \times (1.978 + 3.54 \times 10^{-4}T_l - 3.68T_l^{-2})$
Free carrier heat capacity	$C_e (Jm^{-3}K^{-1})$	$(3/2)k_B N_e$
Lattice heat conductivity	$\kappa_l (Wm^{-1}K^{-1})$	$1.585 \times 10^5 T_l^{-1.23}$
Free carrier conductivity	$\kappa_e (Wm^{-1}K^{-1})$	$-0.5552 + 7.1 \times 10^{-3}T_e$
Band gap energy	$E_g (eV)$	$1.167 - 0.0258(T_l/T_0) - 0.0198(T_l/T_0)^2$
One-photon absorption coefficient	$\sigma_1 (\mu m^{-1})$	$0.112 \exp(T_l/430)$
Two-photon absorption coefficient	$\sigma_2 (\mu mW^{-1})$	10^{-4}
Impact ionization probability rate	$\delta_l (s^{-1})$	$3.6 \times 10^{10} \exp(-E_g/k_B T_e)$
Free carrier absorption cross section	$\Theta (\mu m^2)$	$2.9 \times 10^{-10}(T_l/T_0)$
<i>Molten phase</i>		
Lattice heat capacity	$C_l (Jm^{-3}K^{-1})$	2.633×10^6
Electron heat capacity	$C_e (Jm^{-3}K^{-1})$	$10^2 T_e$
Lattice heat conductivity	$\kappa_l (Wm^{-1}K^{-1})$	$50.2 + 29.3 \times 10^{-3}(T_l - T_m)$
Electron conductivity	$\kappa_e (Wm^{-1}K^{-1})$	67

References

- [1] J. E. Sipe, J. F. Young, J. S. Preston, and H. M. van Driel, "Laser-induced periodic surface structure. I. Theory," *Phys. Rev. B*, vol. 27, no. 2, pp. 1141–1154, Jan. 1983.
- [2] S. He, J. JJ Nivas, K. K. Anoop, A. Vecchione, M. Hu, R. Bruzzese, and S. Amoroso, "Surface structures induced by ultrashort laser pulses: Formation mechanisms of ripples and grooves," *Appl. Surf. Sci.*, vol. 353, pp. 1214–1222, 2015.
- [3] J. Bonse, M. Munz, and H. Sturm, "Structure formation on the surface of indium phosphide irradiated by femtosecond laser pulses," *J. Appl. Phys.*, vol. 97, no. 1, p. 13538, 2005.
- [4] D. Dufft, A. Rosenfeld, S. K. Das, R. Grunwald, and J. Bonse, "Femtosecond laser-induced periodic surface

- structures revisited: A comparative study on ZnO,” *J. Appl. Phys.*, vol. 105, no. 3, p. 34908, Feb. 2009.
- [5] J. Bonse, A. Rosenfeld, and J. Krüger, “On the role of surface plasmon polaritons in the formation of laser-induced periodic surface structures upon irradiation of silicon by femtosecond-laser pulses,” *J. Appl. Phys.*, vol. 106, no. 10, p. 104910, Nov. 2009.
- [6] Z. Huang, Min and Cheng, Ya and Zhao, Fuli and Xu, “The significant role of plasmonic effects in femtosecond laser-induced grating fabrication on the nanoscale,” *Ann. Phys.*, vol. 525, no. 1–2, pp. 74–86, 2013.
- [7] J. Song, J. Ye, X. Lin, Y. Dai, G. Ma, H. Li, Y. Jiang, and J. Qiu, “Discussion of the possible formation mechanism of near-wavelength ripples on silicon induced by femtosecond laser,” *Appl. Phys. A Mater. Sci. Process.*, vol. 118, no. 3, pp. 1119–1125, 2014.
- [8] T. J.-Y. Derrien, J. Krüger, T. E. Itina, S. Höhm, A. Rosenfeld, and J. Bonse, “Rippled area formed by surface plasmon polaritons upon femtosecond laser double-pulse irradiation of silicon,” *Opt. Express*, vol. 21, no. 24, pp. 29643–29655, 2013.
- [9] G. D. Tsibidis, M. Barberoglou, P. A. Loukakos, E. Stratakis, and C. Fotakis, “Dynamics of ripple formation on silicon surfaces by ultrashort laser pulses in subablation conditions,” *Phys. Rev. B*, vol. 86, no. 11, p. 115316, 2012.
- [10] T. J.-Y. Derrien, T. E. Itina, R. Torres, T. Sarnet, and M. Sentis, “Possible surface plasmon polariton excitation under femtosecond laser irradiation of silicon,” *J. Appl. Phys.*, vol. 114, no. 8, p. 83104, 2013.
- [11] N. M. Bulgakova, R. Stoian, A. Rosenfeld, I. V. Hertel, W. Marine, and E. E. B. Campbell, “A general continuum approach to describe fast electronic transport in pulsed laser irradiated materials: The problem of Coulomb explosion,” *Appl. Phys. A*, vol. 81, no. 2, pp. 345–356, Jul. 2005.
- [12] T. J.-Y. Derrien, J. Krüger, T. E. Itina, S. Höhm, A. Rosenfeld, and J. Bonse, “Rippled area formed by surface plasmon polaritons upon femtosecond laser double-pulse irradiation of silicon: the role of carrier generation and relaxation processes,” *Appl. Phys. A*, vol. 117, no. 1, pp. 77–81, Oct. 2014.

Appendix II

Abbreviations

CCD	Charge Coupled Device
ET-SE	Everhart-Thornley
F	Fluence
FESEM	Field Emission Scanning Electron Microscope
fs	Femtosecond
G	Gaussian
GLP	Glan Laser Polarizer
H	Horizontal
HAZ	Heat Affected Zone
IL	In-Lens
ICCD	Intensified Charge Coupled Device
LASIK	Laser-Assisted In Situ Keratomileusis
LC	Liquid Crystal
LIBS	Laser Induced Breakdown Spectroscopy
LIPSS	Laser Induced Periodic Surface Structures
N	Number of Pulses
ns	Nanosecond
OAM	Orbital Angular Momentum
OV	Optical Vortex
PMT	Photo Multiplayer Tube
ps	Picosecond
SAM	Spin Angular Momentum
SE	Secondary Electrons
SEM	Scanning Electron Microscope
SLM	Spatial Light Modulator
SPP	Surface Plasmon Polariton
STOC	Spin-to-Orbital Conversion
SoP	State of Polarization
V	Vertical